Journal of Power Sources 657 (2025) 238132

Contents lists available at ScienceDirect

Journal of Power Sources

journal homepage: www.elsevier.com/locate/jpowsour

Untangling the variables: Operational parameters and metrics in NMC cathode synthesis by Co-precipitation

Marco Colasanti [a,*], Cristina Gatti [b], Maryam Maryam [b], Chiara Ferrara [b,d], Micol Di Veroli [a], Massimiliano Giona [c], Pier Giorgio Schiavi [a], Pietro Altimari [a], Francesca Pagnanelli [a]

[a] Sapienza University of Rome, Department of Chemistry, Piazzale Aldo Moro 5, 00185 Rome, Italy
[b] Department of Materials Science, University Milano Bicocca, via Cozzi 55, 20125 Milano, Italy
[c] Sapienza University of Rome, Department of Chemical, Material and Environmental Engineering, Via Eudossiana 18, 00184 Rome, Italy
[d] GISEL-INSTM Via G. Giusti 9, 50121, Firenze, Italy

HIGHLIGHTS

- Article Highlights.
- Previous studies identify spherical and smooth precursors as optimal product.
- The best operative conditions required to have the desired product are identified.
- A list of suitable reactors for the process has been compiled.
- Oxalates and carbonates are regarded as alternative products.

ARTICLE INFO

Keywords:
NMC
Co-precipitation
Transition
Lithium-ion
Battery

ABSTRACT

The wide range of applications for NMC lithium-ion batteries has led to increasing interest in the production of their cathodic material, as it is the most challenging component. Co-precipitation synthesis is the most promising method; it can be scaled up to industrial levels without compromising the quality of the resulting product. Despite the substantial number of studies on this topic, there is still no complete understanding of the process. Current studies are often collections of experiments in which operative parameters are varied through trial-and-error procedures to determine optimal conditions. A unified method is still lacking due to conflicting interpretations of the data. The study presented here compiles numerous outcomes obtained over the years, aiming to identify the best operative conditions. The conclusions are drawn from evaluating the most reliable theories proposed thus far. The goal is to establish a standardized procedure for the synthesis of NMC cathodic material, providing theoretical justifications and observations that go beyond merely collecting experimental data.

1. Introduction

Lithium-ion batteries (LIBs) have revolutionized modern society being small, easily modulable, lightweight, and with high energy density and thus emerging as the most appealing energy storage systems (ESS). These properties have been fundamental for the development of portable devices, and more recently for the adoption of electric vehicles (EVs), both needing for high-energy-density batteries [1,2]. Since their commercialization, LIBs have been improved in terms of performance (energy density, lifetime, cyclability, safety) and this evolution is strictly related both to improvement in cell design and assembly but mainly on the materials optimization. While the anodic graphite-based materials have not undergone substantial changes throughout the decades, huge efforts and milestones have been reached onto the development of new cathodic materials, which, consequently, largely determine the battery properties and characteristics [3–8]. $LiMn_2O_4$ (LMO) [8–10], $LiFePO_4$ (LFP) [8,11,12] - all belonging to the intercalation compounds. Among these various classes of materials, the layered systems derived from the LCO structure are the most exploited and are ramping up in the market share due to the best compromise in terms of high capacity, operating

This article is part of a special issue entitled: In memory of Professor Bruno Scrosati published in Journal of Power Sources.

* Corresponding author.
E-mail address: marco.colasanti@uniroma1.it (M. Colasanti).

https://doi.org/10.1016/j.jpowsour.2025.238132
Received 25 June 2025; Received in revised form 30 July 2025; Accepted 11 August 2025
Available online 21 August 2025

voltage, stability allowing to reach the high energy densities requested particularly for EVs applications (Fig. 1) [13].

Indeed, both the widely used LMO and LFP cathodes fall significantly short in terms of energy density, a critical parameter for automotive applications. LMO operates at a high voltage (around 4.5 V vs. Li+/Li) and can reach 95 % of its theoretical capacity (148 mAh g^{-1}), however processes such as manganese dissolution and Jahn-Teller effect lead to a relevant decrease in capacity throughout cycling and affect the overall energy density [15]. LFP works at lower voltages, around 3.5 V vs. Li/Li^{+}, with an acceptable theoretical capacity (170 mAh g^{-1}), but it presents a low energy density, together with poor electronic conductivity and ionic diffusivity [15].

While LCO layered electrode seemed to be the best option for EVs considering its high theoretical capacity (274 mAh g^{-1}) and high operating voltage (4.35 V vs. Li/Li^{+}), it present several drawbacks related to Co massive exploitation (i.e. high cost, critical supply due to high content of critical raw materials) and its poor stability at high temperatures, emerged as a driving force for the development of Ni-rich lithium transition-metal oxides (NMC and NCA materials, referred to the formula $Li(Ni/Mn/Co)O_2$ and $Li(Ni/Co/Al)O_2$), introduced in late 1990s [2,16–18]. The layered oxides, as discuss in more details in the next paragraphs, present some unique features such as the possibility to tune the compositions while maintaining the structure, and as a consequence to regulate the electrochemical behaviors and possibilities. Indeed, through the years the NMC materials have evolved significantly, both in terms of composition and morphologies, that have been determined as the two main parameters controlling the final functional properties. With respect to the other cathodes, this effort in the research has landed in the commercialization of new compositions and morphology, as schematized in Fig. 2. The fine control of composition and morphology is thus needed as well as the deep understanding of the correlation among these two aspects with the final desired electrochemical features. Given the cruciality in addressing the aforementioned issues and the insistent need for NMC-based LIBs, obtaining consistent features in NMC cathodes, particularly for future industrial-scale applications, is essential. The properties of these cathodes are intrinsically tied to specific synthesis parameters, such as temperature, pH, chelating agents, agitation, and operational time. Yet, to date, no single, standardized method has been established in the literature and no systematic investigations have been reported. This work, therefore, seeks to critically review the large amount of results presented in literature, focusing on the most relevant synthesis route (the coprecipitation of TM precursor followed by lithiation). We present a discussion of the experimental parameters explored in literature, and provide a correlation with the final structural, composition, and morphological features that in turns are directly correlated with the electrochemical performance.

To establish a quantitative foundation for the ensuing discussion, Table S1 (supporting information) compiles the findings from prior studies for statistical analysis. By graphing the results obtained from the cross-referencing of different studies, it is possible to obtain a global overview on each topic and to derive conclusions that are not operator or apparatus dependent. The statistical analysis was performed using the JMP software. The outcomes that were discussed are the only ones that proved to have satisfying statistical significance on the basis of the F-test.

2. Layered cathode -state of the art

Although the classes of cathode layered materials used today are essentially the same since their introduction (see Fig. 2), the obtained performances in terms of capacity, capacity retention, and lifetime are had been greatly and progressively improved. This is the direct consequence of the optimization of these materials in terms of chemical composition, doping, structural stabilization, and morphology control. Indeed, the materials' engineering it the key to improve and stabilize the performance of the layered materials that suffer of several drawbacks among which metals solubility, chemical instability at high potentials, formation of inactive phases [24,25].

The degradation mechanisms of such compounds have been widely investigated over the years, leading to a deep understanding (even if the complete picture is still not complete) of the correlation among the composition-structure-morphology and the performance and fading of the performance. For these reasons, in the following sections the main compositions of layered materials are presented with the evolution over the years; in the following the main causes of the failure of layered cathode are reviewed with the aim of rationalizing the most relevant parameters that need to be controlled and thus, potentially, optimized during the synthesis of these cathode materials. The identification of the main failure mechanism, detrimental phenomena, and side reactions causing of the degradation of the cathodes have led to the development of strategies to minimize these detrimental phenomena, allowing for improving of the performances.

2.1. Why layered oxides and their composition

$LiCoO_2$ has been one of the first proposed cathode materials [6,7,26] LCO is still considered as the reference cathode material for LIBs due to the high operating voltage (4.0–4.6 V vs Li/Li^{+}) and high theoretical specific capacity (274 mAh g^{-1}). It is characterized by a layered structure (space group R-3m) based on CoO_2 and Li alternated layers (Fig. 3a). The theoretical capacities 274 mAhg^{-1}, nevertheless, is never reached, the experimentally obtainable capacity values reported are

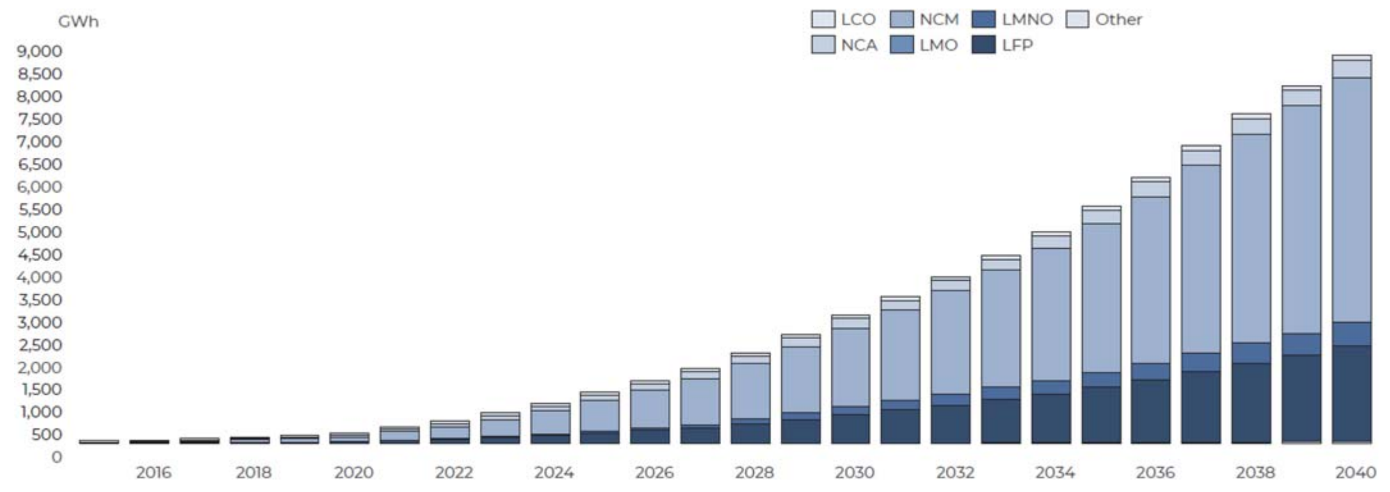

Fig. 1. Market share of cathode materials with expected trend up to 2040 [14].

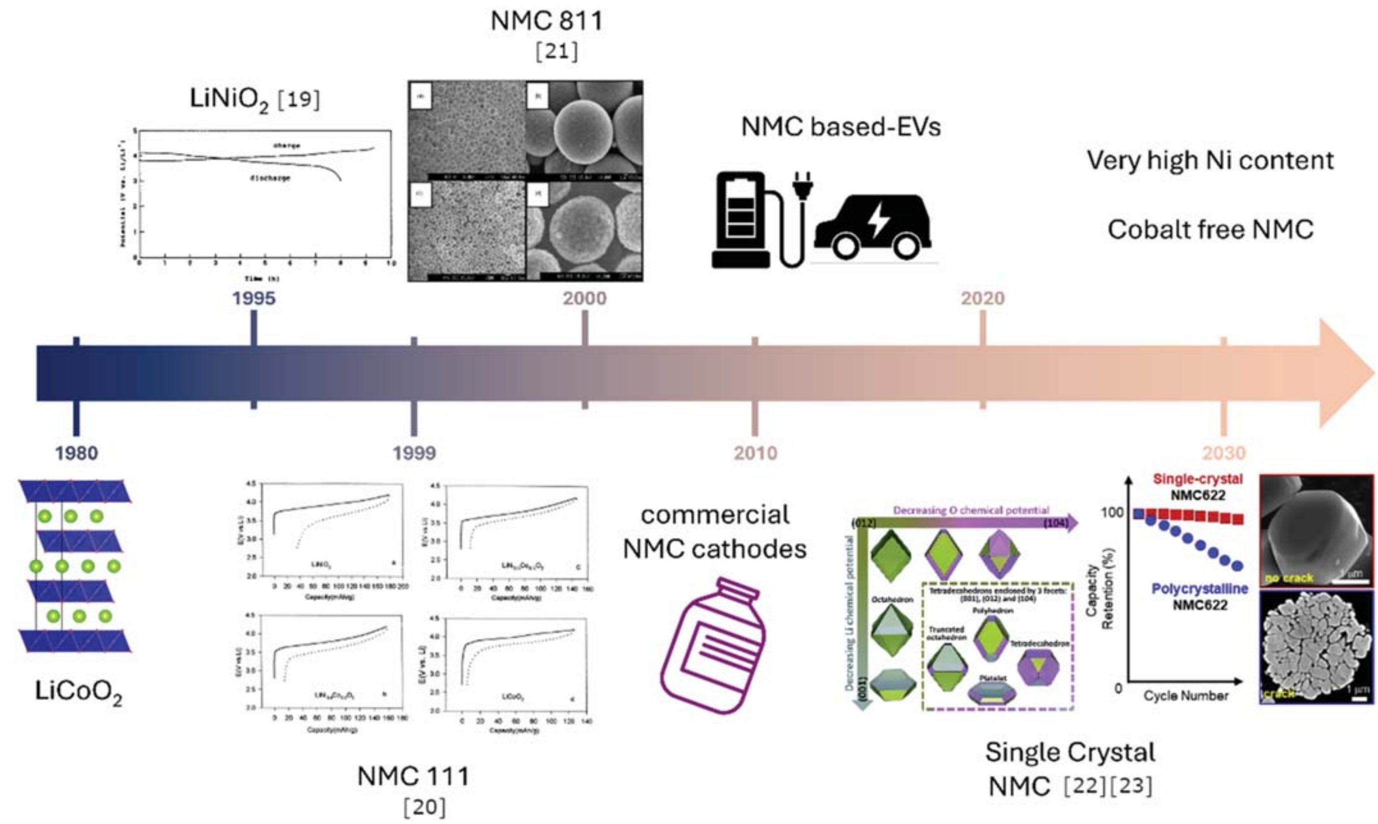

Fig. 2. NMC evolution and timeline [19–23].

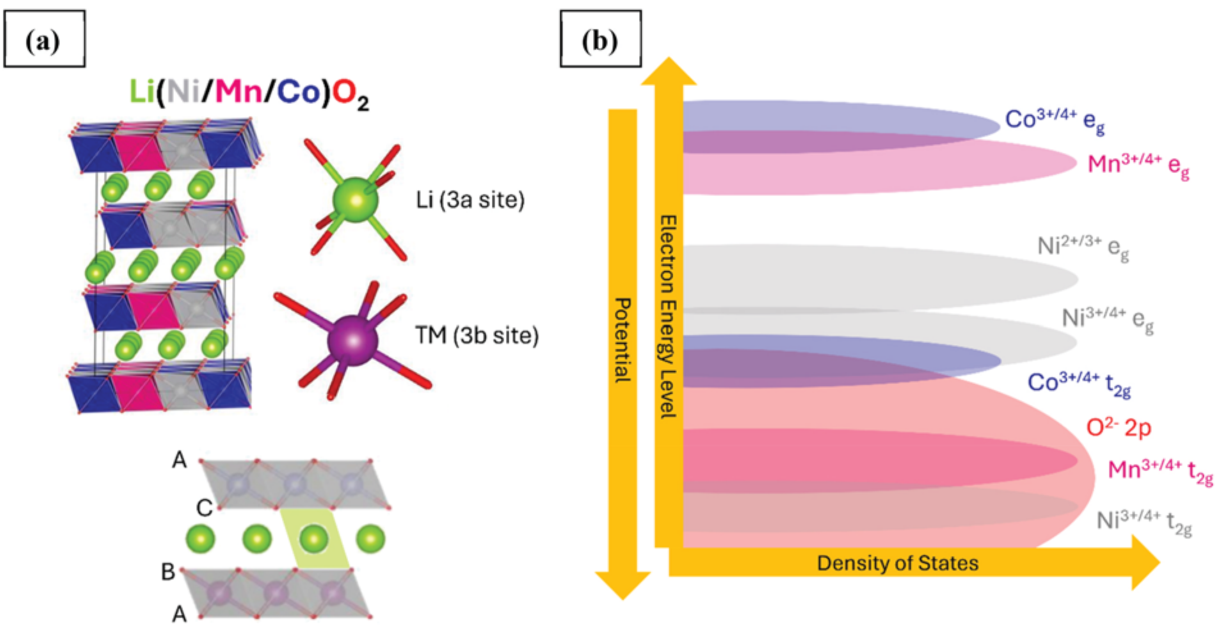

Fig. 3. Layered structure (a) and electronic structure (b) of the NMC cathode.

~140 $mAhg^{-1}$ at a potential of 4 V vs Li/Li^{+}. This limitation is directly correlated to the electronic structure of the material, and in particular to the superposition of the Co^{3+} t_{2g} and O^{2-} 2p bands [6,7,21].

Through the oxidation of the material the band of Co are gradually depleted; further charging at higher potential the material will causes the oxidation of $O^{2-}$with subsequent irreversible formation of O_2 and induced structural rearrangement of the material. At the same time, reaching high potential and enhancing the cathode voltage is one of the strategies to improve the overall cell voltage and, consequently, the powder of the battery. The main strategy adopted to overcome the chemical instability of LCO and increasing the operating potential has been the introduction of Ni^{3+} and Mn^{3+} in the structure. The substitution of Ni on Co site should provide extra capacity allowing to reach higher potential and avoiding the oxygen evolution thanks to the favorable positioning of the Ni bands (see Fig. 3b) while Mn is used to stabilize the structure, and it is not electrochemically active. The combination of higher operating potential and structural stabilization gives origin to higher experimental capacity, above 200 mAh g^{-1} [2,27].

A variety of compositions, generally referred as NMC materials, has been explored starting from the $LiNi_{1/3}Co_{1/3}Mn_{1/3}O_2$ (NMC111) the first one to be commercialized [28], followed by the introduction in mid-2000s of $LiNi_{0.8}Co_{0.1}Mn_{0.1}O_2$ (NMC811) enabling for the first time to reach high capacity (~200 mAh g^{-1}) combined with high potential (3.8 V vs Li/Li^+) [29] and followed by several compositions, trying to compensate and mitigate the advantages and disadvantages of the different metals composition, namely $LiNi_{0.6}Co_{0.2}Mn_{0.2}O_2$ (NMC622), $LiNi_{0.5}Co_{0.2}Mn_{0.3}O_2$ (NMC532), $LiNi_{0.4}Co_{0.2}Mn_{0.4}O_2$ (NMC424) [6]. Besides the NMC materials, also the Al doping has been proposed leading to the class of $Li(Ni/Co/Al)O_2$ compounds referred as NCA. The advantages of substitution of Mn with Al includes the lower atomic weight and cost of Al with respect to Mn [30,31].

The fine tuning of the composition allows to tailor the electronic structure and the structural evolution upon cycling and, additionally, address at the same time the problems related to the cost of Co. Each element and its percentage play a role in determining the final structural and functional properties of the cathode. Mn and Al are exploited for the structural and thermal stabilization but it must be considered that they are electrochemically inert (and present in the systems in form of Mn^{4+} and Al^{3+} respectively) [32,33]. The presence of Ni, as already mentioned, allows for higher voltage and higher capacity and thus improved energy density but at the same time it must be considered that the increase of the Ni and Mn contents induces an enhanced surface reactivity. Indeed, on the surface some defective species such as Mn^{3+} and Ni^{3+} can lead to unfavorable phenomena such as metal solubility with migration into the electrolyte, triggered by eventual presence of H^+.

The NMC cathode are thus more prone to surface reactivity with formation of cathode electrolyte interface, CEI, and/or migration of Ni and Mn into the electrolyte through the anode with respect to the LCO [2]. Although the high cost and sustainability problem, a fraction of Co is maintained in the system as its beneficial effect has been recognized and related to reduction of the magnetic frustration and the consequent lowering of Ni/Li cation mixing degree, the enhancement the electronic conductivity, and the improvement of the rate performance [34–37]. Nevertheless, it is still no possible to indicate the best performing composition as, as already mentioned, each element introduced in the system involves beneficial and detrimental effect at the same time. To better understand these aspects, it is necessary to face and discuss the degradation process affecting the NMC materials. The description of the failure mechanisms is here provided, with the attempt to highlight the interconnections among the different phenomena and the trigger of each of them. This will be considered as the starting point to identify the strategies to contrast the fading of the performance and, backwards, the best synthesis routes to control the desired composition and morphology.

2.2. Crystal structure and morphology

The $LiCoO_2$ and the NMC materials are isostructural to the α-$NaFeO_2$, crystallizing in the R-3m space group and presenting a layered hexagonal structure [38,39]. Li, transition metals (TM), and oxygen ions occupy respectively the 3a, 3b, 6c sites in this system (Fig. 3a); this arrangement leads to the formation of alternating TMO_2 and Li layers. The TM layers are formed of edge-sharing TMO_6 octahedra. With this respect, the Li ions occupy the octahedral positions (O) included between the TMO_2 sheets (see Fig. 3a); they can also occupy prismatic (P) and tetrahedral positions (T), leading to the formation of defects. Due to the stacking sequence of the oxygen (ABCABC), the structure is also defined as O3-type structure [38,39]. This arrangement is maintained for different compositions (pure Co, Ni/Mn/Co mixture, Ni/Co/Al mixture). The most common defect that has been reported it the Li^+/Ni^{2+} cation antisite disorder, due to the similar ionic radii (Li^+ 0.76 Å, Ni^{2+} 0.69 Å). The control of the actual stoichiometry and the severity of the antisite defect are among the main problems faced during the synthesis of these materials. Moreover, the Li/Ni antisite defect increase in relevance with the increase of the Ni content.

These materials can be obtained according to various synthesis routes, treated in more details in the next sections. Generally, what is obtained is a polycrystalline material presenting almost spherical micrometric particles, as many of the cathode active materials for lithium-ion batteries.

In the specific field of NMC materials the terms "polycrystalline" and "single crystal" have been used with a meaning not corresponding to the general understanding and, at the same time, not univocal definitions have ever been reported, example of these two peculiar morphologies are reported in Fig. 4. Single crystal is rigorously referred to a monocrystal, where the sample is entire, without any discontinuity in the periodic repletion of the structure (e.g. no grain boundaries), at a macroscopic level. This definition is never applying to the so called "single crystal" NMC for which indeed the single crystal morphology referred to large particles (generally above 2 μm) constituted by few particles (less than 5) with not random orientation [13,18]. In contrast "polycrystal" NMC are large particles (also up to 10 μm in industrial standard) but resulting at the aggregation of a large amount of subunits with lower degree of orientation or lack of orientation (in the order of hundreds of nanometers) [13,18,40,41]. Both the single and polycrystals are thus constituted by "particles" but the term "particles" is use quite generally referring to agglomerates and/or to the subunits. The definition of "primary" and "secondary" particles has been introduced. Secondary particles are large agglomerates formed by primary particles [16,40,42]. Primary particles are thus domains, generally in the order of 0.1–1 μm; the compact agglomeration of these form secondary particles. The number and reciprocal orientation of the primary particles thus define the secondary particles morphology as single or polycrystal, as schematize in Fig. 4, even if, formally, each secondary particle is rigorously speaking always a polycrystal. The terminology here reported is a tentative to rationalize the different notations appeared in literature even if rigorous and quantitative definitions of single and poly crystals are difficult to provide; the terms here introduced will be used in the following (see Fig. 5).

2.3. Failure mechanisms

The investigation on the causes of the degradation for the NMC cathode materials is a lively field, demonstrating how still today the complete picture regarding the complex interconnection of phenomena is still missing [24,25]. Indeed, several possible chemical, physical, and mechanical damages can occur.

The peculiar feature of these materials is the deep interconnections of the failure mechanisms leading to the fading of the performance. The complete treatment of the degradation mechanisms requires a detailed discussion that is actually out of the scope of the present work and several specialized reviews have been dedicated to this topic [24,27,43,44]. Here a brief overview is reported, highlighting the interconnections and mutual dependencies, from the atomic to the micrometric scale as the knowledge of the failure mechanism is considered as the starting point for the definition of improved composition and morphology able to provide enhanced performance.

- Irreversible oxygen evolution. Deep discharging involves high depletion of the Li layers associated to formation of high amount of Ni3+. The high level of delithiation involves the structural rearrangement, starting with migration of Ni3+ on Li sites (formation of Li/Ni antisite defects) with the local modification of the structure and release of highly reactive species such as O_2^-, O^- [45]. The release of oxygen is also accelerated at high temperature [46,47].

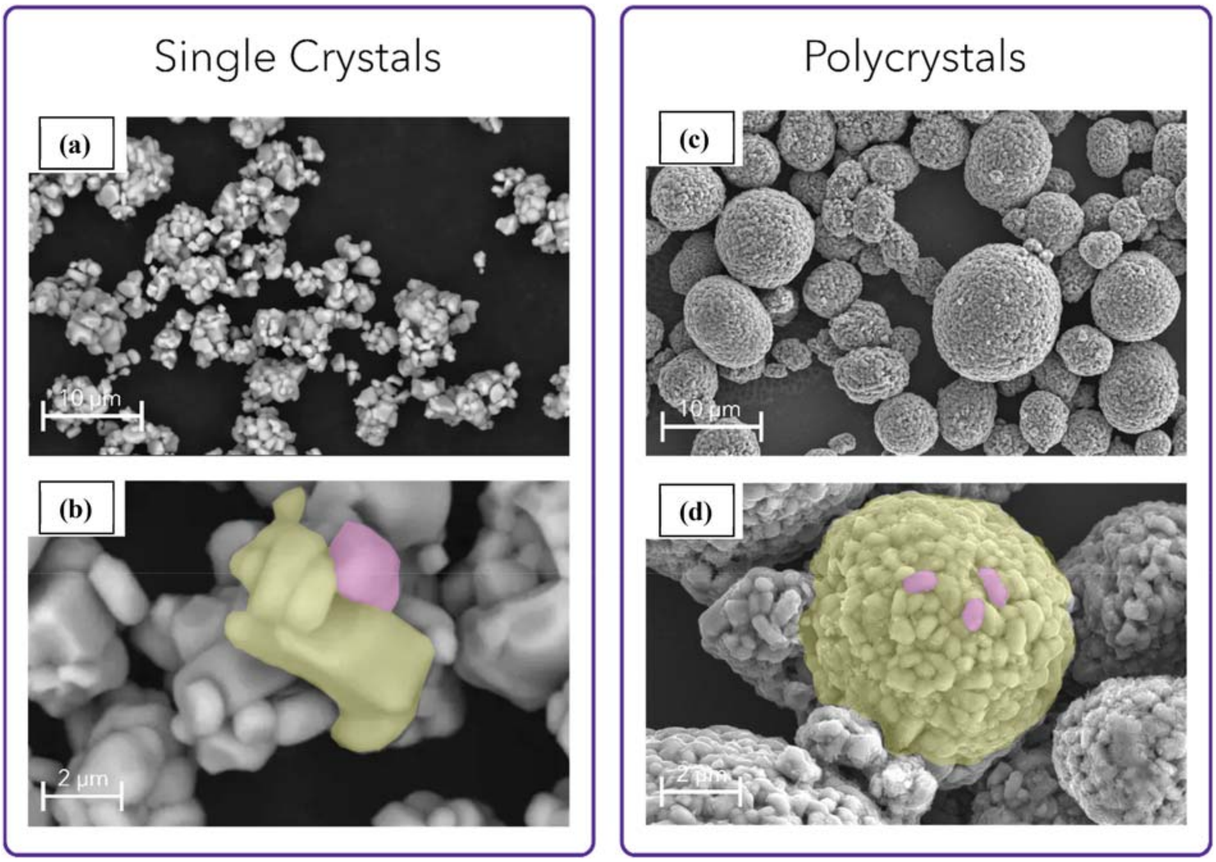

Fig. 4. Single and poly crystals morphologies with highlight of primary (red) and secondary (yellow) particles. (For interpretation of the references to color in this figure legend, the reader is referred to the Web version of this article.)

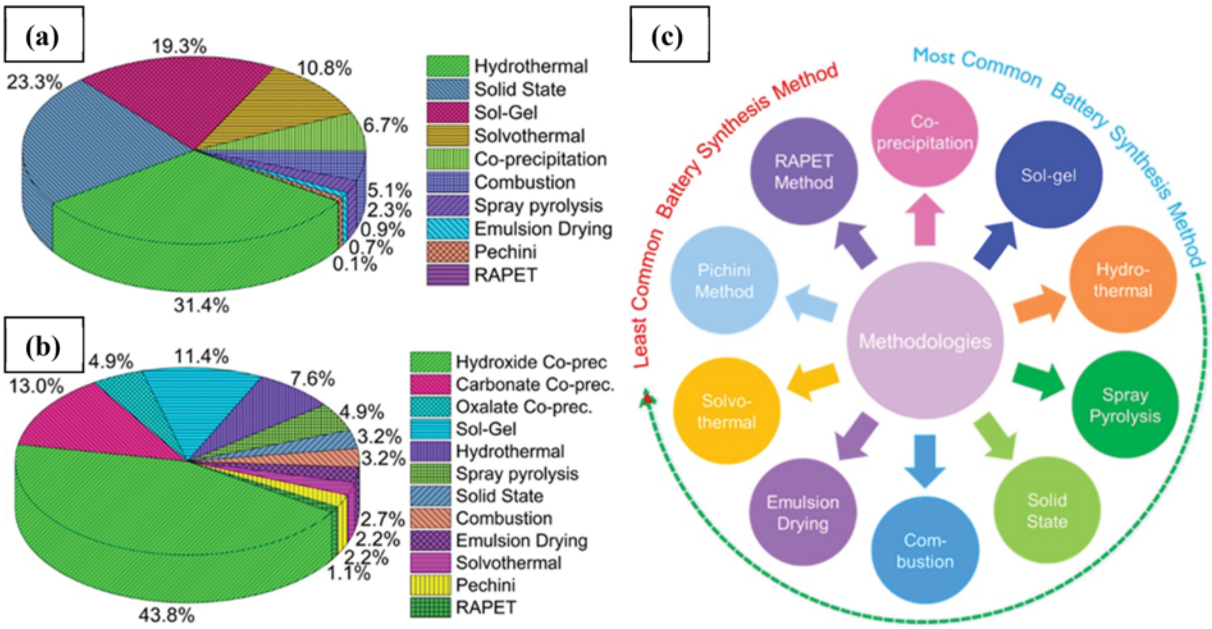

Fig. 5. Scheme on the synthesis methods exploited in scientific literature for the NMC production [16].

- Cation mixing and formation of antisite defects. A portion of Li^+ is observed on the TM site, while part of the Ni^{2+} can occupy the Li sites due to the similarities in the ionic radii ($r_{Li+} = 0.76$ Å, $r_{Ni2+} = 0.69$ Å). The Ni/Li antisite disorder is detrimental as it can limit both the Li ionic conductivity and the electric conductivity. The Ni/Li disorder can be triggered by the discharge process and it has also been related to the thermal history of the sample. With Li extraction from the structure, Ni migration into the Li layer is observed. This can also be followed by irreversible oxygen release from the structure, as described by the point above. Thus, lithium deficiency

induces local ordering of transition metals (TM), O, and O vacancies on the surface and favors the oxygen evolution at high potentials. Migration of Ni into the Li site can also cause variation in the interlayer distance and thus can be related to origin of microcracking defects (discussed in the next points), and it can also be the driving force for the phase transition to the rock-salt structure. [48,49]. As the Ni/Li mixing can be derived also from the synthesis route, it must be considered and controlled, particularly for high Ni content NMC.
- Transition metals dissolution. The well-known problem of the solubility of TM into the electrolyte with consequent migration and deposition on the anode is highly detrimental and responsible of irreversibility. It is particularly relevant for charging above 4.3 V; the driving force of this phenomenon are i) the corrosion of the material caused by the decomposition products of the electrolytes (i.e. HF, $HClO_4$), ii) the eventual high level of Li/Ni antisite defects, iii) high surface area of the particles [50–52]. The dissolution of TM metals involves local compositional changes that in turn can induce phase transitions with formation of electrochemically inert species (metals oxides, spinel).
- Structural instability. Generally, at voltage higher than 4.2–4.3 V the structure evolves toward thermodynamically stable phases (spinel structure and rock-salt structure). This phenomenon is triggered by the irreversible oxygen release, the compositional changes on the surface of the particles, Ni migration into the Li sites [53]. Moreover, at high potential, deep delithiation can be reached; this favors a strong anisotropic structural relaxation that in turns further promotes the cation mixing and the oxygen evolution.
- Mechanical cracking. The mechanical degradation of the secondary particles has been described, and it is followed by electrolyte penetration with high electrolyte consumption for the higher CEI formation. Mechanical pulverization is triggered by the anisotropic volume variation during lithiation and delithiation, particularly when reaching high delithiation states, involving mechanical stress at nanoscale and microscale [54–56].
- Surface reactivity and phase evolution. Phase transitions from layered structure to rock salt structure occurs mainly on the cathode surface. This phase evolution is favored by high temperature, high Ni content, deep delithiated states and generally leads to the formation rock salt phases. These phases are undesired as they present null Li transport properties and poor electric conductivity (insulating phases). Phase transformation can be promoted by the presence of Ni^{4+} at the surface and is generally associated to the formation of CEI. The surface reactivity can be stimulated by residual compounds from the synthesis. Indeed, excess Li is frequently introduced during the synthesis of such materials to compensate for Li volatilization during the high temperature treatment and to prevent Ni/Li mixing. At the same time this can lead to the presence of residual lithium compound (RLCs) on the cathode surface with the most frequently observed and stable being Li_2CO_3 and LiOH. The presence of such RLCs has been associated with irreversible capacity losses and their presence is not favorable as they are ionic and electronic insulators [57,58].
- Formation of cathode-electrolyte interphase (CEI). The CEI formation is specific of layered materials while is not so relevant for other cathode materials. In the case of NMC material the CEI formation is triggered by the highly reactive Ni^{4+} on the surface of the particles, leading to local degradation of the electrolyte for formation of CEI, involving NiO formation [50,59–61].

2.4. Contrasting the failure: strategies

The majority of the above reported effect are evidently interconnected and the trigger of one of this mechanism can activate also others, with a domino effect (e.g. the TM migration is associated to oxygen evolution that is followed by structure collapsing; the deep discharging involves the structural relaxation leading to mechanical cracking). To prevent the detrimental cascade effect is at the same time essential and not trivial. Several strategies have been considered to mitigate or limit these failure mechanisms. A brief overview of these strategies is reported in Table 1 and Table 2 with references to high quality dedicated works.

2.4.1. Why single crystal

Among the abovementioned strategies for the limitation and control of the failure mechanisms, the morphological control with the production of the so called "single crystal morphology" is the one more explored and that led to the commercialization.

The definition of single crystal (SC) non rigorous as it is referred generally to particles consisting of few (less than 5) primary particles with global dimension of ~2–6 μm in contrast to polycrystalline (PC) cathodes composed of large micrometric secondary particles made up of primary nanometric particles. A more operative definition classifies as SC the cathodes composed of primary particles with no cracks while, in contrast PC are constituted by secondary particles where cracks can be present and well visible. The adoption of the SC term is not specific, and it is referred to a variety of morphologies of the final particles. Even maintaining this definition, the need for quantitative parameters identifying the single crystal morphology is still needed, and difficult to formulate based on the current state of the art [23,44,73,80].

Advantages/benefit of single crystals:

- limited surface area and grain boundaries with respect to PC, limited surface reaction and CEI formation with lower electrolyte and Li consumption.
- limited exposed surface contains the M migration from the cathode into the electrolyte.
- no primary cracking, no electrolyte penetration, further limiting the exposed cathode particles 'surface.
- high Li ionic conductivity, Li diffusion within the particles is not hindered by grain boundaries.

SCs thus present several advantages with respect to the other strategies reported in Table 1. For example, doping with stabilizing elements such as Zr^{4+}, Y^{3+}, Al^{3+} introduces electrochemically inactive sites,

Table 1
Overview of the possible strategies adopted to contrast the failure mechanisms.

Bulk and lattice engineering		
Doping, compositional engineering	**Core-shell structure**	**Gradient concentration**
Control of composition with cation substitution to improve the structure stability, modify the cell parameters, typically with electrochemically inactive species [25, 62–65].	Creation core shell structure to create a buffer shell able to minimize the reactivity with electrolyte and buffer the mechanical stress [66,67].	Similar to the core-shell concept, creating a concentration gradient in particles' section to prevent and minimize the reactivity with the electrolyte [68,69].
Surface engineering		
Surface phase modification	**Surface coating**	**CEI optimization**
Modification of the superficial phases to create a stabilized interface [54].	Introduction of the electrochemically inactive coating protecting the bulk materials from reactivity with electrolyte [69].	Controlled formation of CEI layer with introduction of reactive additive into the electrolyte [70,71].
Morphology control		
Single crystal	**Rod shape particles**	**Facet regulation**
Formation of particles with specific shape and dimension, enabling for the minimization of failure mechanisms [72–75].	Formation of particles with controlled shape (rod like), enable to minimize the effect of anisotropic cell breathing during charge/discharge processes [76,77].	Formation of particles with controlled facets growth to minimize the reactivity with the electrolyte, control the ion diffusion, and formation of secondary phases [78,79].

Table 2
Advantages and disadvantages of various synthesis techniques for producing $LiNi_xMn_yCo_{1-x-y}O_2$ cathode materials.

Synthesis Method	Advantages	Disadvantages
Sol gel	- low synthesis temperature and short healing time - Small diameter particles with uniform size and crystallinity	- Complex operating process, requiring long preparation time - High energy consumption and environmental impact
Spray pyrolysis	- Short residence time in reactor with higher production rate - Excellent reproducibility without the need for post-synthesis purification	- Formation of hollow secondary particles - Low tap density
Hydrothermal/ solvothermal	- Low energy consumption - High crystallinity of transition metal oxide, better performance	- Considered like a treatment method, not a conventional method - Involves additional steps compared with other conventional methods
Combustion	- Simple method with minimal or no external energy requirement - Size of the crystal can be easily controlled and optimized	- Large particle size - Presence of impurities in case of incomplete combustion
Solid state	- Simple one step process, not requiring sophisticated equipment	- Requires significantly mechanical mixing
Coprecipitation	- More environmentally friendly	- Particles are more susceptible to fracture due to high porosity - Compositional difference between desired metal ratio and feed
Pechini method	- Provides good control of the stoichiometry at a relatively low cost - Required shorter sintering time	- Limited to the solution where the dissolved salt does not precipitate
Emulsion drying	- Produces homogeneous powder precursors - An excellent method to control particle size and morphology	- Lengthy and complicated process - Energy intensive and producing significant waste
RAPET method	- Simple one stage, cost effective, and efficient method - Surfactant and solvent free, gives a high yield and reproducibility	- Requires long hold time - Limited options to control particles size and morphology

lowering the overall theoretical capacity. Coating is generally based on non-active materials (2–5 %w of Al_2O_3, TiO_2, MgO) thus while protecting the cathode it introduces inert mass into the cathode, lowering the energy density. Moreover, the coating thickness must be carefully regulated to balance the protective and the insulating effects. The concentration gradient of the NMC composition within the particle's profile require very fine control during the synthesis. The facet control and rod shape particles are difficult to obtain and scalability is problematic. On the contrary, the procedure to obtain SC particles has been now widely studied and has been optimized to be compatible with the traditional synthesis procedures (two steps route described in the following paragraphs). Moreover, the SCs morphology can be combined with other strategies (e.g. doping, surface modification) thus offering higher flexibility. It is relevant to report here also some limitations of the SCs approach, the main ones related to the lower surface with respect to PC particles, limiting the interfacial reaction, the large particles imposing kinetic limitations in the Li^+ diffusion within the particles, macroscopic fractures and kinking [44,73,81,82].

Based on all these considerations, the SCs approach to emerge above the others, leading to a variety of reports on the synthesis and characterization of such SC-NMC materials [72,73,75,83]. Finally, among the other strategies reported, SC is the more mature, with some available commercial products.

Due to the huge effort in the production and optimization of SC NMC cathode, very recently the investigation of the fading of performance in SCs has led to identification of specific mechanisms affecting these materials. Among them the cracking of secondary particles with pulverization of the electrode, loose of electric contact, high CEI formation has been identified as the most serious and detrimental [13,84,85].

2.5. *Looking forward: the target layered cathode*

Based on the review of the existing literature and knowledge it is possible to identify some guidelines to target the most promising features of the NMCs and direct the synthesis of new optimized materials. High Ni contents are desirable to reach for high-capacity values but at the same time inevitably involves the lowering of the capacity retention as high Ni content is associated to some of the abovementioned fading mechanism (e.g. Ni solubility, structural instability). At the same time, pure Ni composition ($LiNiO_2$) is not experimentally exploitable for its high thermal and structural instability. Although the tendency is to move for "Co free" cathode materials, as a perspective it is not feasible to completely eliminate cobalt as it is crucial for the stabilization of the structure, enhancing both the thermal stability and conductivity. Inert species such as Mn and Al are beneficial to further stabilize the structure upon cycling. Thus, the mixed compositions NMC and NCA with high Ni content seems to remain the more promising for the near future perspective. At the same time, as discussed, Ni rich compositions are inevitably linked to specific detrimental effect such as favorable Ni/Li disorder, Ni dissolution, formation of secondary phases, oxygen degassing.

2.6. *Production methods*

Today the "Ni rich" compositions (Ni $>$ 0.6) represent the commercial benchmark cathode materials for high energy density applications (Ni $=$ 0.6) while Ni $>$ 0.8 represent the target to be reached. In this regard, the control over the nominal stoichiometry becomes increasingly important with the increase of the Ni content, thus is essential to control this parameter also for the precursor of the synthesis, generally mixed Ni/Co/Mn hydroxides as discussed in more details in the following sections. Indeed, apart from the considerations reported above on the correlations between the Ni content and the electrochemical performance, it must be considered also the needs and requirements for the manufacturing and handling of NMC and NCA materials. The Ni rich compositions are associated with higher sensitivity to exposure to air and humidity, with the consequent formation of surface oxides and hydroxides species, detrimental for the final applications [86–88].

Regarding the morphology and particle size, the PC vs SC strategies has been presented in the previous sections. SC materials have been developed to holistically contrast the failure mechanisms of the PC materials, reported above, minimizing the surface reactivity, degassing, mitigating the pulverization and TM migration. Nevertheless, this approach is not always affective and with increasing Ni content the failure of SC with respect to PC is even faster and more severe. In particular a threshold seems to be identifiable around Ni 0.7: below this value the implementation of SC morphology seem to be effective while for higher Ni content the SCs fail more abruptly than PCs analogue [40,89]. Recently the specific failure mechanisms for SC materials have been investigated and unveiled; in particular interplanar gliding, kinking and leading to intergranular cracks being the most severe [82,85,90–95]. Nevertheless, a systematic study of the PC vs SC behavior is still missing and hindering a complete comprehension of the cascade effect in the failure mechanisms (i.e. the trigger event, the correlation among composition/structure evolution and electrochemical parameters). The SC morphology is thus effective under the restriction of low Ni content (Ni

< 0.7); at higher Ni content further strategies need to be coupled with this peculiar morphology (e.g. particle size control [84,85], doping [96,97], coating [98,99], artificial CEI [100]).

It is thus possible to identify the NMC 811 as one of the most promising compositions, combining and balancing the beneficial and detrimental effect of high Ni content. For compositions around this range, the dimension of 2–3 μm range for the secondary particles can be propose as, again, a good compromise among the PC advantages (short diffusion paths for Li, fast kinetic) and SC advantages (low expose surface, minimization of cracking, minimization of the mechanical stress during cycling).

High-capacity values (>180 mAh g^{-1} at cut-off potential <4.3 V) can be achieved) together with capacity retentions above 90 % for 500 cycles at 2C for SC materials with Ni content in the 0.6–0.7 [23,101,102] range while PC materials can provide this performance for Ni content in the range 0.6–0.9 [103,104]. Nevertheless it must stressed that, for the same composition a huge variability in the capacity and capacity retention values can be found in literature and can be ascribed to other relevant parameters beside the morphology of the NMC particles, such as the C rate, the selection of the electrolyte, the potential cut off, the number of cycles, use of additives [105–107].

The process of synthesizing the NMC materials is crucial to obtaining the necessary properties and performance because, as highlighted in the previous sections, the combination of controlled composition and morphology lead to desired composition but also very specific failure mechanisms [108].

NMC are thus obtainable with various methods, a further advantage of this class of materials as specific features can be obtained through the selection of the synthetic path. The sol-gel method, solid-state reaction, hydrothermal synthesis, spray pyrolysis, combustion, coprecipitation, template method, and solvothermal for the synthesis of the cathode are some of the wet chemical, and solid-state synthesis techniques that have been developed in the last few decades [109–112].

A straightforward and affordable method emerged for creating cathode nanostructures with a high yield and particle sizes as small as 20 nm is solvothermal/hydrothermal synthesis, as also evident from Fig. 1 and Table 1 [16,113]. Better electron transport and a shorter Li^+ diffusion channel inside the synthesized nanostructures are the reasons for the cathode materials' improved performance. The particle size may be further decreased by using the hydrothermal synthesis technique with an addition of ethanol or ethylene glycol [114]. However, it has also been shown that finer and more desirable nanostructures may be synthesized using additive-free techniques [115]. The main disadvantage is that a number of process variables (type, volume ratio and concentration, precursor source and mixing sequence, process time, pressure, and drying temperature) make it challenging to control the final nanostructure's size and shape [115–117]. Moreover, no systematic investigation of such parameters has been reported and their effect has not been completely rationalized; we propose a critical discussion in the next paragraphs.

Other relevant synthesis path are represented by the solvothermal/hydrothermal approach, emerged as one of the most widely used techniques for creating nanostructured cathode materials, borrowed from the LFP-based materials [118–121]. Generally, solid state synthesis has been widely exploited for preparation of polycrystalline cathode materials can be easily produced with high throughput using the solid-state reactions approach. Short Li^+ diffusion channel lengths allow for the easy synthesis of hollow and porous cathode nanostructures for high rate and long-term cycling stability. However, this process does not provide adequate control over the final size and form of the material when it comes to nanostructure production. Additionally, since the initial reagent materials are solids and intimate mixing is impossible to achieve, it is challenging to produce nanostructured materials with well-controlled shape. Spray pyrolysis process has also been proposed but the difficult control in regulation of the reactants and byproducts is limiting its diffusion [122].

Among the others, as evident from Fig. 1 and Table 1, the synthesis based two-step process (coprecipitation of transition metals followed by high temperature treatment with the addition of a lithium source) is the most exploited. Coprecipitation is extensively used in several industries, including water treatment, pharmaceuticals, metal mining, and catalyst manufacturing thank to the high flexibility and scalability [123,124]. In the last 20 years, coprecipitation has drawn more attention, particularly for NMC cathode materials, because of its ease of use, improved control over particle shape, atomic-scale homogenous mixing, and simple scaling [125,126].

As cited, this synthesis consists of two main steps i.e. the coprecipitation of transition metals and sintering as shown in Fig. 2. In the first stage, transition metals are mixed in the proper ratio to create an ionic solution. These metals are then coprecipitated in a controlled environment by altering the pH to produce homogeneous particles known as precursors (in the large majority hydroxides, followed by oxalates and carbonates). To produce single-phase coprecipitates, a chelating agent is often exploited during the precipitation process. These precursors are washed with deionized water to remove impurities and dried to eliminate residual solvents. Before combining the coprecipitate with a lithium source, such as lithium carbonate (Li2CO3) or lithium hydroxide (LiOH), the precursors may be grinded. To create the active materials for battery electrodes, a homogenous mixture of coprecipitate and lithium source is sintered in one or two phases, depending on the metal sources and sintering circumstances [127].

A key advantage of using the coprecipitation process is to achieve the desired phase and crystallinity at very moderate sintering temperatures and holding times [128]. Despite the fact that sintering often modifies the size of primary particles and the surface roughness of secondary particles, the comparatively moderate sintering conditions help to preserve the size and shape of secondary precursor particles [128,129]. Numerous controllable parameters during coprecipitation processes, including pH, precipitation temperature and atmosphere, sources of transition metals and their concentration, use of chelating agents and their concentration, rate of reactant feed, stirring rate and mixing method, drying temperature, and the use of any additional additives, can have a significant impact on the morphology and composition of the coprecipitate [130].

Sintering conditions including (if palletized or not, the number of sintering steps, the sintering duration, and the sintering environment (air, oxygen, or inert) also have an impact on the electrochemical performance and particle structure of active material [130,131].

The two steps synthesis based on coprecipitation and high temperature sintering is the most common for NMC material, also at industrial level. Due to its relevance, it is discussed in more details in the following section. The experimental parameters explored during both steps are thus discussed as they do play a role in determining the final composition, morphology, and functional behavior.

3. Nucleation and growth

In this instance, the reaction under investigation is metal coprecipitation, wherein hydroxide anions function as precipitating agents. The emphasis on this particular procedure stems from its preeminence in contemporary practice, as it stands as the sole method employed in industrial settings.

In the context of a precipitation reaction, it is imperative to comprehend the mechanisms of nucleation and growth. A paucity of studies has hitherto been published that offer a comprehensive range of proposals for the analysis of these mechanisms.

Before delving deeper into the nucleation and growth mechanisms, it is necessary to clarify the reactions involved. Metal ions can undergo two reactions: precipitation due to interaction with hydroxide anions or the formation of the soluble complex $[M(NH_3)_n]^{2+}$ due to interaction with the chelator (NH_3). The precipitation process depends on the equilibrium between the formation of the ammonia complex and precipitation (a more detailed study is presented in the section on the effect of the chelating agent).

The first attempt to identify the nucleation and growth phenomena can be found in the study by Yang et al. [132]. They initially examined the crystalline structure, which has an octahedral unit cell. At the center of the cell is the metal ion, surrounded by OH^- anions arranged in a layered structure, with the external surfaces possessing negative charges. Due to these charges, metal-ammonia complexes are attracted to the surfaces. The crystals are organized such that the negative charges are mainly distributed along the (001) plane; therefore, growth along this direction is faster. As a result, the primary particles (the term used in this work for the basic particles obtained from nucleation) will have an acicular structure.

These basic primary particles subsequently undergo two growth phenomena: agglomeration and growth. Agglomeration occurs due to the interaction between multiple primary particles, while growth is driven by Ostwald ripening, where smaller primary particles, being below the critical size (coming from uncomplete nucleation or particles collision [133]), dissolve and release metal ions. These ions precipitate upon contact with already-formed crystals, causing them to grow.

This latter phenomena also induces a smoothing process; particles may develop sharp edges due to impacts and agglomeration. These edges do not minimize surface energy, so they dissolve and, through Ostwald ripening, recrystallize along the surfaces of pre-existing particles, leading to a smoothing process.

Over time, these growth phenomena result in the formation of the final particles, which, in accord with Sun et al. [133], reaches its final shape and dimensions when there is a balance between collision and re-dispersion phenomena. Yang et al. [132] supported this growth process by performing precipitations in batch reactors using different operative times, then they were analyzed with XRD and SEM imaging (see Fig. 6).

In 2017, Hua et al. [134] proposed a growth process consistent with that of Yang et al. [132]. As shown by Fig. 7 they identified a growth pattern that was not unidirectional but led to the formation of primary particles with hexagonal sheet shapes. Although their theoretical justification was somewhat weak (as it mirrored that of Yang et al. [132]), their proposal aligns more closely with the SEM images typically observed in studies in this field. This same observation was later highlighted by Zhu et al. [135], who also attempted to identify a nucleation and growth process.

Only in few studies [135–137] primary particles reach acicular shape. The primary distinctions between these conditions and the standard ones pertain to the agitation rate. These primary particles are usually recovered by working with Taylor-Couette reactors or using impellers different from the radial one. This evidence that nuclei growth is not only matter of chemistry but it also depends on the fluid-dynamics.

In addition, all the studies that have previously tried to identify growth phenomena [132,134,135,138–140] had not success in evidencing nucleation steps. The kinetic of nucleation is so fast that cannot be easily detected. It has been demonstrated that transport phenomena are the rate-determining step of the reaction, thereby

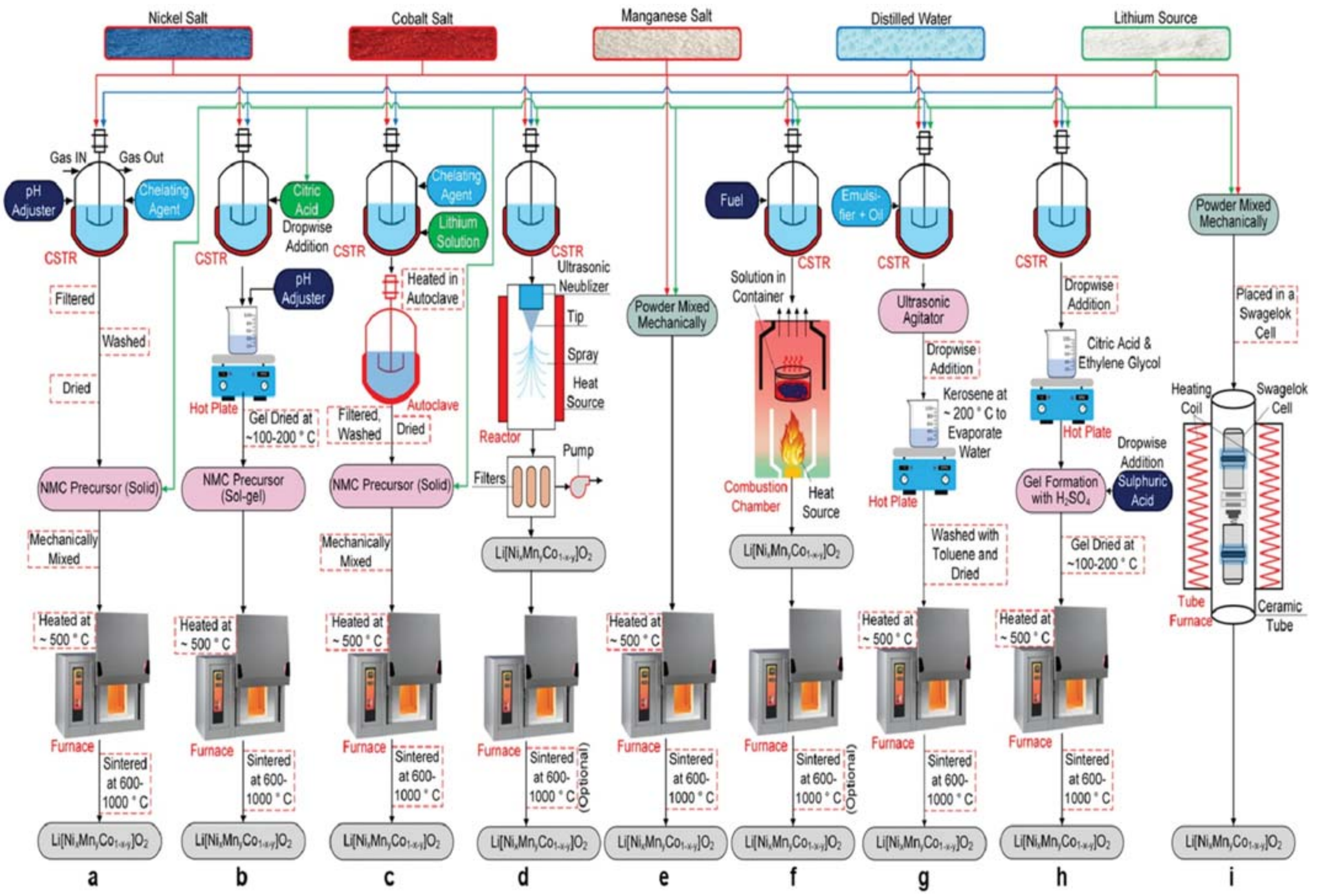

Fig. 6. Schematic representation of the LiNi$_x$Mn$_y$Co1-x-yO$_2$ cathode material manufacturing process using several techniques Coprecipitation (a), sol-gel (b), and hydrothermal (c) (solvothermal uses the same procedure, but a different solvent). (d) solid-state, (f) combustion, (g) emulsion drying, (d) spray pyrolysis (the process is the same as the spray drying technique, but the reactor's heating source is orientated in front of the spray rather than parallel to it), (i) RAPET; (h) Pechini. A continuous stirred tank reactor (CSTR) is not required and is just used for comparison. Both heating and sintering the mixture at the necessary temperature in the necessary environment may be done in a furnace. The first heating process, which typically takes place at 500 °C, is usually optional.

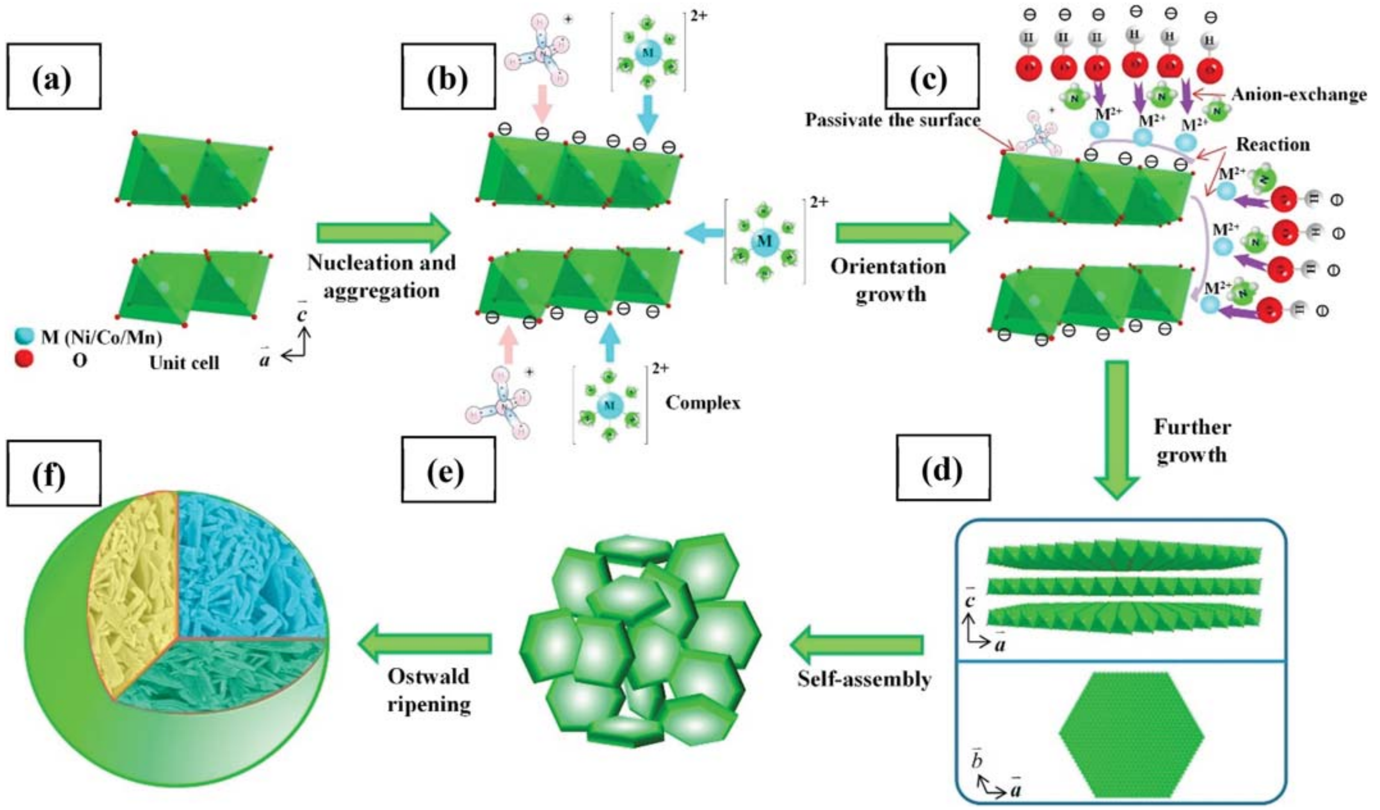

Fig. 7. Growth process proposed by Hua et al. [134]. The mixed metal nuclei (a) interact, causing growth along the preferential directions [001] and [012] (c), resulting in a planar structure. After 14 h, no further growth is observed, and the final crystals are fully developed (d). Their aggregation leads to the formation of the primary aggregate (e), which further aggregates into the final particle (f).

underscoring the significance of fluid dynamics.

Given the heterogeneity in identifying the growth steps, a specific nomenclature will be used in the current study to clearly address all particle components. The term "primary particle" will refer to the basic structure, i.e., the simple result of nucleation. Meanwhile, the term "secondary particle" will refer to the final product of the co-precipitation process, which is the result of all growth phenomena (agglomeration and Ostwald ripening) and can be identified from SEM images as aggregates of flock-shaped primary particles.

4. Chemical parameters influence

The product obtained is influenced by the operating conditions imposed within the reactor. Each parameter contributes differently to the nucleation and growth phenomena, with variations that can be either synergistic or antagonistic. This point should be kept in mind during the discussion, as it highlights that the optimal operating conditions for any synthesized material are not uniquely defined, because of them synergistic interactions. They must be determined by balancing the chelating agent, pH, and temperature together. Therefore, for a fixed stoichiometry, there are many possible recipes to optimize the synthesis.

The following discussion aims to gather information on how these parameters affect particle morphology. It clarifies doubts arising from conflicting or unjustified opinions presented in previous studies. By understanding these effects, there is no need to strictly follow specific recipes in the production of NMC precursors; instead, it is sufficient to balance the parameters based on their impact on the particles produced.

4.1. Chelating agent

The chelating agent is a key parameter in controlling particle shape, size, and stoichiometry ([134,140–148]). The process in question has been demonstrated to induce a delay in the precipitation stage, a phenomenon that has been shown to be advantageous in the context of attaining a homogeneous crystalline structure, as opposed to the formation of a mixture of different phases [134,142]. The necessity of the process in question is linked to the precipitation reactions of cobalt and nickel, which are slower than those of manganese [149,150]. Furthermore, the presence of a chelating agent has been demonstrated to enhance the sphericity and size of particles [131,140–142,145,148–151].

Although its role is well-established, the exact mechanism by which it acts is not clearly defined. Two main hypotheses have been proposed so far:

1. Metals form a complex with ammonia and only later interact with hydroxide groups:

$$xNi + yMn + zCo + nNH_4OH \rightarrow \left[Ni_xMn_yCo_z(NH_3)_n\right]^{2+} + nH_2O \tag{1}$$

$$\left[Ni_xMn_yCo_z(NH_3)_n\right]^{2+} + mOH^-H_2O \rightarrow Ni_xMn_yCo_z(OH)_2 + NH_4OH + (n-z)H_2O \tag{2}$$

In this case, the ammonia complex is an intermediate compound.

2. Metal hydroxides (denoted as M) undergo an equilibrium reaction with the ammonia complex:

$$M(OH)_2 + nNH_3 \leftrightarrow \left[M(NH_3)_n\right]^{2+} + 2OH^- \tag{3}$$

This equilibrium causes a delay in the precipitation process due to competition among ammonia and hydroxide ions toward the reaction with metals.

In 2000, Cho [148] first proposed the reaction mechanism, describing the growth of cathodic precursors with (1 and (2. However, the original study was not directly related to these reactions, as it dealt with the precipitation of nickel, cobalt, and magnesium hydroxides. Therefore, the initial mechanism did not pertain to NMC precursors. In 2004, Lee et al. [142] applied the same reaction scheme when magnesium was substituted with manganese. The justification for this choice was that, in both cases, the reactions produced spherical particles under the influence of the ammonia complex. However, no direct correlation was proven between their study and that of Cho. [148]. Since then, all NMC precursor co-precipitation syntheses have been assumed to follow this reaction scheme.

In 2009, van Bommel et al. [141] introduced a new mechanism, described in the equilibrium reaction in (3. Their proposal differs from the previous one primarily in two key aspects:

- The presence of an equilibrium, therefore the species precipitate and re-dissolves smoothing the particles.
- Ammonia complexes interact with one metal at a time

The latter observation led to further discussion in the same study, highlighting that the reaction constants for ammonia complex formation depend on the metal involved. These differences become more pronounced when the pH is altered. According to Sillén et al. [152], Co and Mn complexation occurs in the pH range of 6–10, while for Ni, it occurs between 4 and 12. This observation is particularly interesting for future studies, as the typical operating pH is around 11, which may not be optimal for all metal-ammonia complexes involved.

After van Bommel et al. [141] introduced their new theory, two possible mechanisms were proposed to explain the co-precipitation process. In 2015, Wang et al. [131] attempted to determine which of the two mechanisms was more accurate or at least provided the best approximation of reality. They took 1g of dried precursor and placed it in a solution of water and ammonia at 60 °C for 2 h. They then compared the resulting solution (based on its color) with two separately prepared solutions: one containing $[Ni(NH_3)_n]^{2+}$ (green color) and the other containing only $NiSO_4$ (blue color). Visual observation revealed no similarity between the colors of the three solutions, indicating that the precursor did not undergo any dissolution. Wang et al. [131] used this result to refute the mechanism proposed by van Bommel et al. [141].

In recent years, further studies have speculated on the topic [149, 150,153]. The studies by Qiu et al. [149] and Xu et al. [150] proposed several tests to examine how the quantity of ammonia influences the quality of the final product. Aside from the quantitative results, their discussions are important, as they explicitly relied on the kinetics proposed by van Bommel et al. [28]. The same approach was used by Lee et al. [153], who supported their discussion with theoretical computations to measure the Q/K ratio of the equilibrium between the metal-ammonia complex and metal hydroxides (which gives information on how much the reaction is far from the equilibrium one [154, 155]). Thanks to these computations, they were able to examine how the rate of precipitation of different metals changes with varying amounts of chelator. They validated their computations with experimental outcomes. Their results also aligned with the theory advanced by van Bommel et al. [141].

Lee et al. [153] and Xu et al. [150] also identified an additional effect of ammonia content: it increases the occurrence of Ostwald ripening, allowing secondary aggregates (the final particles) to be smoothed through dissolution and precipitation phenomena. Although they agreed on this point, they attributed the effect to different causes. Lee et al. [153] argued that it is a manifestation of the equilibrium proposed by van Bommel et al. [141], while Xu et al. [150] identified the cause of Ostwald ripening as the minimization of surface energy.

Although these studies are promising, they all share a significant limitation: their kinetic models are derived based on thermodynamic evaluations. However, it cannot be assumed that kinetic behavior and thermodynamic predictions always align.

While the general consensus currently supports the kinetics proposed by van Bommel et al. [141], there have been no further studies on the reaction mechanism, suggesting that the process is far from fully understood. Additionally, uncertainties remain regarding how different stoichiometries might affect the reaction mechanism. It is reasonable to expect that varying the metal ratios would also shift the equilibrium, as observed by Han et al. [156]. Aware of this gap, this section will approach the problem through practical analysis. Many studies have explored the effect of chelating agents during precipitation, so the following discussion will focus on identifying the operating conditions that produce materials with the best performance.

Let us first examine how the chelating agent generally affects particle growth. In both proposed models, as shown by numerous studies, the chelating agent competes with hydroxide groups for metals. The higher the quantity of ammonia, the less metal hydroxide precipitation occurs. Therefore, solutions with lower NH_3/OH^- ratios will undergo faster nucleation, preventing primary particles from packing uniformly [131]. The resulting particles will not have a homogeneous size and shape distribution. Wang et al. address this behavior in the context of agglomeration dynamics. In this framework, the optimal particle morphology is said to be reached only when there is a balanced relationship between shear stresses and the rate of agglomeration. This rate is influenced by the dimensions of the primary particles, which are, in turn, influenced by the nucleation and growth rates. Additionally, nucleation events are more frequent, and higher reagent consumption limits particle growth, leading to smaller particles. Thus, a smaller NH_3/OH^- ratio is typically associated with smaller particle sizes [131, 142,145,146].

Rather than focusing solely on the chelating agent quantity, the parameter to investigate is the NH_3/OH^- ratio. Typically, this involves controlling the pH while fixing the amount of ammonia [142,145–147]. However, since using NaOH to control pH does not accurately account for the OH^- quantity, this method is not suitable for quantitative evaluations. In recent years, studies have relied on using an excess amount of chelator to ensure a perfect equilibrium between the ammonia complex and the metal hydroxides [150,153]. This is necessary to prevent instantaneous precipitation when NaOH drops hit the surface of the solution, causing a localized increase in pH.

All of these considerations make sense if the quantity of ammonia is enough to make complexes with all the metals present in solution. Since the nature of metal ammonia complexes is not well understood, there is no way to forecast what has to be the proportion between these two components. Different studies [151,157] focused on this parameter, and they identify 1 as a satisfying NH_3/M ratio (see Fig. 8).

The mechanisms discussed until now make evidence that this is not enough to detect the best ammonia quantity. As underlined before the most important thing is to have a reaction between metals and ammonia that is faster than the direct precipitation. Assuming, for simplicity, they are elementary reactions, the rate of reactions can be modelled as:

$$r_{comp} = k_{comp} c_M c_{NH_3} \quad r_{prec} = k_{prec} c_M c_{OH} \tag{4}$$

Where r_{comp} and r_{prec} are respectively the rate of reaction of the complex formation and of the precipitation, k_{comp} and k_{prec} are the corresponding kinetic constants, and c_x is the concentration of the component. Then, to favor the complex formation ($r_{comp} > r_{prec}$) it is necessary to have:

$$\frac{r_{comp}}{r_{prec}} = \frac{k_{comp} c_{NH_3}}{k_{prec} c_{OH}} > 1 \tag{5}$$

Since there are no information about the kinetic constants, for now the only way to have a preferential complexation is to manipulate ratio c_{NH_3}/c_{OH}.

Despite that, only Wang et al. [131] explicitly controlled the NH3/OH^- ratio, making it worthwhile to focus on their results, even though these pertain to the LNMO cathode material. They tested six different $NaOH/NH_3{\cdot}H_2O$ ratios (2:3, 1:1, 3:2, 2:1, 5:2, 4:1). The results

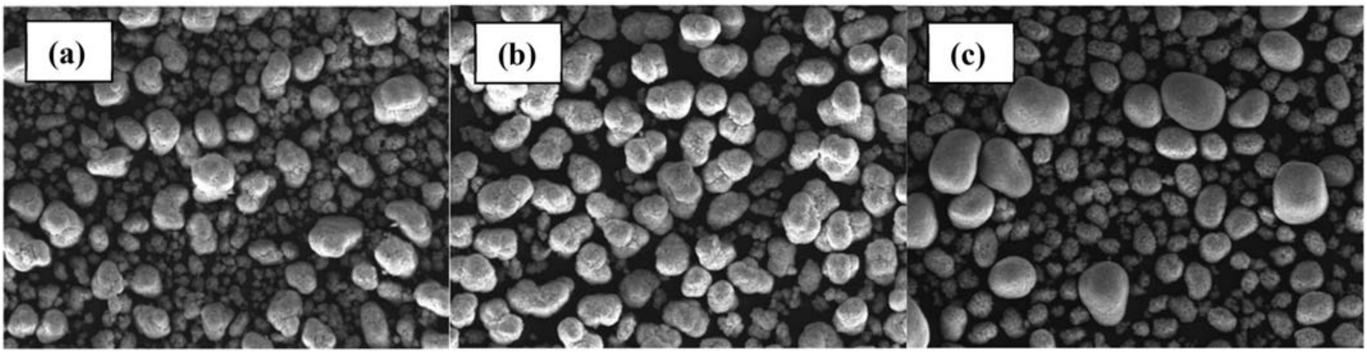

Fig. 8. These are the particles obtained by Vu and Lee [157] changing the ratio between ammonia and metals. 0.8 (a), 1(b), 1.2(c). By examining the sphericity and homogeneity of the material obtained, it is possible to identify 1 (b) as the optimal condition for the reaction.

showed spherical particles with a smooth surface and good dimensions (20 μm) only at the 1:1 ratio (see Fig. 9). As the ratio shifted toward more NaOH, the particles became smaller and lost their sphericity.

It is also noteworthy that when $NH_3 \cdot H_2O$ was in excess, the particles became heterogeneous and smaller (around 7 μm) [131]. The authors did not provide an explanation for this behavior. However, this result could be useful in future studies to identify cases where ammonia content is excessive.

The procedure presented above offers an approach to determining the optimal quantity of chelating agent.

Unfortunately, the studies on this topic are not extensive enough to provide definitive values for NMC, particularly given the dependence on metal stoichiometry.

A proof of the last observation is provided by Fig. 10. It shows how the tap density and sizes are affected by the ratio between the chelating agent concentration once with metals (Fig. 10a and c) and once with the precipitant (Fig. 10 (b) and 10d). It can be observed that there is no obvious trend, since the p-value is always greater than 0.05 when the metals are precipitated as hydroxides.

This indicates that the high variability used in previous studies [134, 140–148] limits the possibility of a quantitative evaluation of the effects of the chelating agent on the obtained precursors.

4.2. pH

As introduced before, the synthesis reaction relies on the interaction

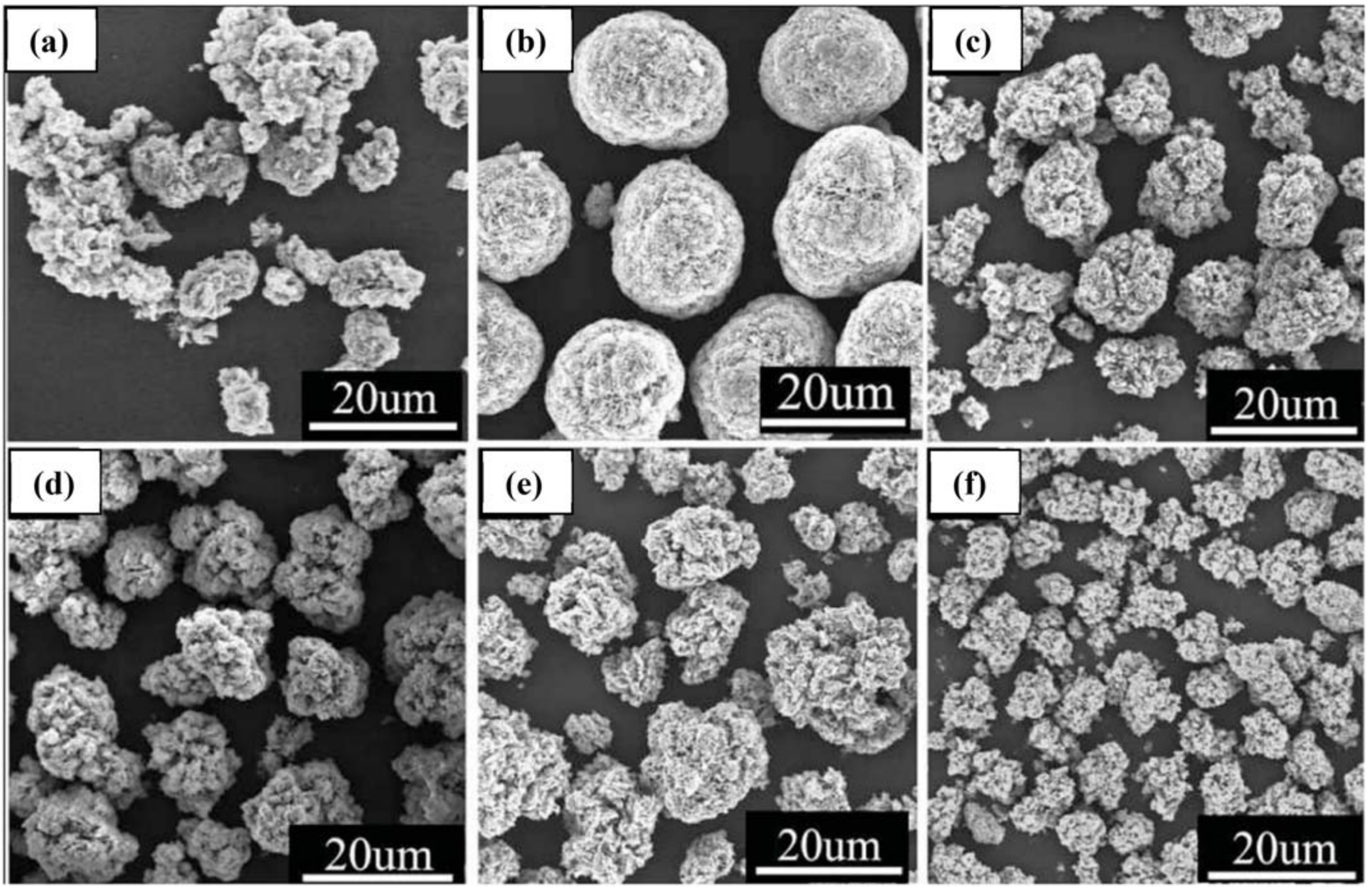

Fig. 9. These are the results collected by Wang et al. [131] varying the ratio between OH^- and NH_3H_2O. 2:3 (a), 1:1 (b), 3:2 (c), 2:1 (d), 5:2 (e), 4:1 (f). By examining the homogeneity and sphericity of the particles obtained, the best precursor is achieved when ammonia and hydroxide anions are used at the same molarity.

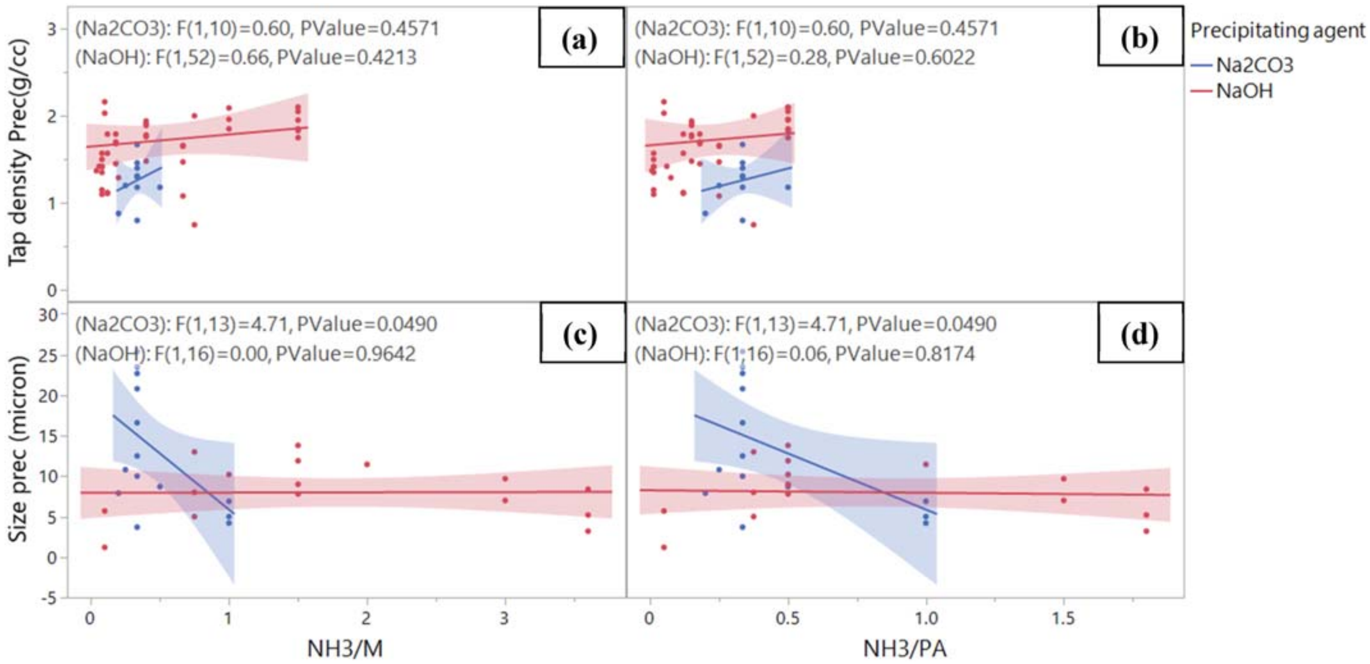

Fig. 10. These images are obtained with a statistical analysis of Table S1. It shows the effect of the chelating agent on the precursor tap densities and sizes. The results are classified based on the precipitant used. As discussed in the text, the focus is not simply correlated to the chelating agent concentration, but to its ratio to the metal and precipitant concentrations. Figures (a) and (b) show the effect on tap density, while figures (c) and (d) show the effect on size.

between metal ions and hydroxide ions; $[OH]^-$ anions play a fundamental role in the reaction kinetics. An increase in pH results in a higher concentration of this reactant, leading to a faster reaction. However, speeding up the reaction does not enhance the conversion, or at least not in a detectable way, since the synthesis occurs under transport control (see the section on nucleation and growth). Instead, it directly affects the morphology of the particles produced. The reason for this behavior lies in the precipitation mechanism presented in the nucleation and growth section; an increase in the reaction rate leads to a higher supersaturation rate, causing nucleation phenomena to occur more frequently. In this condition, the reactant is consumed to produce many nuclei, leaving insufficient material for all the grains to grow as desired [158]. As a result, some primary particles will reach the proper dimensions, while others will remain smaller. This heterogeneity limits the aggregation phenomena, producing particles that are not uniform in shape and size. Evidence of this behavior can be seen in the images from Shen et al. [131,145] (Fig. 11).

In the opposite case, where a small quantity of nuclei is produced, the primary particles grow too large, reducing their aggregation and producing crystals that are not properly packed. The resulting particles exhibit a complex structure that deviates from the usual spherical shape. Additionally, they also possess non-homogeneous dimensions. It is possible that increasing the reaction time and consequently extending the smoothing process could resolve the issue with sphericity, but this has not been tested yet. Even so, the operation time would need to be longer, making this approach less ideal.

In both cases described, the products obtained are not satisfactory. They represent two extreme situations: one where the pH is too high, and the other where the pH is too low. Many intermediate situations may occur, producing something close to the target properties, but they still have some drawbacks. Previous studies ([134,140,142,145,151, 157,159–161]) have shown that among all these intermediate conditions, there is always a pH value at which a satisfactory cathode precursor can be obtained.

Collecting all these results, there is no evidence of a linear dependence between the optimum pH value and other synthesis operating conditions. The same observation can be extended to the stoichiometry of nickel, cobalt, and manganese. For example, consider the studies by Ren et al. [159], Hu et al. [151], Liang et al. [160], and Shen et al. [145], where the optimum pH values were 10.8, 11, 11.2, and 11.2, respectively. Although all of these studies dealt with NMC622, the pH values that produced the best material differed.

Furthermore, comparing these results with those for NMC811 ([157]) and NMC111 ([134,140,142]), it is possible to observe that in some cases, the best pH values coincide despite the differences in stoichiometry.

This analysis highlights how much this parameter is significantly affected by the operating conditions and how difficult it is to predict the optimum pH without prior experience. The range in which this parameter must be identified is typically between 10 and 12.

The key takeaway from this paragraph is that once the pH value that produces the desired product is identified, it must be maintained for the entire duration of the synthesis; this consideration will be of great importance in the paragraph discussing the various reactor configurations.

4.3. Temperature

Temperature is a key parameter affecting both thermodynamics and kinetics; this discussion will address both, starting with thermodynamics. Thermodynamically, temperature determines the process's feasibility by identifying the operative range in which reactions occur. This is crucial for limiting the formation of impurities. According to Vu et al. [157] and Liang et al. [160], undesired products are related to the autoxidation of manganese hydroxide, for which Nichols and Walton [162] identified two possible reaction mechanisms:

4.3.1. 1st MECHANISM

$$6Mn(OH)_2 + O_2 \leftrightarrow 2Mn_3O_4 + 6H_2O \tag{6}$$

$$4Mn_3O_4 + O_2 \leftrightarrow 6MN_2O_3 \tag{7}$$

$$2Mn_2O3 + O_2 \leftrightarrow 4MnO_2 \tag{8}$$

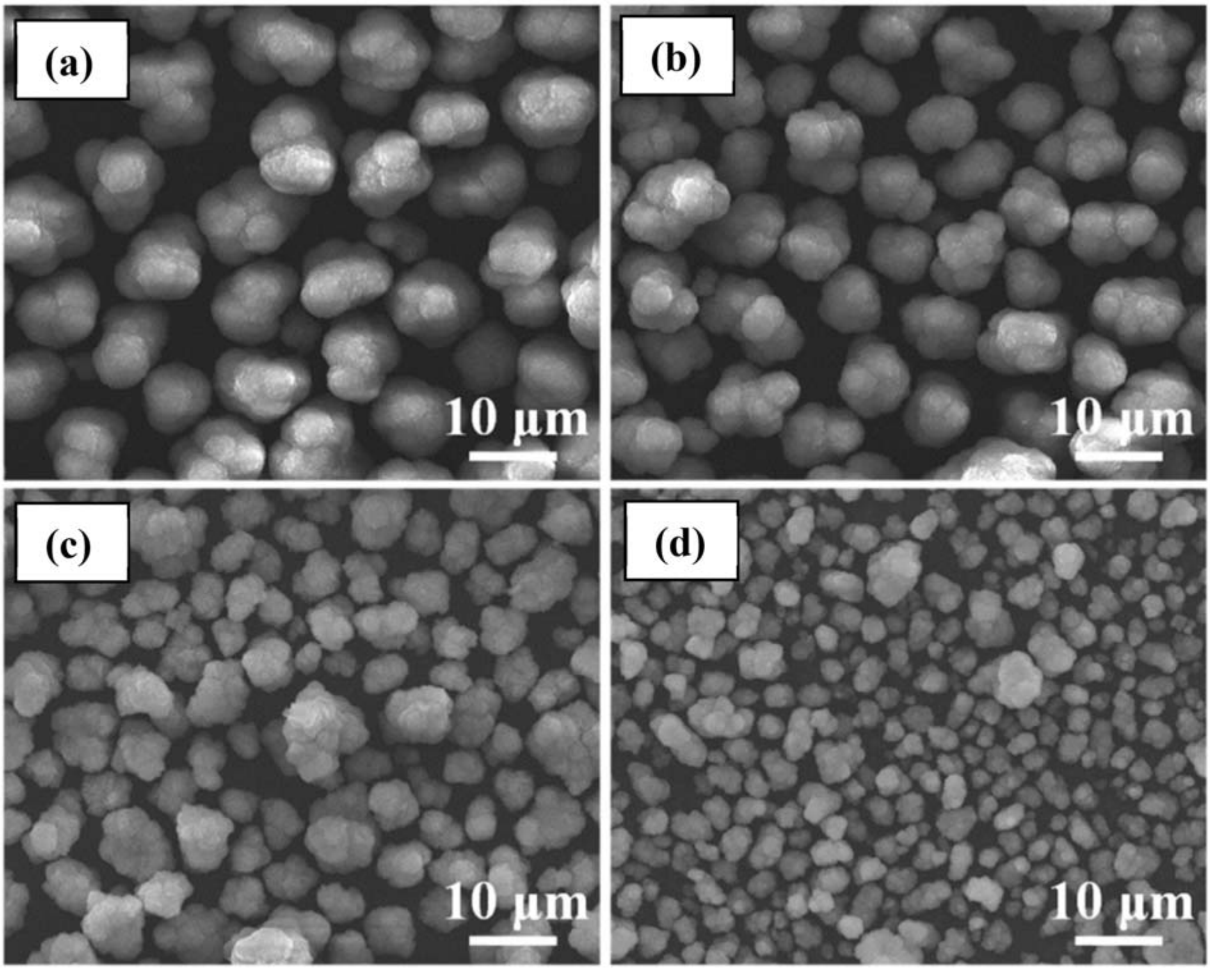

Fig. 11. The images taken by Shen et al. [145] demonstrate how particle morphology is influenced by pH: 11 (c), 11.2 (d), 11.4 (e), and 11.6 (f). Particle dimensions decrease as pH increases. Starting at pH 11, where the precursors are excessively large, their size reduces as this parameter increases. The authors identified the material obtained at pH 11.2 as the optimal one; its dimensions, morphology, and sphericity maximize the tap density, thereby enhancing performance.

4.3.2. 2nd mechanism

$$2Mn(OH)_2 + O_2 \leftrightarrow 2MnO_2 + 2H_2O \tag{9}$$

$$MnO_2 + Mn^{2+} + H_2O \leftrightarrow Mn_2O_3 + 2H^+ \tag{10}$$

$$Mn_2O_3 + Mn^{2+} + H_2O \leftrightarrow Mn_3O_4 + 2H^+ \tag{11}$$

The temperature must be maintained within an operational range to avoid these reactions. Previous studies [162,163] have shown that, regardless of other parameters, manganese hydroxide autoxidation cannot occur at temperatures below 60 °C under an inert atmosphere. Therefore, thermodynamics imposes an upper limit on the process; exceeding this temperature compromises the synthesis due to the production of excessive impurities [164].

Additionally, this observation highlights the necessity of working under an inert atmosphere to prevent oxidation.

Next, it is important to consider how temperature influences reaction kinetics. This topic is closely related to the discussion on the influence of pH, as, according to Arrhenius's law [165], temperature affects the reaction rate similarly to reactant concentration, albeit with a different mathematical dependence (temperature affects reaction velocity exponentially, while reactant concentration follows a power series dependence). The higher the temperature, the faster the reaction. This influence can be observed in the dimensions of the primary particles, similar to the pH discussion. If the temperature is too high, nucleation phenomena are enhanced, reducing the growth of some primary particles and leading to heterogeneous dimensions that hinder aggregation. Conversely, if the temperature is too low, primary particles will grow too large and will not be able to pack properly. Within the range defined by these extreme conditions, there is always an intermediate temperature at which the product will have homogeneous dimensions and sizes. This behavior is demonstrated in the studies by Vu et al. [157] and Liang et al. [160], which are the only ones that tested different temperatures (see Fig. 12).

The aforementioned effects are predominantly associated with the geometry, as the statistical analysis reveals no discernible impact on the precursor size or tap density (Fig. 13). Notwithstanding, there is evidence of the effect of temperature on the cation mixing. Increasing the temperature results in a reduction of cation mixing, with optimal conditions being achieved at 60 °C.

As a result, it can be concluded that the operational conditions for the co-precipitation synthesis of NMC precursors should be set within the temperature range of 50 °C–55 °C to achieve spherical, homogeneous particles with uniform distribution.

5. Physical parameters influence

Physical parameters can be divided into two main categories: those affecting the synthesis step and those related to post-synthesis treatments.

The parameters affecting the synthesis step include agitation and

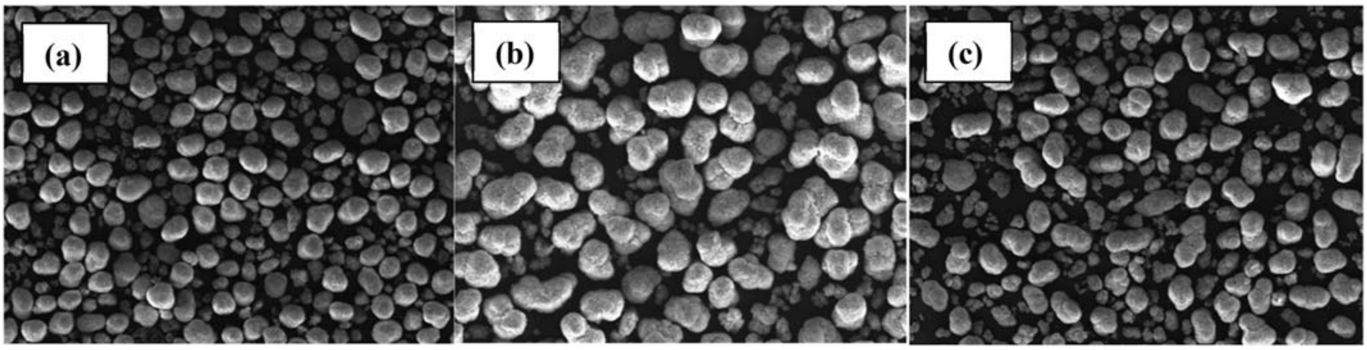

Fig. 12. These are the precursors obtained by Vu and Lee [157] testing three different temperatures: 45 °C (a), 50 °C (b), 55 °C (c). Particles synthesized at 45 °C and 55 °C are smaller and exhibit less spherical morphology compared to those obtained at 50 °C. Consequently, under these conditions, 50 °C can be identified as the optimal temperature parameter for the reaction.

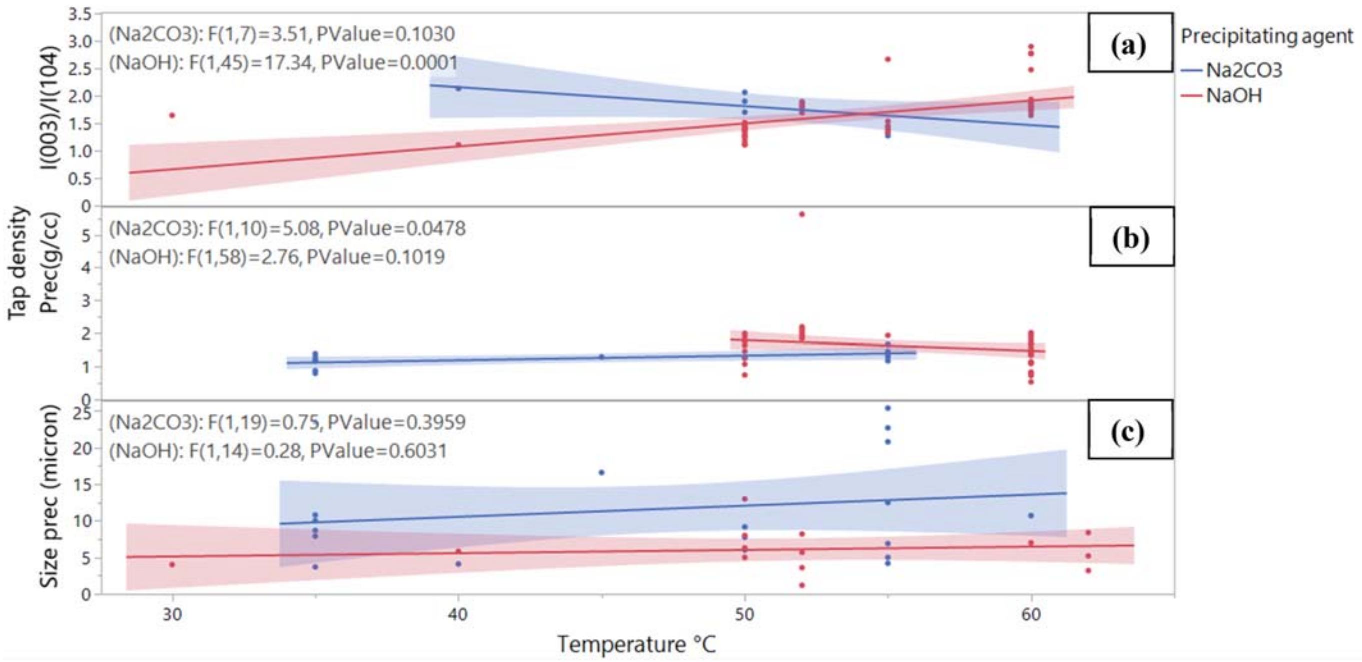

Fig. 13. This figure illustrates the impact of temperature on the cation mixing (a) of the final product and on the tap density (b) and size (b) of the precursor. The sole parameter that evinces a discernible trend is tap density.

operative time. On the other hand, post-synthesis treatments are specifically related to the calcination temperature.

5.1. Agitation

NMC precursor co-precipitation is highly dependent on stirring velocity.

As previously discussed in the section on nucleation and growth, the reaction occurs extremely fast and is limited by transport phenomena. However, transport effects on nucleation cannot be strictly related to agitation, as no study has yet tested the influence of fluid dynamics on the conversion rates and aggregative phenomena.

Nevertheless, stirring velocity remains crucial as it affects the aggregation steps. This influence is evident on both microscopic and macroscopic scales.

The only study that investigated the microscale effects is by Vu and Lee. [157]. Their high-resolution images reveal how primary particles are packed, showing that increased agitation leads to smaller primary particles. This is likely because they do not have enough time to grow before aggregation. However, the differences are not substantial, and the primary particles maintain a planar shape across different agitation conditions.

The most significant impact of stirring velocity is on the macroscopic scale. It affects the smoothing step, which is the final stage of synthesis. Higher agitation increases the impacts between particles and shear stresses, thereby accelerating the smoothing process to achieve spherical particles with a flat surface. Consequently, data from studies [142,157,159,160] agree that higher agitation speeds up the attainment of optimal particle morphology.

As demonstrated in Figs. 14 and 15 evidence of these effects is apparent on the particles' shape. The statistical analysis in Fig. 16 demonstrates that this is not the case for other parameters. In this instance, the heterogeneity of the products documented in the extant literature engenders an analysis devoid of any significant trend. This phenomenon can also be attributed to the variable used to identify the agitation. The impeller stirring rate does not generate equivalent turbulence in every reactor; it is contingent on the reactor itself and the dimensions of the impeller. Given that extant studies uniformly designate the stirring rate as a reference for the agitation, this discussion is obliged to rely on it. However, a thorough examination reveals that the

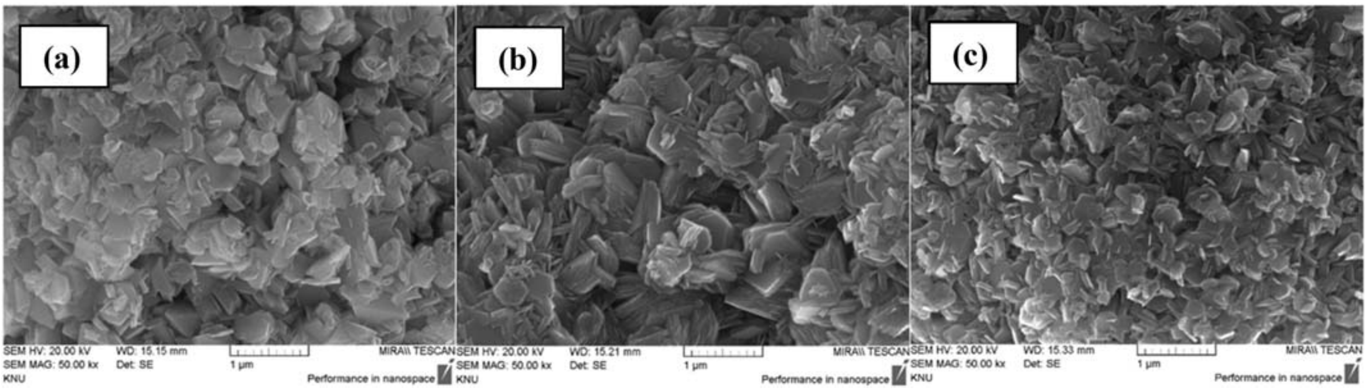

Fig. 14. This picture taken by Vu and Lee [157] shows how crystallites change varying the agitation: 500 rpm (a), 600 rpm (b), 800 rpm (c). Moving from 500 rpm to 600 rpm flock crystals became thinner, as if agitation primarily affects the aggregation between the planar basic crystals. Moving from 500 rpm to 600 rpm, flock crystals became thinner, suggesting that agitation primarily influences the aggregation between the planar basic crystals. With a further increase to 800 rpm, the two preferential growth directions are also affected, reducing their surfaces. This results in smaller crystals that are able to pack more efficiently.

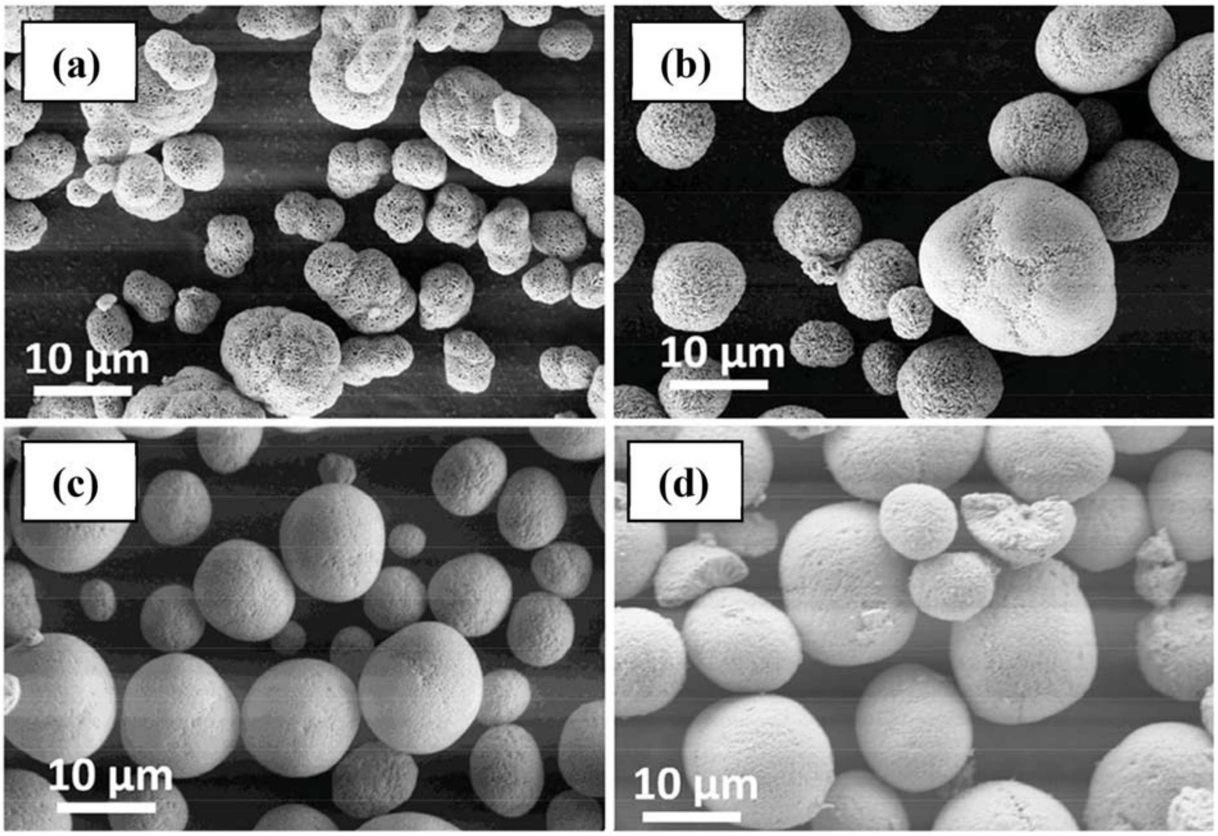

Fig. 15. As illustrated in the images captured by Ren et al. [159] It is possible to identify how the sphericity of the particles is enhanced by increasing the stirring rate until the particles begin to break. Four distinct agitation protocols were employed: 600 rpm (a), 800 rpm (b), 1000 rpm (c), and 1200 rpm (d).

cathode cation mixing, the precursor tap density, and the size remain unaltered by the agitation variations applied.

Correlating the evidence presented herein is a subject meriting further study. Fig. 15a with the preceding observations on the impact of the stirring rate. As previously discussed, agitation affects the primary particles' characteristics but does not influence the cation mixing. This observation suggests the absence of a correlation between the characteristics of the primary particles and the order of cation mixing. It is important to note that this observation is preliminary, and further studies are necessary to provide definitive evidence.

The only limitation is particle integrity. Ren et al. [159] demonstrated that a stirring velocity of 1200 rpm causes particle breakage, making 1000 rpm the optimal value observed in all cases.

Additionally, the type of impeller used is also relevant to agitation. Zhu et al. [135] conducted a study testing four different types of impellers: two radial, one axial, and one a combination of radial and axial.

Interestingly, unlike previous findings, changing the type of impeller affects primary particle morphology (see Fig. 17). The study found that using axial impellers produces acicular primary particles, which can be packed more effectively than the typical planar ones. This results in particles with higher sphericity and a smoother surface.

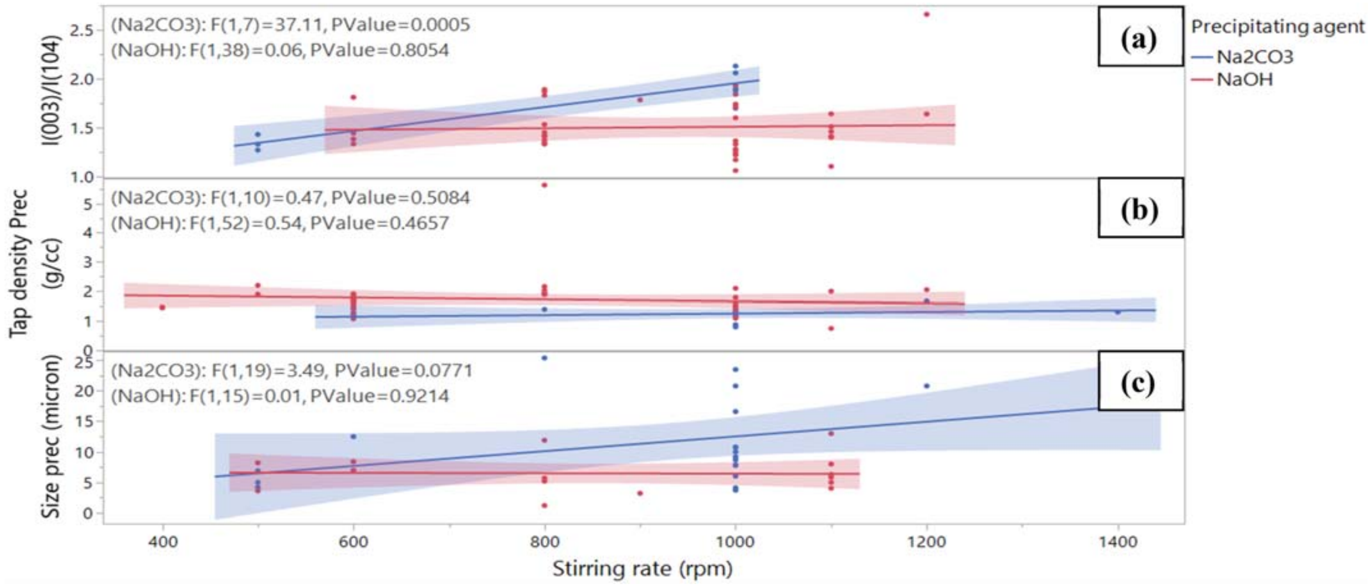

Fig. 16. The following statistical analysis was conducted to determine the effect of the stirring rate on the cation mixing of the cathode (a), the precursor tap density (b), and the size (c).

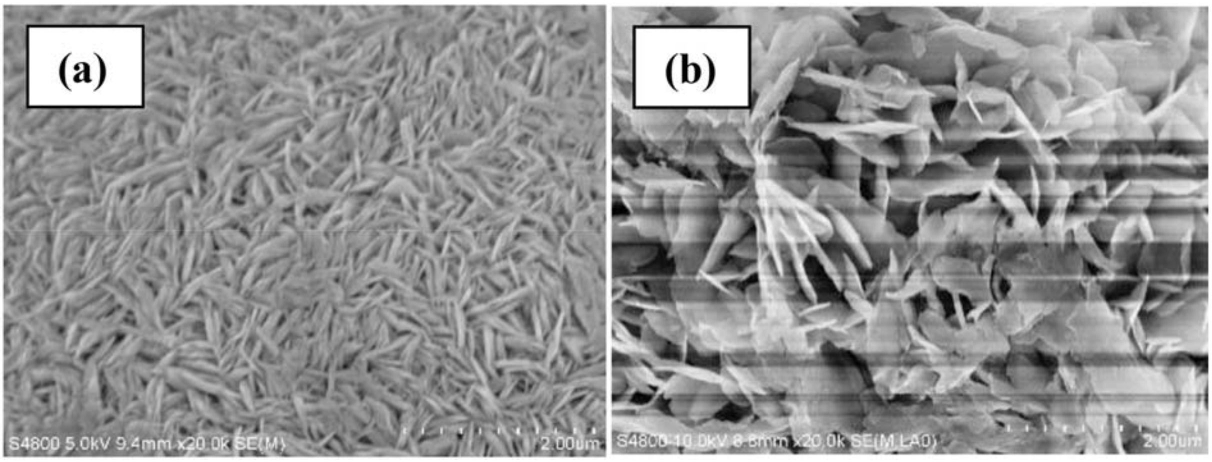

Fig. 17. These pictures taken by Zhu et al. [135] prove that agitation may be also used to influence the crystallites structure. They compared the materials produced using axial impellers (left), which exhibited an acicular shape, with the flock-like materials obtained using radial impellers (right).

5.2. Operative time

Before diving into the evaluation of this parameter, it is important to understand that “operative time" is a general term that can vary depending on the apparatus used. This distinction will be clarified in the paragraph on reactors. For now, this parameter will be referred to as the duration for which a species is confined inside the reactor, indicating the amount of time reagents have to react from the moment they enter the reactor until they exit.

Although many studies have explored the effects of time on particles ([131,134,140,141,145,146,151]), none have investigated times shorter than 10 min. This is why the nucleation model discussed earlier relies on general knowledge of crystallization rather than specific empirical evidence for this case. The shortest time investigated is 10 min (Yang et al. [132]), which only shows that primary particles have formed, grown, and begun to aggregate. No useful information on nucleation phenomena can be derived from this.

Nevertheless, studies on operative times are still valuable as they identify key stages in the synthesis process (see Fig. 18), which can be summarized into five consecutive steps:

- Initial 10 Minutes: Nucleation, growth, and formation of small aggregates occur. While no detailed evidence is available for this initial period, a picture taken at 10 min by Yang et al. [132] shows that simple aggregates are already visible.
- 10 Minutes to 6 Hours: Primary particles and aggregates formed in the initial 10 min continue to interact, forming increasingly complex structures. At this stage, particles are still too simple and heterogeneous to be clearly recognized.
- 6 to 8 Hours: Simple aggregates consolidate into more complex structures, leading to the formation of an initial form of the product particles.
- 8 to 15 Hours: Particles continue to grow and aggregate. By the end of this period, the particles have dimensions comparable to the final product (around 10 μm), though their shape is still not ideal due to a multilobed morphology resulting from recent aggregation phenomena.
- 15 to 30 Hours: A smoothing procedure is initiated, resulting in spherical particles with a smooth surface. At the conclusion of this stage, the particles exhibit dimensions ranging from 10 to 15 μm, contingent upon the prevailing operational parameters. These

particles manifest a spherical geometry with a smooth surface. The statistical analysis presented in Fig. 19 (b), where a substantial increase in tap density with reaction time is discernible. This enhancement is attributable to the enhancement of the particle sphericity, which facilitates more efficient packing, thereby increasing tap density.

Some studies also provide images of particles obtained with longer operative times [135,151]. These results suggest that after 30 h, the particles no longer change significantly, indicating a balance between smoothing processes (such as particle collisions and shear stress) and growth (Ostwald ripening).

This step is ordinarily executed as the final one in precipitation reactions. Nevertheless, a further phenomenon occurs for reactions that are longer in duration: recrystallization [166]. This phenomenon has typically been observed in the context of crystal aging, yet it remains largely unexamined and unreferenced in the extant literature. It does not contribute to the development of the particle morphology; rather, it is concerned with the structural characteristics of the material. The process of nucleation is typically the most expeditious phase of precipitation, manifesting as an almost instantaneous occurrence. In this regard, kinetics supersedes thermodynamics. This process gives rise to a crystalline structure characterized by a substantial quantity of strains [166]. The only method for eliminating them is to allow sufficient time for the material to reach thermodynamic equilibrium (minimize the system energy). This phenomenon is analogous to the process of recrystallization, wherein the particles, once formed, undergo a structural relaxation towards thermodynamic equilibrium. It is noteworthy that this process can necessitate an extensive reaction time.

This phenomenon, however, remains largely unexamined due to the absence of straightforward methods for observing this structural relaxation. The statistical analysis presented in Fig. 19 is a unique instance in which the structural effect can be assessed. As illustrated in Fig. 19 (a), a substantial correlation is evident between reaction time and the reduction of cation mixing. Given that the latter is a detrimental characteristic related to the structure of the material, it is reasonable to hypothesize that the strain reduction due to the recrystallization is the cause of the reduction in cation mixing.

This phenomenon may offer insights into growth phenomena and provide an important contribution toward the optimization of the production of NMC cathodes. However, further studies are needed to draw definitive conclusions.

Thus, this area remains a promising field for future research.

6. Thermal treatment

As stated in paragraph 2.6, the production of NMC through co-precipitation does not culminate with the precursor; rather, the precursor must undergo a thermal treatment. During this treatment, two key phenomena occur: mixed-metal hydroxide crystals are converted into oxides, and lithium is intercalated into the metal matrix.

The calcination process consists of two distinct steps. In the first step, the metal matrix undergoes a phase transition from hydroxide to oxide crystal structures at a relatively mild temperature (400–500 °C) [167]. This transition precedes lithium intercalation, as lithium ions (Li^+) must diffuse into the oxides for two reasons. First, the target material is an oxide matrix with lithium intercalated between its layers. Second, Li^+ ions diffuse more readily in an oxide matrix compared to a hydroxide matrix. Concurrently, lithium melts and partially diffuses into the matrix, lowering the temperature required for subsequent steps [168]. This

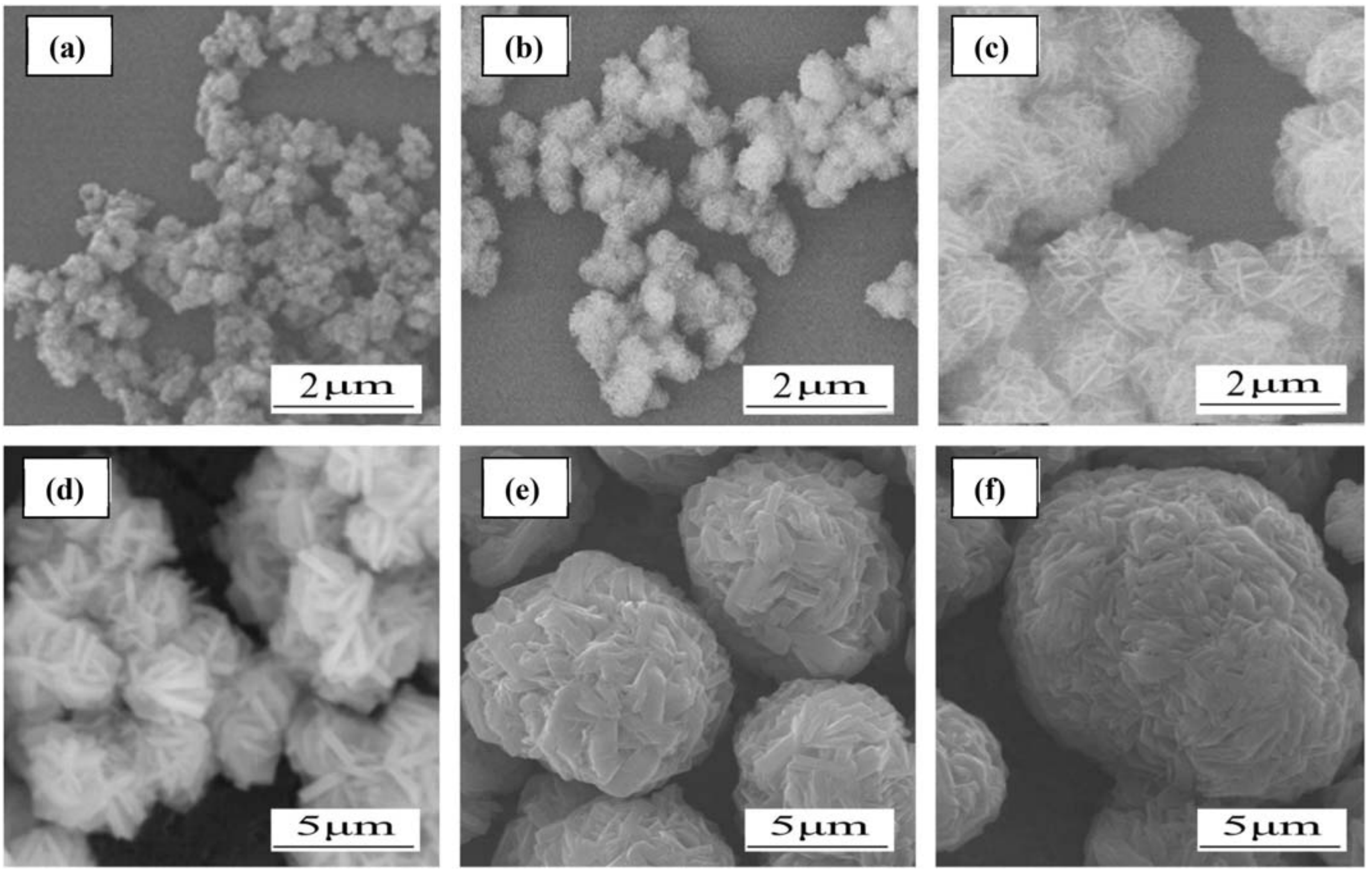

Fig. 18. These pictures show how particles characteristics changes by varying the operative times [132]. The primary aggregates form within 10 min (a). After 30 min (b), they remain primary aggregates but have grown significantly in size. The first larger aggregates with flock crystals begin to appear at 1 h (c) and continue to develop at 2 h (d). Final particles are obtained after 10 h (e), achieving a more refined shape by 18 h (f).

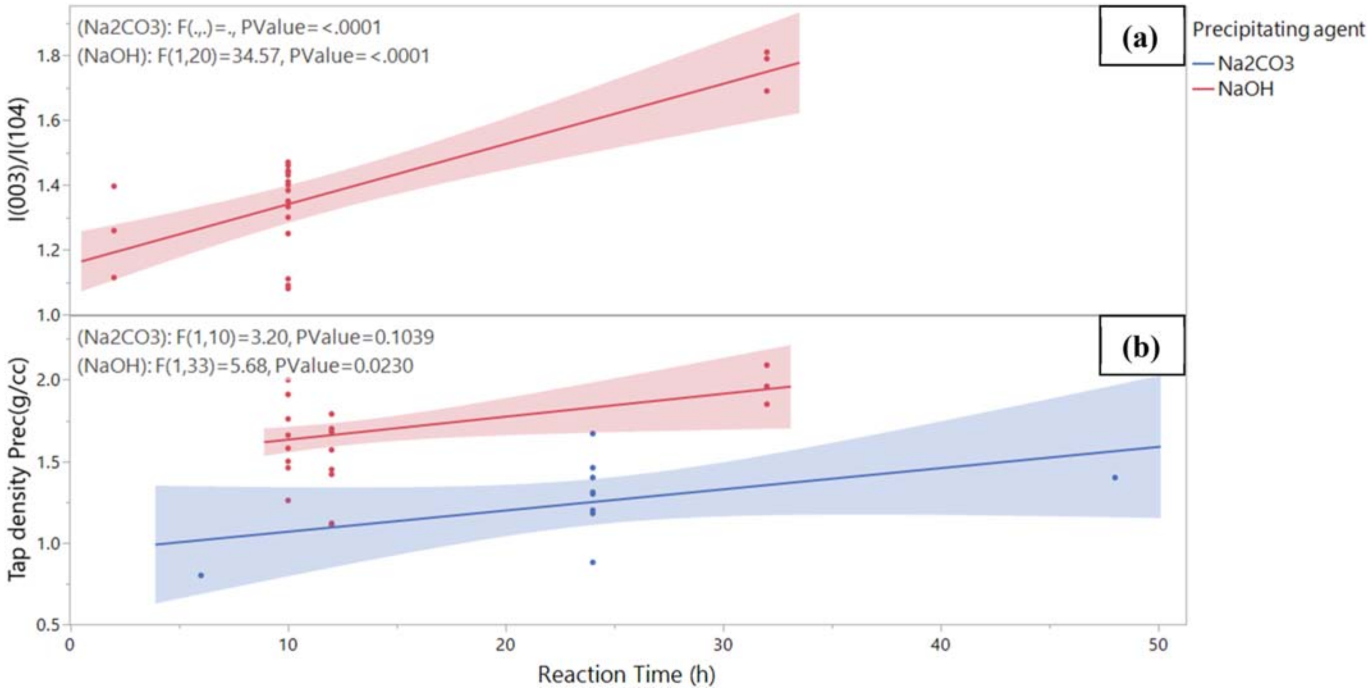

Fig. 19. The trends illustrate the behavior of cation mixing (a) and precursor tap density (b) as a function of reaction time. A substantial correlation is observed in both scenarios, as evidenced by the statistical analysis of Table S1.

step typically lasts about five to 6 h.

In the second step, lithium ions diffuse into the crystalline structure of the metal matrix. This requires a higher temperature (at least 700 °C) and a longer duration (at least 10 h).

The ensuing paragraphs will delve into the impact of calcination temperature, duration, and other pivotal parameters on the material

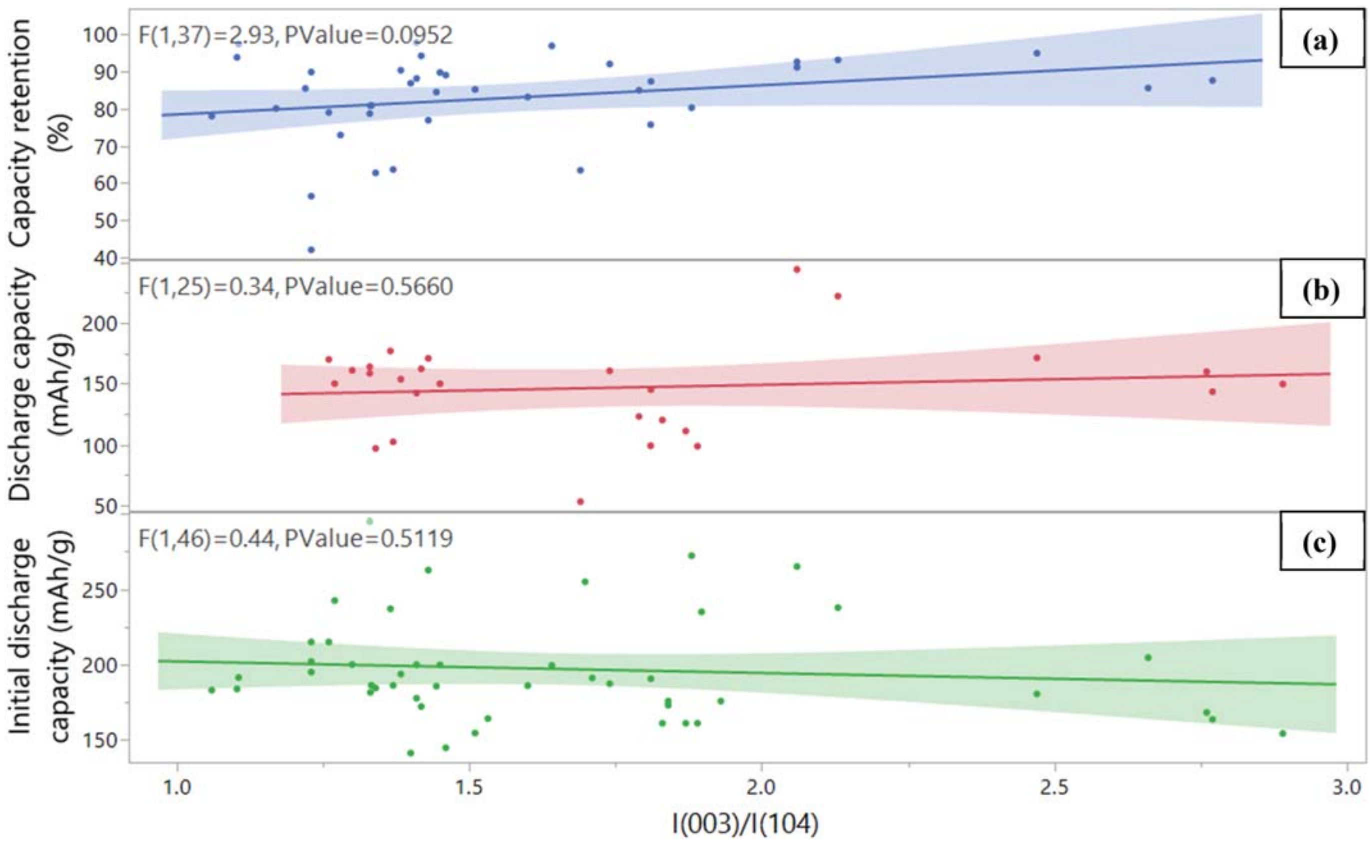

Fig. 20. This figure presents the statistical analysis that examines the correlation between the I(003)/I(104) ratio derived from the XRD characterization and the electrochemical performances, including capacity retention (a), discharge capacity (b), and initial discharge capacity (c).

obtained from physical and electrochemical standpoints.

The paragraph on the temperature effect is based on previous studies that provide evidence of its effect by comparing the cathodes obtained with different conditions. A distinction must be made between the two paragraphs under consideration, as the other parameters that play a key role in the thermal treatment have not been investigated through explicit comparison of materials obtained under different conditions. Consequently, the present study will posit the following argument, as substantiated by the statistical analysis presented in Table S1. This argument is proposed given the lack of alternative comparative approaches in the current body of literature.

Nonetheless, the analysis of cathode materials involves greater complexity than that of precursors, as the outcomes of characterization may vary depending on the equipment and the operator.

Consequently, a direct comparison of the absolute values obtained from different studies may not be sufficiently reliable to draw definitive conclusions.

For instance, the assessment of cation mixing employs XRD analysis. When the intensity ratio of the 003 to 104 peaks exceeds 1.2, there is minimal cation mixing. It is imperative to maintain an I(003)/I(104) ratio that exceeds this threshold in order to ensure the preservation of optimal material qualities [142,157,160,161].

Fig. 20 indicate an absence of correlation between electrochemical performance and the I(003)/I(104) ratio measured. This absence of correlation is evidenced by the analysis of data from disparate studies. This discrepancy may be partially explained by the intrinsic heterogeneity of coin cells used under conventional testing conditions. Consequently, comparisons made across studies are only indicative and should be interpreted with caution.

Analogous conclusions can be extrapolated from an examination of capacity retention. The range of regulatory and market targets for these performances complicates the identification of an indicative value that can be satisfied. The objective of preserving 80 % capacity retention following 1,000 cycles is regarded as the fundamental benchmark. However, due to operational constraints, the majority of studies examine capacity retention following 100 cycles (Fig. 21).

While this is not the desired 1,000 cycles, the 80 % retention threshold is typically achieved. Coin cells may experience degradation phenomena that are less prevalent in full cells. For instance, coin cells frequently use metallic lithium anodes, which differ from the anodes in commercial full cells. Therefore, while direct comparison with commercial materials may be inappropriate, coin cells remain useful for relative comparisons within individual studies.

In the absence of comparative studies investigating all relevant operative parameters, the statistical analysis presented in Table S1 provides the only available approach to identifying the most effective calcination conditions.

6.1. Calcination temperature

Once the lithium source is selected, the optimal operating temperatures must be determined. The literature on ideal temperatures for the first step is limited, as many studies combine both steps into a single high-temperature procedure [161]. However, this approach often leads to increased degradation, making it unsuitable for nickel-rich materials. If the desired stoichiometry is not achieved in a two-step process, the duration or temperature of the first calcination step may need adjustment.

The second step involves lithium-ion intercalation into the crystalline structure, with key indicators of success being the degree of hexagonal crystalline order and cation mixing. Studies [142,157,160] indicate that increasing the calcination temperature improves hexagonal order, as observed via XRD characterization (the order is determined by the degree of separation between peaks 006/012 and 108/110.).

However, materials with the highest I(003)/I(104) ratios have shown improved capacity retention, which is attributed to reduced cation mixing—even when these materials were not synthesized at the highest temperatures [142,157,160,161]. This observation supports the

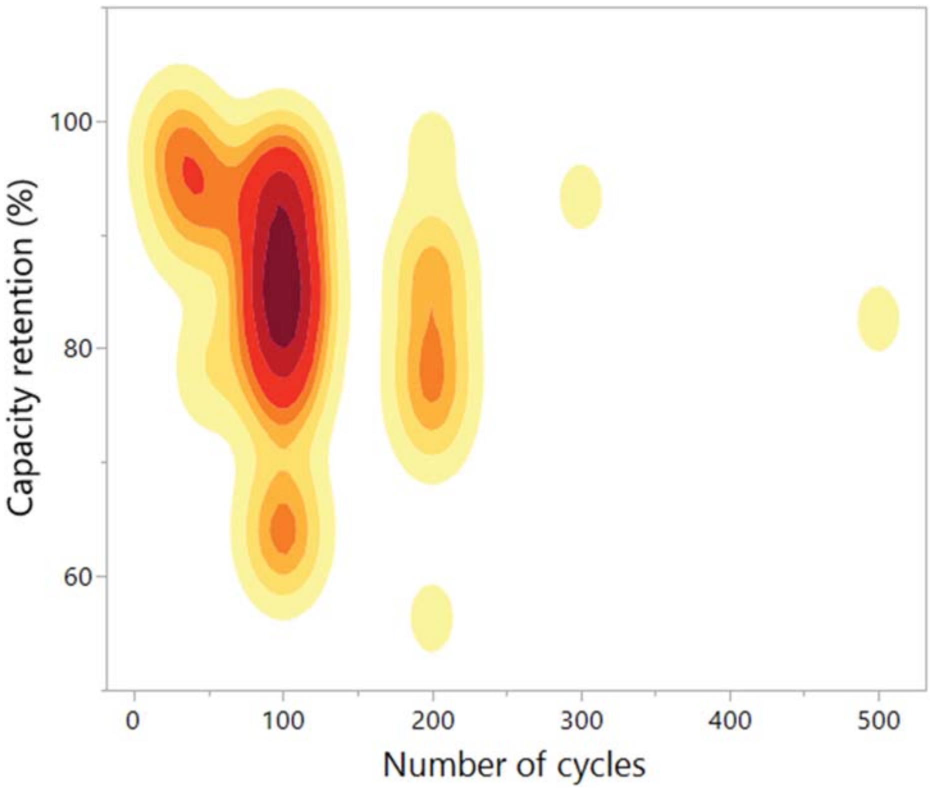

Fig. 21. The contour plot indicates that the vast majority of studies enumerated in Table S1 utilize cycle number 100 as a reference point to assess the capacity rate.

hypothesis that cation mixing may represent a thermodynamically favorable state in NMC materials, as it potentially minimizes the crystalline structure's energy. Therefore, matrix order alone may not reliably indicate the extent of cation mixing.

At higher calcination temperatures (>900 °C), primary particles undergo melting and coalescence, leading to large grains within the crystalline structure. While this enhances crystallinity and structural order [167,169,170], the grains lose their precursor orientation, increasing anisotropy. Consequently, grain boundaries act as barriers to lithium-ion migration during cycling, promoting crack formation.

An optimal calcination temperature is one that achieves a balance between improved crystallinity and minimized anisotropy. Materials exhibiting optimal cation mixing are typically produced at temperatures ranging from 750 to 850 °C [142,157,160,161,167,169,170]. This range is considered substantial, as the precise value is contingent upon the targeted stoichiometric configuration. Liang et al. [160] demonstrated that while initial discharge capacities of materials are comparable, those with the highest capacity retention after 40 cycles were produced within this range. Thus, the I(003)/I(104) ratio is a reliable metric for identifying the optimal calcination temperature.

SEM images from Vu and Lee [157] provide further insights. At 780 °C, the cathodic material closely resembles its precursor. At 800 °C, the crystals lose their precursor structure and form aggregates of smaller, non-planar Primary particles. At 850 °C, the crystals reorganize into a parallelepiped shape. Since the lowest cation mixing was observed at 800 °C, this temperature may represent a favorable condition for achieving the desired material structure.

This temperature range should be considered a general guideline rather than a strict rule. For processes involving different chemistries (as discussed in paragraph 8), the optimal calcination temperature may fall outside the 750–850 °C range. In such cases, the best temperature can be identified using SEM images and cation mixing measurements.

6.2. Calcination times

A subsequent discussion addresses the time extension of the calcination treatment. From the statistical analysis of Table S1, an observation of particular interest has been made, though it has not been previously discussed. As illustrated in Fig. 20, a substantial decrease in the I(003)/I(104) ratio is observed with an increase in the calcination time. This observation suggests that there is an increase in the cation mixing with the calcination time.

It is imperative to note that calcination is not merely a process employed in the synthesis of metal oxides and lithiation; it also facilitates the relaxation of the cathode microstructure, thereby eradicating structural defects that have the potential to compromise material performance. Over time, the structure evolves towards a configuration that minimizes the overall energy.

This observation, supported by the statistical analysis in Table S1, suggests that cation mixing may arise from structural relaxation processes, potentially indicating that a more stable configuration corresponds to increased cation mixing (see Fig. 22).

As this hypothesis has not been explicitly addressed in previous literature, further research is required to confirm its validity. If validated, this would highlight the need to optimize calcination time to ensure adequate lithiation while avoiding excessive cation mixing.

6.3. Other key parameters

The thermal treatment is contingent on various parameters, with the temperature being merely one of them. Notwithstanding the dearth of research in this area, a select number of studies have partially examined the subject. The ensuing paragraph will delve into these studies, with the objective of either substantiating existing findings or providing a foundation for future research endeavors.

The two most commonly used lithium sources are LiOH and Li_2CO_3.

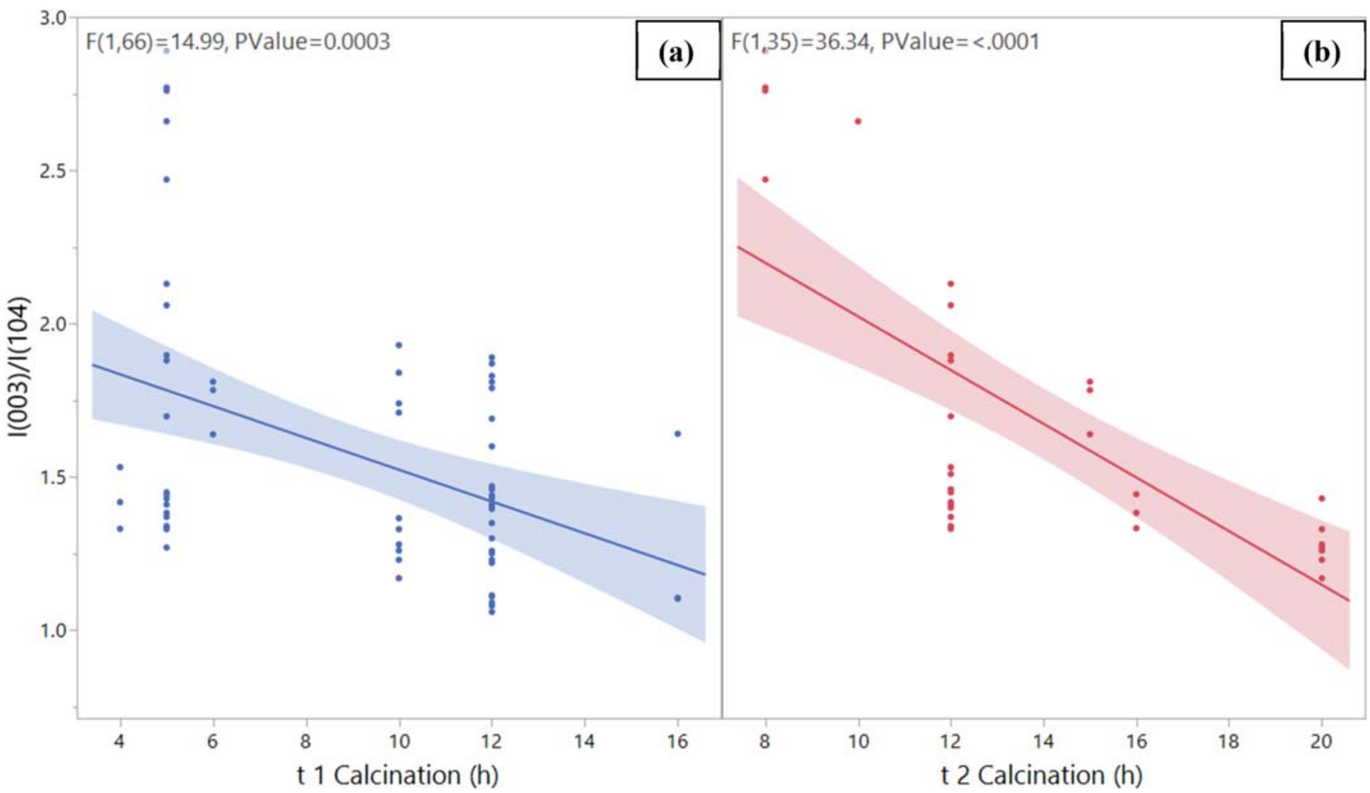

Fig. 22. As illustrated in Table S1, the ratio of the peaks at 003 and 104 can be used to deduce the degree of cation mixing. It is possible to extrapolate a significant dependence of the ratio of the peaks I(003) and I(104), which is indicative of the cation mixing. It has been demonstrated that an increase in the calcination time results in an increase in the cation mixing.

As discussed by Entwistle et al. [171], both are viable but require different operating conditions. LiOH can be utilized at lower temperatures (230–380 °C), while Li_2CO_3 requires temperatures of at least 750 °C. Lithium intercalates in the metal matrix subsequent to the degradation of the lithium source to Li^+ 2 O^{2-} [172]. This process is accompanied by the loss of H_2 O or CO_2, depending on the specific source. In the course of the procedure, lithium evaporates to a certain extent. To rectify this issue, a 10 % excess of lithium is incorporated. It has been demonstrated that an increase in material degradation temperature corresponds to a decrease in the amount of loss [172]. Selecting between LiOH and Li_2CO_3 requires evaluating the trade-off between lithium loss through evaporation and the energy demands of the process. Jo et al. [173] further report that when using Li_2CO_3 with hydroxide precursors, the actual calcination temperature may be lower than the nominal degradation point due to catalytic effects from surface NiOOH.

In many cases, LiOH is the preferred option, as it prioritizes energy consumption over the utilization of lithium in excess.

Fig. 23 is derived from the statistical analysis of Table S1. An analysis of the process reveals no discernible variations when the lithium source is altered during the calcination stage, even when starting from hydroxide precursors. A comparison of the violin plots indicates that the shapes are analogous for both sets of reagents. However, materials synthesized with Li_2CO_3 exhibit slightly greater performance variability.

Based on Fig. 23, the best-performing materials appear to be those derived from carbonate precursors using Li_2CO_3 as the lithium source.

A plethora of studies have been conducted on alternative lithium sources [172,174]; however, none of these investigations have addressed the subject of hydroxide precursors. Nonetheless, an alternative method known as wet impregnation has been proposed, which is not feasible with LiOH or Li_2CO_3 due to their low solubility in water [174]. This procedure is referred to as wet impregnation. This process involves mixing the precursor with an aqueous lithium-rich solution, potentially yielding a more homogeneous mixture than dry blending techniques. A significant drawback of this method is the loss of $Ni(OH)_2$ when the precursor is introduced into the aqueous medium [174].

The atmosphere has also been investigated; Yuan et al. [175] compared the performances of the materials obtained calcinating the precursor in air and in pure oxygen. Their findings suggest that calcination in pure oxygen enhances the bonding strength between transition metals and oxygen atoms. This improvement reduces the incorporation of undesired surface impurities like LiOH and Li_2CO_3, leading to better electrochemical properties. Consequently, all materials obtained from the utilization of pure oxygen atmospheres exhibit enhanced electrochemical performance. However, the economic viability of using pure oxygen at scale must be carefully considered, given its higher cost compared to ambient air.

7. Reactors

The precursor is synthesized through a co-precipitation reaction, and the aggregation of primary particles is significantly influenced by the fluid dynamics, which in turn depend on the type of reactor used.

In the following discussion, we will review different types of reactors, focusing on those that have shown the most promising results in previous studies. These reactors are categorized into three main types: stirred tank reactors (STR), flow reactors, and Taylor-Couette reactors.

The discussion will be based on the basic approach to reactor modelling, with all computations grounded in a theoretical perspective, specifically modelling “ideal reactors". More detailed analyses could be performed by considering the practical behavior of these reactors. However, since this approach depends heavily on the specific apparatus used, such a discussion is beyond the scope of this study. Therefore, our focus will remain on “ideal reactors."

7.1. Stirred tank reactor

A stirred tank reactor (STR) is a simple type of reactor that consists of a tank with impellers to mix the reactants, hence the name “stirred tank."

As previously discussed, we will focus on ideal reactors, assuming STRs are perfectly mixed. This assumption means that the concentrations within the vessel are uniform and equal to the concentration in the outlet, if applicable [176,177].

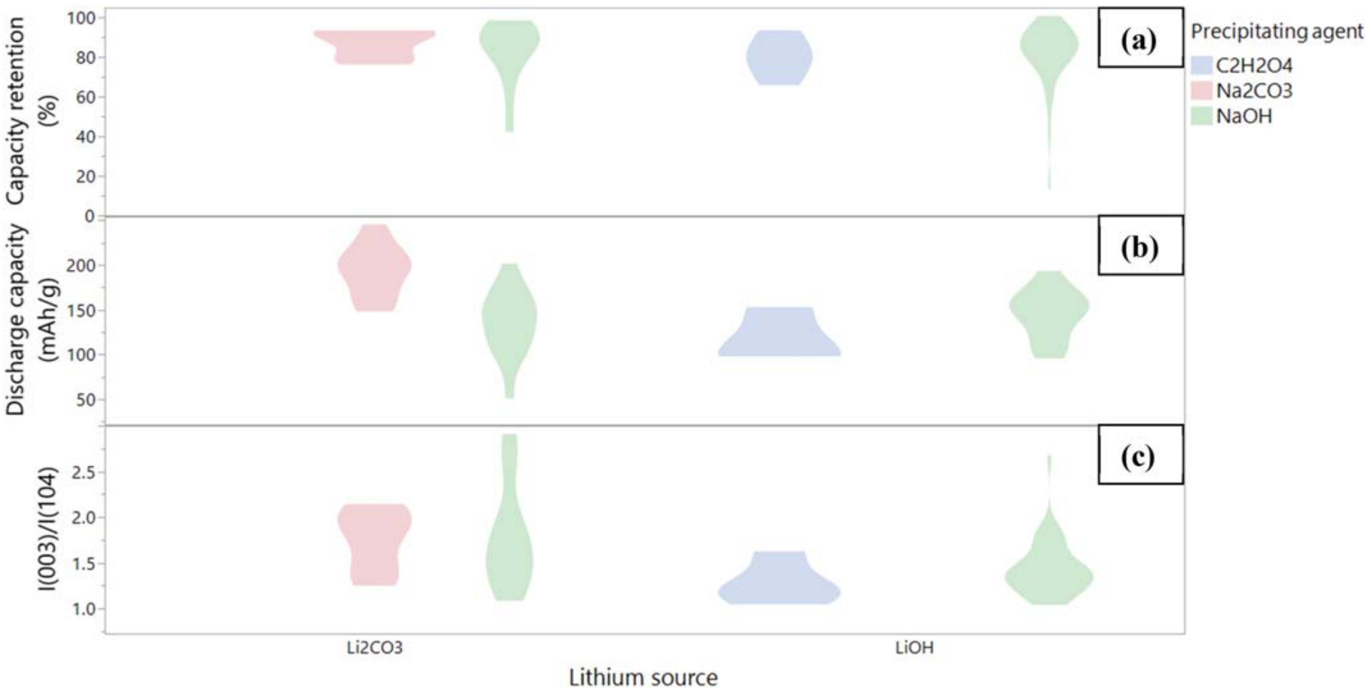

Fig. 23. The figure (a)(b) presents the electrochemical performance of the samples, while (c) illustrates the physical characteristics of the samples obtained from different lithium sources. Attention are directed towards the identification of the precipitating agent utilized, thereby facilitating the determination of the specific precursor.

STRs typically have a cylindrical shape with an aspect ratio (H/D) ranging from 1 to 4, though they can sometimes be larger, up to a maximum of 6.

Temperature control is crucial for ensuring optimal reaction conditions. STRs are equipped with heating or cooling systems, depending on whether the reactions are endothermic or exothermic. Common heat exchange equipment includes jackets, external pipes, and internal coils [176,177].

Reactor sizing is based on mass balances and they require the kinetics of reaction. Some small insights will be presented in the dedicated section for each reactor. More in dept information can be taken from basic books on chemical reactors [176,177].

7.1.1. Batch and semi-batch reactors

Batch reactors are a fundamental type of reactor, consisting simply of a tank, impellers, and a temperature control system. They operate through a straightforward procedure: loading the reactor with reactants, allowing it to operate for a fixed period, and then collecting the products.

In batch reactors, the dynamics are characterized by a single transient phase since the reactor never reaches a steady state. This simplicity makes batch reactors a common choice for synthesizing NMC precursors. Their lack of inlets and outlets minimizes the need for complex controls. However, this same characteristic can be a limitation for large-scale production. Consequently, some studies have explored continuous processes to improve efficiency [135,157,159–161,178], which will be discussed further in the section on Continuous Stirred-Tank Reactors (CSTRs).

In a transient reactor, the operating time required to achieve the desired conversion must be determined using mass balances. Equations S.1–S.6 in the supplementary data demonstrate the computations necessary for reactor dimensioning. Finalizing these computations is not possible without understanding the kinetics. However, detailed kinetic data for NMC precursor co-precipitation is not currently available. Thus, existing studies rely on operational conditions derived from prior experience, with no rigorous kinetic evaluations. Future studies on reaction kinetics would be crucial for scaling up reactors and deriving quantitative values for nucleation and aggregation phenomena.

The balance indicates the temporal dependence of conversion. This correlation enables the derivation of the time required from the reaction to reach the desired conversion.

The residence time, defined as the time during which reagents stay inside the reactor, starts with the apparatus start-up and ends with the shut-down. It coincides with the operative time, which describes the quantity interval in which the reactor is active.

As will be presented later, it is not so simple for other kind of reactors.

In the context of synthesizing NMC precursors, while the reactor might initially be categorized as a batch reactor, it often operates as a semi-batch reactor. This type of reactor allows for the continuous addition or removal of materials during the operation. Unlike batch reactors, which only operate in a single transient phase, semi-batch reactors experience multiple transient phases depending on the operation.

For the synthesis discussed, the semi-batch reactor operates in two phases:

1) Initial Phase: Sodium hydroxide (NaOH) is continuously fed to maintain the desired pH.
2) Secondary Phase: After reaching the desired pH, the reactor functions similarly to a batch reactor with no further inlets or outlets.

This division in several steps extends also to the characteristic times. As previously discussed, each phase can be considered a single operation. It is possible to identify a unique operative time, but the residence times can vary between the reagents in dependence on the procedure.

For example, in the NMC co-precipitation, the operative time starts in the instant in which the reagents come in contact for the first time, but the residence time is not uniquely defined. Sodium hydroxide e.g. is injected in the following hours, up to reach the desired pH; therefore, its residence time will be smaller than the operative one.

In summary, semi-batch reactors offer the flexibility of continuous material input while maintaining transient conditions, making them suitable for processes requiring precise control over reactant concentrations and pH [132,140,142,144].

7.1.2. Continuous stirred tank reactor (CSTR)

Continuous Stirred-Tank Reactors (CSTRs) are among the most widely used reactors in industrial applications. They blend the simplicity of batch systems with the high productivity of continuous processes. This combination is the reason why CSTRs are preferred in industry.

However, the presence of multiple inlets and outlets requires additional control systems. These systems adjust input parameters to maintain desired product characteristics and manage disturbances. For instance, CSTRs operate in a steady state, meaning they require precise control of conditions such as flow rates, temperature, and pH. When external disturbances cause deviations from the desired conditions, the control system detects these changes and adjusts manipulated variables to restore optimal operation. Additionally, control systems are essential for managing the start-up and shut-down phases of the reactor.

Despite their advantages, managing CSTRs is more complex than managing batch reactors due to the need for advanced control systems. As a result, there are currently no industrial processes for NMC precursor production using continuous reactors [79,157,159–161,178]. Many studies on continuous production simply use a CSTR to feed a stirred tank reactor, without implementing a real continuous process with active control.

CSTRs operate in three main phases: start-up, steady-state, and shut-down. The steady-state phase is the primary focus for dimensioning and mass balances. During this phase, the reactor operates under stationary conditions, while the start-up and shutdown are transient phases and are not typically considered in the production chain.

In batch reactors, the operative time is straightforward: it is the time the reactor is active, from loading reactants to collecting products. This time is also known as the residence time, which is the duration that reactants and products stay in the reactor.

In CSTRs, the situation is more complex. The operative time refers to the duration from start-up to shut-down. In contrast, the residence time is the average time a volume element spends in the reactor, calculated as the ratio of the reactor volume to the total flow rate Q (i.e., V/Q). However, this calculation may not always be precise.

To illustrate, consider a CSTR where a tracer is injected to study residence time. The concentration of the tracer is given by:

$$c_0 = \frac{M_0}{V} \tag{12}$$

The mass balance for the tracer is:

$$V\frac{dc}{dt} = -Qc \tag{13}$$

The concentration profile of the tracer is:

$$c(t) = c_0 e^{-\frac{Q}{V}t} \tag{14}$$

The mass of tracer leaving the reactor between time and is:

$$M(t) = \int_{t_1}^{t} Qc\, d\tau = Qc_0 \int_{t_1} te^{-\frac{Q}{V}\tau}\, d\tau \tag{15}$$

Dividing by M_0:

$$\frac{M(t)}{M_0} = \int_{t_1} t\frac{Q}{V}e^{-\frac{Q}{V}\tau}\, d\tau \tag{16}$$

This result shows that the residence time distribution is not a single value but an exponential decay function, indicating a range of residence times for different particles.

Despite that, in CSTRs residence times can be satisfyingly approximated with the ratio V/Q.

The most important point of this discussion is that speaking about CSTRs, in previous studies there is a lot of confusion and little clarity on the way CSTRs are operated. Many times there is no way to identify the residence time because it is not declared and there are missing parameters to compute it [69,134,139,179–183].

Another discussion on the times declared in previous studies deals with the working procedure of CSTRs.

The reactor is initially loaded with water (or with metal solution, although this causes the waste of materials), then the reagents feed and the outlet are activated. At this point the reactor is not at its final steady-state, because there is a transient period required before reaching the steady state [176,177].

Another error done in previous studies is to collect the material at several times from the beginning and to analyze the particles to identify the kinetic of nucleation and growth [138]. This is not an accurate procedure because the particles taken into account are produced during the transient, therefore their characteristics are affected from parameters that are still far from the steady state, and this may compromise the crystallization. For example, at the beginning the reagents are injected in a volume full of water, therefore they are diluted and them concentration is different from the one that will be reached at the steady state.

A significant drawback of CSTRs is that good conversion typically results in low reactant concentrations at the outlet, which can slow down reaction rates since many reactions are enhanced by higher reactant concentrations. To achieve high conversion rates, CSTRs often need to be larger to extend residence time, creating a trade-off between conversion efficiency and reactor size. This trade-off is influenced by the economic considerations of the process, and commonly, CSTRs are designed for a conversion rate around 60 %, which is relatively modest.

7.1.3. STRs with high shear mixers

High shear mixers are not strictly reactors but are crucial components in many chemical and industrial processes, including those involving the synthesis of NMC (Nickel Manganese Cobalt) precursors. These devices are designed to enhance mixing efficiency through intense shear forces, which can be critical for controlling particle formation and growth.

A high shear mixer consists of two main components:

1) Rotor: The rotor is a dynamic component featuring multiple blades arranged along concentric circles. It operates at extremely high speeds, typically ranging from 10,000 to 20,000 revolutions per minute (rpm). The high rotational speed of the rotor generates significant shear forces, which improve the mixing process.
2) Stator: The stator is a static component that surrounds the rotor and is composed of one or more concentric chambers. The stator is equipped with several holes of varying geometries, creating a maze-like structure that facilitates enhanced mixing by directing the flow of the fluid through intricate pathways.

High shear mixers are primarily used to achieve superior mixing by generating high shear stresses. These stresses are essential for processes where rapid and uniform mixing is required, such as in the synthesis of NMC precursors. The primary advantages of high shear mixers include:

- Enhanced Mixing: The intense shear forces created by the rotor and stator improve the uniformity of the mixture, leading to better control over particle size and distribution.
- Improved Particle Formation: The high shear environment accelerates the formation of spherical particles and promotes smoother surfaces. This is particularly beneficial in the synthesis of NMC precursors, where particle morphology is crucial.

High shear mixers can be integrated into stirred tank reactors (STRs), either as standalone units or in combination with other types of mixers (e.g., axial or radial impellers). When used in conjunction with STRs, the balance equations for mass and energy remain the same as those previously discussed for STRs. However, the presence of high shear mixers introduces additional mixing dynamics that can influence the overall process.

Studies have shown that incorporating high shear mixers in the synthesis of NMC precursors offers several benefits:

- Increased Capacity: Research [184–186] indicates that transitioning from conventional impellers (axial or radial) to high shear mixers improves both the initial discharge capacity and the capacity retention of the process.
- Enhanced Shear Stress: High shear mixers are capable of subjecting particles to extremely high rotational velocities. This is in contrast to conventional impellers, which may cause particle breakage at much lower speeds (around 1,200 rpm). The ability of high shear mixers to maintain particle integrity while applying high shear stresses suggests that they are effective at enhancing fluid dynamics without compromising particle structure.

High shear mixers play a critical role in optimizing the synthesis of NMC precursors by improving mixing efficiency and particle formation. Although they are not reactors themselves, their ability to generate high shear forces makes them an invaluable tool for controlling the growth and aggregation of particles. The integration of high shear mixers into STRs or other reactors can lead to significant improvements in product quality and process efficiency.

7.2. Flow reactors

As their name specifies, these reactors involve a continuous flow of reagent solutions. They are typically constructed from pipes and can have aspect ratios that reach up to 20. Since plug flow reactors (PFRs) are the most notable example of such reactors, they will be discussed in the following paragraph, even though they have no applications in the synthesis of NMC precursors. The discussion will then proceed to consider two promising options for the process presented here: micro-reactors and static mixers.

7.2.1. Plug flow reactors (PFR)

They are, along with CSTRs, the most commonly used reactors. Almost all industrial reactions are managed using either a CSTR or a PFR. Plug flow reactors also have a simple configuration. They consist of a pipe through which reactants are fed [176,177]. Under the ideal reactor assumption, a PFR is modelled based on two hypotheses: the entering solution is a perfect mixture of reactants (uniform distribution of concentrations), and all properties are uniformly distributed along the cross-section. Because of this latter characteristic, PFRs are dimensioned and modelled using a unidimensional balance.

Eq. S.13–S.18 illustrate how the balance must be performed for equipment dimensioning. In this context, the result depends on the reaction rate. The mass balance must be coupled with the energy balance, as the kinetic constant is temperature-dependent [165]. This principle applies to any reactor; however, the discussion was previously simplified because, in stirred reactors, the temperature is uniformly distributed, resulting in a uniformly distributed kinetic constant.

However, this is not the case for PFRs, as there is a temperature profile along the x-axis. Achieving a more uniform temperature would necessitate the implementation of a control system capable of maintaining constant conditions along the entire reactor. However, this presents a significant challenge. For instance, the limitation of the peak temperature, which is usually concentrated in the center of the reactor, necessitates intervention at specific locations. This is a particularly complex issue due to the fact that cooling systems, for both practical and economic reasons, generally affect the entire reactor. These systems frequently incorporate jackets or coils. Furthermore, during the initiation and cessation of operation, peak temperatures may be observed at disparate locations, necessitating adjustments at multiple points. A reduction in temperature at one point can have ramifications for the entire reactor, potentially leading to a decrease in reaction rates in regions where conditions were previously optimal.

However, PFRs have been shown to achieve higher conversions than CSTRs. As conversions increase along the reactor's length, the concentration gradients that are characteristic of the CSTR are preserved, thereby avoiding the mixing limitations that are a hallmark of CSTRs.

However, PFRs are subject to back-mixing, a phenomenon where a portion of the reagents moves in the opposite direction of the flow, affecting the concentrations. This issue must be considered, as it leads to a relaxation of the ideal reactor assumptions.

These reactors operate in turbulent regimes, resulting in plug flow. Mixing along the section is achieved through convective motions, which generate shear stresses significantly lower than those in stirred reactors. This reduces transport and aggregation phenomena. However, they are not suitable reactors for NMC precursor production, which explains the lack of previous studies utilizing these units. They were introduced to highlight the pros and cons of PFRs, the class to which the following reactors belong.

7.2.2. Microreactors

They are similar to PFRs, but their cross-sectional diameter is under 1 mm. Despite this similarity, an important distinction sets them apart: PFRs typically operate under turbulent conditions (with a few exceptions), while microreactors are almost every time under in laminar flow. As a result, the assumption of an ideal reactor with a uniform distribution of fluid properties along the cross-section does not hold true for microreactors. In PFRs, the motion along the cross-section is driven by turbulence and convection phenomena. In contrast, in microreactors, species move along the section primarily due to diffusion.

Although the regime in microreactors is laminar, it might seem that the reaction is limited by transport phenomena more than in PFRs. However, this is not the case because the pipe diameter is so small that the available area is extremely reduced. This effect is pronounced enough to enhance transport phenomena. Indeed, microreactors are often used to highlight the kinetics of reactions controlled by transport.

Several studies in the literature have investigated the synthesis of NMC precursors using microreactors [186–188]. Para et al. [186,187] conducted two studies. In the first [186], they used microreactors to carry out the synthesis and develop a model for particle evolution over time. In the second [187], they focused primarily on characterizing the product and evaluating microreactors as production equipment.

Wu et al. [188] also tested microreactors for synthesizing LNMO precursors, opting to precipitate the product as carbonates—a chemistry that will be discussed later. This approach is promising, as particles with optimal morphology and size were produced in just 12 s. SEM micrographs showed that the primary particles had different shapes compared to the usual ones; this capability to achieve optimal morphology quickly can be attributed to their packing method. The properties of these precursors translate into good electrochemical performance.

In conclusion, it is important to note that the term "microreactor" may not be perfectly suited for such applications. With a pipe diameter of 1 mm, they are on the borderline between flow reactors and microreactors. Furthermore, they have been used only for production purposes, with no studies conducted on reaction kinetics. This observation highlights a potential application of microreactors that has not yet been explored but could open avenues for future research.

7.2.3. Static mixers

As with high shear mixers, static mixers were not originally designed as reactors but as equipment for mixing or separating. They are particularly effective for mixing highly viscous materials that can only be moved in laminar flow. In a PFR, if some reactants have high viscosity, the only way to ensure proper mixing in the system is by using such mixing equipment. This is also applicable to fluids with viscosities close to that of water but used in microreactors.

Although static mixers have not been used for the precipitation of NMC precursors, they are worth mentioning because they can enhance production in microreactors. This is related to the behavior of primary particles. In narrow channels, species transport is enhanced, but primary particle motion is restricted. With Poiseuille flow, primary particles move in straight lines along the axial axis of the channel, limiting their ability to aggregate.

This behavior is related to the fluid's regime. In capillary channels, the critical Reynolds number for transitioning from laminar to turbulent flow is 1. Therefore, in microreactors, achieving a turbulent regime is relatively easy. However, for pipes with diameters around 1 mm, this is not the case; they are too large, and the critical Reynolds number remains at 4000. Channels with such small diameters exhibit high pressure drops, making it difficult for pumps to push the fluid quickly, which necessitates operating in a laminar regime. Consequently, the idea of using confined spaces to reduce dependence on transport phenomena may not be effective due to reduced turbulence and mixing.

This is why static mixers are relevant, as they can provide efficient mixing even under laminar flow conditions.

7.3. Taylor-Couette

These reactors consist of two concentric cylinders: an inner, rotating cylinder and an outer, static cylinder. Fluid flows through the gap between the two cylinders. As the inner cylinder rotates, different fluid regimes are observed, which are identified by critical values of the characteristic parameter known as the "cylindrical Reynolds number" or Taylor number:

$$Ta = Re_{cyl} = \frac{\omega r_i d}{\nu} \tag{17}$$

where r_i is the radius of the inner cylinder, ω is the angular velocity, d is the gap between the cylinders, and ν is the fluid viscosity.

In this reactor, four distinct regimes can be identified based on the Taylor number. The transition points between these regimes depend on the specific equipment and the fluid used. The regimes are:

- Laminar Flow: The velocity field appears as concentric cylinders with velocities decreasing progressively from the inner surface to the outer.
- Taylor-Vortex Flow: The fluid is divided into several vortices with parallel horizontal axes along the height of the reactor.
- Wavy Vortex Flow: The fluid is distributed in vortices with wavy rather than strictly horizontal axes.
- Turbulent Flow: The fluid is completely mixed, and no distinct structure is visible.

The regime of interest for this application is Taylor-vortex flow. This regime allows for effective mixing while confining the materials to a small volume, significantly reducing transport limitations. It also facilitates interactions between particles without the excessive impacts or shear stresses found in CSTRs. This is crucial for crystallization reactions, as excessive forces can compromise nucleation, growth, and aggregation.

Indeed, Kim et al. [189] proved that in Taylor-Couette rectors particles sensitivity to fluid shear is lower than in STR.

Moreover, in Taylor-Couette reactors, reagents follow a continuous path from the inlet to the outlet, with no mixing between the inlet and outlet. This enables high conversions, similar to PFRs. In this regard, Taylor-Couette reactors have an advantage over PFRs because the Taylor vortices effectively prevent back-mixing, whereas in plug flow reactors, the lack of back-mixing is merely an assumption. Additionally, Taylor vortices provide mixing that is as effective as that in STRs but without the violent conditions that could damage particle integrity during growth.

As a result, Taylor-Couette reactors combine the benefits of both PFRs and STRs in a single system. Some studies have tested Taylor-Couette reactors for producing NMC precursors [190–196]. The results consistently showed particles with optimal morphology, including shape, size, and sphericity, regardless of the stoichiometry used. This indicates the effectiveness of the Taylor-Couette reactor in producing high-quality cathode precursors. However, no studies have compared the performance of Taylor-Couette reactors with that of classical STRs, so it is unclear how much this method improves particle quality. All these results are achieved with short residence times and continuous processing.

8. Alternative chemistries

As previously discussed, the synthesis of NMC cathode materials can be optimized through the process of hydroxide precipitation, provided that certain operative conditions are met.

When these conditions are combined with the reactor properties previously outlined, several challenges associated with scaling up the process, such as transitioning to continuous production, become evident. These challenges include:

- Inert Atmosphere Control: Maintaining an inert atmosphere in large industrial volumes is challenging. The reactor must be perfectly sealed to prevent contamination from manganese oxide impurities, which can compromise the final material.
- Extended Growth Time: The growth mechanism requires several hours to complete. Given the required production rate and residence times, the volumes involved are substantial. This challenge is compounded when considering the smoothing step, making it appear almost impossible to scale up to an industrial level.
- pH Control: Controlling the pH in large reactors is difficult. The need for a basic solution (typically NaOH) affects the liquid level and concentration in the reactor, necessitating a complex control system.
- NaOH and NH3 Ratio: The ratio between NaOH and NH3 must be precisely controlled.
- Ammonia Toxicity: The use of ammonia poses health risks to operators due to its toxicity.

These issues significantly impact production, requiring considerable effort and imposing severe limitations. This development has given rise to a growing interest in alternative chemistries. Among the most promising proposals are the precipitation of precursors as carbonates or oxalates. These proposals are not novel; they were obscured from the hydroxide precipitation. This phenomenon may appear counterintuitive, given that alternative proposals have been developed and address

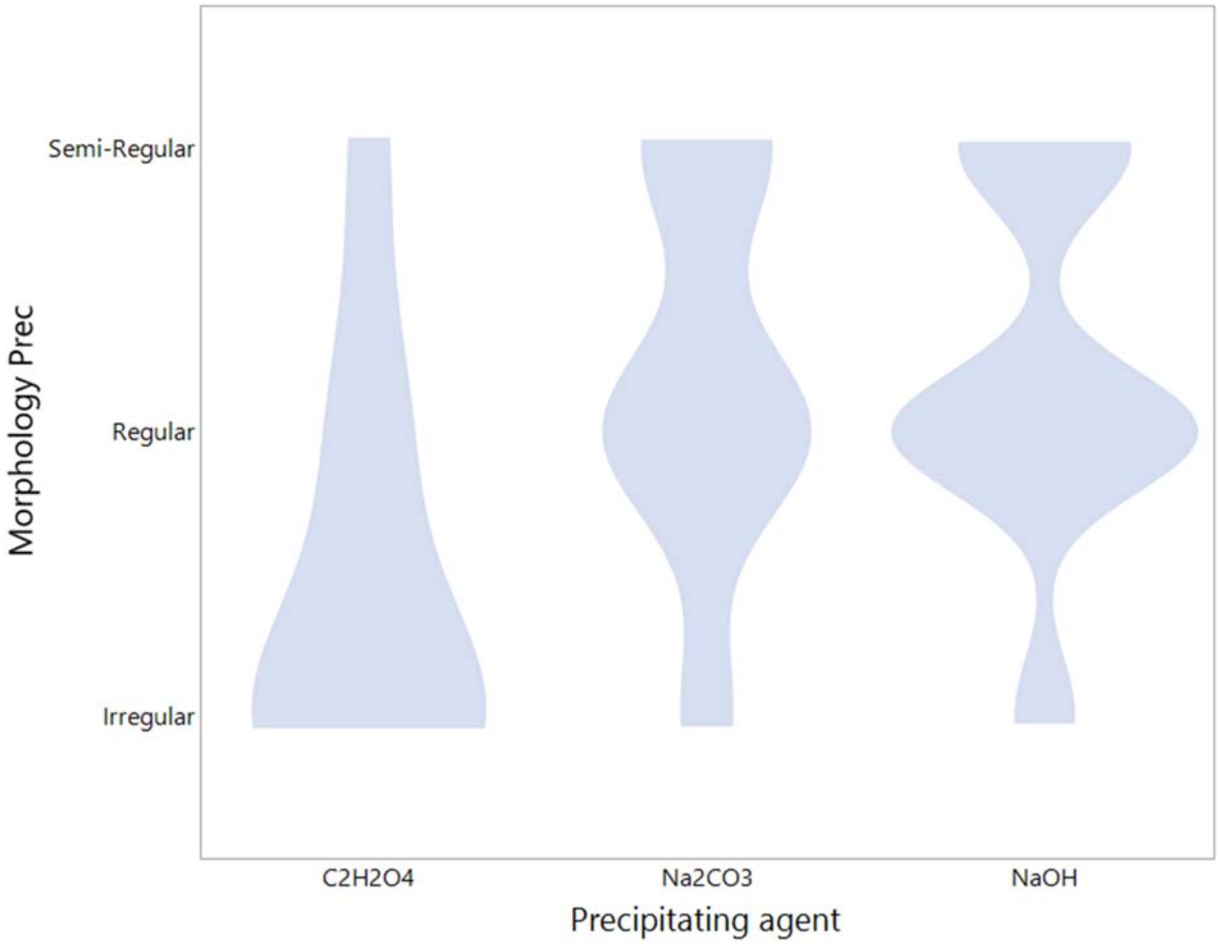

Fig. 24. The violin plots presented herein are derived from Table S1. By defining "regular" as particles that exhibit a homogeneous distribution and spherical shape, it is possible to classify them by naked eye observation as either irregular, semi-regular, or regular. The plot demonstrates a higher probability of regular particles precipitating precursors as hydroxides compared to oxalates or carbonates.

the previously identified criticisms.

The underlying reason for this phenomenon pertains to the elasticity of the hydroxide precipitation process. This process has the capacity to yield particles with optimal morphology, despite the considerable variations in the surrounding conditions. This phenomenon can be attributed to the effect of smoothing phenomena experienced with extended operative time. As illustrated in Fig. 24, the employment of NaOH as a precipitating agent leads to the formation of regular particles with a higher frequency compared to the utilization of alternative precipitating agents.

The employment of disparate precipitating agents has been demonstrated to alleviate certain constraints associated with hydroxide ions; however, further exploration is imperative to enhance the comprehension of nucleation and growth phenomena in the context of material production, particularly concerning the morphology of the resultant material. This has historically posed a significant impediment from an industrial perspective. However, recent advancements in the field of precipitation reaction offer a potential avenue for overcoming these limitations [197–199].

The following paragraph will provide a detailed discussion of these two alternatives to the hydroxide co-precipitation process.

8.1. Oxalates

In this process, NMC precursors are precipitated as a matrix of mixed metal oxalates. Co-precipitation is achieved by inducing the reaction between two solutions: one containing metals and the other containing oxalic acid [200–206].

Initially, the focus will be on the optimal operating conditions for synthesis to provide a basis for comparison. The discussion will then shift to the specific features of this method. Although this process is an alternative to the more commonly used hydroxide co-precipitation, there is limited research available.

Firstly, regarding chelators, there is no need to use a chelating agent for oxalate precipitation. Metal oxalates naturally precipitate in a uniform matrix, making a chelator unnecessary. Yao et al. [204] provided evidence for this by performing TG and DSC analyses on the oxalate precursor, revealing a single rapid weight loss and an endothermic peak, indicating a single crystalline structure.

The impact of pH is different in this process. pH does not affect the quantity of reactant in solution but primarily influences the solubility of metal oxalates. Park et al. [202] conducted a study varying pH (from −0.5 to 4.5) and observed how metal oxalate solubility was affected. They used visual observations of solution color and precipitate quantity as reference points. The results showed that lower pH levels reduced the solubility of manganese oxalate, leading to less manganese in the final material. To address this, they used salts of weak bases, like ammonium salts, which was a good approach for their study but might not be suitable here as it could reduce process independence from ammonia.

When comparing to hydroxide precipitation, studies [135,144,146,185] indicate that manganese quantity in hydroxide co-precipitation can sometimes be lower than stoichiometric amounts. Despite this, the electrochemical performance was not adversely affected. Hua et al. [185] reported the best electrochemical results from samples with lower manganese content. This is because manganese provides chemical and thermal stability but does not contribute significantly to electrochemical performance. Additionally, controlling pH in hydroxide precipitation often requires an OH- source, which can lead to unwanted hydroxide phase formation around particles. Therefore, oxalate co-precipitation, which does not require pH control, can be a simpler alternative.

Regarding reaction temperature, there is limited data on its influence, but it is typically set within the range of 60–80 °C [205–208]. This condition is similar to hydroxide co-precipitation. Further research is needed to determine the optimal synthesis temperature, as oxalates do not undergo parasitic reactions above 60 °C [205,208].

Agitation has not been extensively studied for oxalate co-precipitation. Typically, agitation is maintained between 300 and 500 rpm [201,206,207], but there is insufficient data to draw conclusions.

Regarding operational times, Dong et al. [207] provided some insights. They investigated the nucleation and growth rates of Mn oxalates, Ni oxalates, and Ni-Mn mixed oxalates. They found that Mn oxalates precipitate much faster than Ni oxalates, resulting in larger particles. Mixed metal precipitates follow a nucleation and growth pattern similar to single Mn oxalates, with the initial Mn seeds facilitating Ni precipitation. However, this study focused only on Ni and Mn, and the presence of Co might influence the results, as cobalt oxalates are known to precipitate more easily [202].

Calcination temperature is the only parameter with dedicated studies [200,204]. Yao et al. [204] determined that the optimal calcination temperature for NMC is 850 °C. They found that 800 °C was too low for complete reaction between lithium hydroxide and the precursor, while 900 °C was too high and caused decomposition. Thus, 850 °C strikes a balance between these effects.

Overall, oxalate synthesis appears to be simpler than hydroxide precipitation. While hydroxides benefit from slower reaction rates that result in smooth surfaces, oxalate co-precipitation is faster and requires less control. Therefore, oxalate co-precipitation seems more promising for scalable processes.

To definitively confirm this, future studies should compare the electrochemical performance of NMCs produced by both methods. This comparison will provide crucial insights into the advantages of each production procedure.

8.2. Carbonates

This method is another promising alternative to metal hydroxide co-precipitation. Its distinctive feature is its ability to produce spherical particles with smooth surfaces within a few hours [138,209–211]. However, as with the previous method, there is limited research on this process, making it challenging to determine the optimal conditions for maximizing electrochemical performance. The following discussion summarizes the current knowledge on the topic.

The primary study addressing this field is by Ngoepe et al. [209], which explored various operating conditions. They found that a pH of 8.3 was optimal, as it maximized the tap density without causing significant agglomeration. Temperature was also a critical factor; their tests showed that 55 °C was the best choice among the temperatures tested (35, 45, and 55 °C). This temperature significantly increased particle size and tap density by enhancing the reaction rate. They evaluated several stirring rates (600, 800, 1000, 1200, and 1400 rpm) and found that lower stirring rates did not provide enough shear stress to prevent exfoliation, while very high stirring rates led to excessive agglomeration. The optimal stirring rate was identified as 1200 rpm. These observations suggest that carbonates are more resistant to impacts and shear stresses compared to hydroxides. Lastly, they determined that satisfying particle size and tap density (around 24 μm and 1.4 g/cm^3) were achieved only after 48 h, making this process significantly slower than hydroxide co-precipitation.

Pimenta et al. [138] reported producing spherical particles with smooth surfaces and dimensions of 5 μm within just 2 h. Moreover, aging the product for an additional 12 h did not result in significant changes.

The discrepancy between these results is not easily explained. Both studies used ammonia as a chelating agent, which can significantly influence synthesis time, but this does not fully account for the differences in results. Wu et al. [188] provide an interesting perspective; they used a microreactor for LMN precursor synthesis through carbonate co-precipitation and achieved particle formation in just 12 s without a chelating agent. Notably, they also tested the material and found its electrochemical performance to be comparable to that of materials typically reported in the literature [138,209–211].

Regarding calcination temperature, Cho et al. [199] found that 850 °C was optimal based on electrochemical performance.

It is important to note that these parameters exhibit synergistic behavior and are not fixed but rather case-dependent. However, they can serve as starting points for trials, as the optimal values are unlikely to be far from those proposed.

In conclusion, carbonates present a valuable alternative to hydroxide co-precipitation. Their advantage of not requiring an inert atmosphere is significant, and the results from existing studies are promising [138,188,209–211]. Further research is needed to clarify the role of chelating agents and to resolve the inconsistencies regarding synthesis time.

9. Conclusions

Metal co-precipitation is a process involving nucleation and growth, wherein primary particles are formed and subsequently aggregate and grow through Ostwald ripening. This process is influenced by both chemical and fluid-dynamic factors. The characteristics of the resulting product are determined by the interplay of chemical parameters within the reactor, where the balance of chemical and physical parameters is crucial.

The influence of the chelating agent on particle formation is intricate, involving competition with hydroxide ions, impacting nucleation, and requiring careful balance of the NH3/OH-ratio for optimal outcomes. The pH has a substantial impact on metal hydroxide synthesis, affecting reaction speed, particle morphology, and uniformity. Elevated pH levels have been observed to result in excessive nucleation, while low pH levels have been shown to lead to the formation of large, loosely packed crystals. The optimal pH range, defined as 10–12, is contingent upon the prevailing conditions and must be meticulously maintained to ensure the desired quality of the product. Temperature exerts a profound influence on the feasibility of reactions, impurity formation, and the rate of reactions. At temperatures in excess of 60 °C, manganese hydroxide undergoes oxidation. Conversely, elevated temperatures result in non-uniform particles and undersized primary particles at low temperatures. The optimal range for this process, identified as 50–55 °C, is conducive to the formation of homogeneous, spherical particles.

The synthesis of NMC precursors is influenced by physical parameters in two distinct ways: during the synthesis process (agitation and operative time) and in the post-synthesis phase (calcination temperature). It has been demonstrated that elevated agitation levels, surpassing 1200 rpm, result in a smoothing of the particles; nevertheless, excessive stirring has the potential to lead to particle breakage. The reaction time has been shown to influence the growth of particles, with optimal smoothing occurring within the range of 15–30 h. Calcination, conducted in two stages, maximizes crystallinity within the range of 750–850 °C. However, the application of excessive heat (greater than 900 °C) or extended duration has been observed to enhance cation mixing. The judicious regulation of these parameters is instrumental in ensuring the superior quality of battery materials.

A variety of reactors are employed for the synthesis of NMC precursors, including stirred tank reactors (STRs), continuous stirred tank reactors (CSTRs), and STRs equipped with high shear mixers. While STRs, in both batch and semi-batch configurations, ensure uniform mixing, they are limited in their application for large-scale production. Conversely, CSTRs have been found to be highly effective for continuous processes; however, they necessitate sophisticated control systems and are typically of a larger size to achieve high conversion rates. The integration of high shear mixers into STRs has been shown to enhance particle formation, thereby improving process efficiency. The selection of a particular reactor depends on the desired reaction dynamics and particle control for NMC precursor synthesis. Flow reactors, comprising Plug Flow Reactors (PFRs), microreactors, and static mixers, find application in continuous reagent flow. PFRs have been shown to be efficient; however, they are not well-suited for NMC precursor synthesis due to the challenges associated with temperature control and back-mixing. Microreactors, with diameters under 1 mm, have been shown to enhance transport phenomena and have demonstrated potential in synthesizing NMC precursors with optimal particle morphology. However, further study is necessary to elucidate their reaction kinetics. Static mixers have been demonstrated to enhance mixing in laminar flow conditions, thereby facilitating particle formation. Taylor-Couette reactors, with their distinctive Taylor-vortex flow, provide effective mixing and high-quality particle production, combining the advantages of PFRs and STRs. Alternative chemistries for NMC cathode precursor synthesis, such as oxalates and carbonates, offer potential solutions to the limitations of hydroxide co-precipitation. Oxalate precipitation, a process that does not necessitate the use of chelators and exhibits less pH control, offers a more streamlined process. It has been observed to facilitate expedited nucleation and growth; however, it necessitates meticulous calcination procedures. The process of carbonate precipitation has been shown to yield spherical particles with smooth surfaces in a relatively short period of time, provided that the pH is maintained within the optimal range of 8.3, the temperature is set at 55 °C, and the stirring rate is set at 1200 rpm. In comparison to hydroxide precipitation, both methods exhibit enhanced scalability; however, further research is necessary to ascertain their electrochemical performance and identify the optimal conditions for each.

CRediT authorship contribution statement

Marco Colasanti: Writing – original draft, Investigation, Data curation, Conceptualization. **Cristina Gatti:** Writing – original draft. **Maryam Maryam:** Writing – original draft. **Chiara Ferrara:** Writing – review & editing, Writing – original draft, Investigation, Conceptualization. **Micol Di Veroli:** Data curation. **Massimiliano Giona:** Writing – review & editing. **Pier Giorgio Schiavi:** Writing – review & editing. **Pietro Altimari:** Writing – review & editing. **Francesca Pagnanelli:** Writing – review & editing, Project administration, Funding acquisition, Data curation, Conceptualization.

Declaration of competing interest

The authors declare that they have no known competing financial interests or personal relationships that could have appeared to influence the work reported in this paper.

Acknowledgements

This work was carried out within the MOST – Sustainable Mobility Center and received funding from the European Union Next-Generation EU (PIANO NAZIONALE DI RIPRESA E RESILIENZA (PNRR) – MISSIONE 4 COMPONENTE 2, INVESTIMENTO 1.4 – D.D. 1033 June 17, 2022, CN00000023). This manuscript reflects only the authors' views and opinions, neither the European Union nor the European Commission can be considered responsible for them.

This article benefited from language and grammar suggestions provided by ChatGPT and DeepL.

Appendix A. Supplementary data

Supplementary data to this article can be found online at https://doi.org/10.1016/j.jpowsour.2025.238132.

Data availability

Datas available as supplementary materials.

References

[1] B. Diouf, R. Pode, Potential of lithium-ion batteries in renewable energy, Renew. Energy 76 (2015) 375–380, https://doi.org/10.1016/j.renene.2014.11.058.

[2] Z. Wu, C. Zhang, F. Yuan, M. Lyu, P. Yang, L. Zhang, M. Zhou, L. Wang, S. Zhang, L. Wang, Ni-rich Cathode Materials for Stable high-energy lithium-ion Batteries, 2024.

[3] S. Patnaik, Overview of electrode advances in commercial Li-ion batteries, Ionics 30 (2024) 3069–3090, https://doi.org/10.1007/s11581-024-05579-1.

[4] F. Cerdas, P. Titscher, N. Bognar, R. Schmuch, M. Winter, A. Kwade, C. Herrmann, Exploring the effect of increased energy density on the environmental impacts of traction batteries: a comparison of energy optimized lithium-ion and lithium-sulfur batteries for mobility applications, Energies 11 (2018) 150, https://doi.org/10.3390/en11010150.

[5] M. Akhilash, P.S. Salini, B. John, T.D. Mercy, A journey through layered cathode materials for lithium ion cells – from lithium cobalt oxide to lithium-rich transition metal oxides, J. Alloys Compd. 869 (2021) 159239, https://doi.org/10.1016/j.jallcom.2021.159239.

[6] J.L. Pimlott, R.J. Street, M.P. Down, C.E. Banks, Electrochemical Overview: a Summary of ACoxMnyNizO2 and Metal Oxides as Versatile Cathode Materials for Metal-Ion Batteries, 2021.

[7] K. Mizushima, P.C. Jones, P.J. Wiseman, J.B. Goodenough, LixCoO2 (0<x<-1): a new cathode material for batteries of high energy density, Mater. Res. Bull. 15 (1980) 783–789, https://doi.org/10.1016/0025-5408(80)90012-4.

[8] J.B. Goodenough, K.-S. Park, The Li-Ion rechargeable battery: a perspective, J. Am. Chem. Soc. 135 (2013) 1167–1176, https://doi.org/10.1021/ja3091438.

[9] M.M. Thackeray, W.I.F. David, P.G. Bruce, J.B. Goodenough, Lithium insertion into manganese spinels, Mater. Res. Bull. 18 (1983) 461–472, https://doi.org/10.1016/0025-5408(83)90138-1.

[10] C. Schilcher, C. Meyer, A. Kwade, Structural and electrochemical properties of calendered lithium manganese oxide cathodes, Energy Technol. 4 (2016) 1604–1610, https://doi.org/10.1002/ente.201600130.

[11] A.K. Padhi, K.S. Nanjundaswamy, J.B. Goodenough, Phospho-olivines as positive-electrode materials for rechargeable lithium batteries, J. Electrochem. Soc. 144 (1997) 1188–1194, https://doi.org/10.1149/1.1837571.

[12] J. Hu, W. Huang, L. Yang, F. Pan, Structure and performance of the $LiFePO_4$ cathode material: from the bulk to the surface, Nanoscale 12 (2020) 15036–15044, https://doi.org/10.1039/D0NR03776A.

[13] H.-H. Ryu, B. Namkoong, J.-H. Kim, I. Belharouak, C.S. Yoon, Y.-K. Sun, Capacity fading mechanisms in Ni-Rich single-crystal NCM cathodes, ACS Energy Lett. 6 (2021) 2726–2734, https://doi.org/10.1021/acsenergylett.1c01089.

[14] Benchmark Mineral Intelligence, Benchmark mineral intelligence. https://www.benchmarkminerals.com/.

[15] M. Baazizi, M. Karbak, M. Aqil, S. Sayah, M. Dahbi, F. Ghamouss, High-valence surface-modified LMO cathode materials for lithium-ion batteries: diffusion kinetics and operando thermal stability investigation, ACS Appl. Mater. Interfaces 15 (2023) 40385–40396, https://doi.org/10.1021/acsami.3c05708.

[16] M. Malik, K.H. Chan, G. Azimi, Review on the synthesis of LiNixMnyCo1-x-yO2 (NMC) cathodes for lithium-ion batteries, Mater. Today Energy 28 (2022) 101066, https://doi.org/10.1016/j.mtener.2022.101066.

[17] S.S. Nisa, M. Rahmawati, C.S. Yudha, H. Nilasary, H. Nursukatmo, H. S. Oktaviano, S.U. Muzayanha, A. Purwanto, A fast approach to obtain layered transition-metal cathode material for rechargeable batteries, Batteries 8 (2022) 4, https://doi.org/10.3390/batteries8010004.

[18] S. Mallick, A. Patel, X.-G. Sun, M.P. Paranthaman, M. Mou, J.H. Mugumya, M. Jiang, M.L. Rasche, H. Lopez, R.B. Gupta, Low-cobalt active cathode materials for high-performance lithium-ion batteries: synthesis and performance enhancement methods, J Mater Chem A Mater 11 (2023) 3789–3821, https://doi.org/10.1039/D2TA08251A.

[19] S. Yamada, M. Fujiwara, M. Kanda, Synthesis and properties of LiNiO2 as cathode material for secondary batteries, J. Power Sources 54 (1995) 209–213, https://doi.org/10.1016/0378-7753(94)02068-E.

[20] Z. Liu, A. Yu, J.Y. Lee, Synthesis and characterization of LiNi1−x−yCoxMnyO2 as the cathode materials of secondary lithium batteries, J. Power Sources 81–82 (1999) 416–419, https://doi.org/10.1016/S0378-7753(99)00221-9.

[21] M.-H. Kim, H.-S. Shin, D. Shin, Y.-K. Sun, Synthesis and electrochemical properties of Li[Ni0.8Co0.1Mn0.1]O2 and Li[Ni0.8Co0.2]O2 via co-precipitation, J. Power Sources 159 (2006) 1328–1333, https://doi.org/10.1016/j.jpowsour.2005.11.083.

[22] J. Zhu, G. Chen, Single-crystal based studies for correlating the properties and high-voltage performance of $Li[Ni_x Mn_y Co_{1-x-y}]O_2$ cathodes, J Mater Chem A Mater 7 (2019) 5463–5474, https://doi.org/10.1039/C8TA10329A.

[23] G. Qian, Y. Zhang, L. Li, R. Zhang, J. Xu, Z. Cheng, S. Xie, H. Wang, Q. Rao, Y. He, Y. Shen, L. Chen, M. Tang, Z.-F. Ma, Single-crystal nickel-rich layered-oxide battery cathode materials: synthesis, electrochemistry, and intra-granular fracture, Energy Storage Mater. 27 (2020) 140–149, https://doi.org/10.1016/j.ensm.2020.01.027.

[24] T. Li, X.Z. Yuan, L. Zhang, D. Song, K. Shi, C. Bock, Degradation Mechanisms and Mitigation Strategies of Nickel-Rich NMC-based Lithium-Ion Batteries, 2020.

[25] Z. Zhao, B. Huang, M. Wang, X. Yang, Y. Gu, Facile synthesis of fluorine doped single crystal Ni-rich cathode material for lithium-ion batteries, Solid State Ionics 342 (2019), https://doi.org/10.1016/j.ssi.2019.115065.

[26] M.S. Whittingham, Lithium batteries and cathode materials, Chem. Rev. 104 (2004) 4271–4301, https://doi.org/10.1021/cr020731c.

[27] S. Zhang, J. Ma, Z. Hu, G. Cui, L. Chen, Identifying and Addressing Critical Challenges of High-Voltage Layered Ternary Oxide Cathode Materials, 2019.

[28] Liu, Z., Yu, A., Lee, J.Y.: Synthesis and Characterization of LiNi Co Mn O as the Cathode 1yxyy X Y 2 Materials of Secondary Lithium Batteries.

[29] J. Cho, T.-J. Kim, J. Kim, M. Noh, B. Park, Synthesis, thermal, and electrochemical properties of AlPO[sub 4]-Coated LiNi[sub 0.8]Co[sub 0.1]Mn [sub 0.1]O[sub 2] cathode materials for a Li-Ion cell, J. Electrochem. Soc. 151 (2004) A1899, https://doi.org/10.1149/1.1802411.

[30] W. Li, X. Liu, H. Celio, P. Smith, A. Dolocan, M. Chi, A. Manthiram, Mn versus Al in layered oxide cathodes in lithium-ion batteries: a comprehensive evaluation on long-term cyclability, Adv. Energy Mater. 8 (2018), https://doi.org/10.1002/aenm.201703154.

[31] M. Jeong, H. Kim, W. Lee, S.J. Ahn, E. Lee, W.S. Yoon, Stabilizing effects of Al-doping on Ni-rich LiNi0.80Co0.15Mn0.05O2 cathode for li rechargeable batteries, J. Power Sources 474 (2020), https://doi.org/10.1016/j.jpowsour.2020.228592.

[32] Y.-K. Sun, H.-B. Kang, S.-T. Myung, J. Prakash, Effect of manganese content on the electrochemical and thermal stabilities of li[Ni[sub 0.58]Co[sub 0.28−x]Mn [sub 0.14+x]]O[sub 2] cathode materials for lithium-ion batteries, J. Electrochem. Soc. 157 (2010) A1335, https://doi.org/10.1149/1.3497304.

[33] Fang, R., Miao, C., Nie, Y., Wang, D., Xiao, W., Xu, M., Wang, C.: Degradation mechanism and performance enhancement strategies of LiNi x Co y Al 1−x−y O 2 (X ≥ 0.8) cathodes for rechargeable lithium-ion batteries: a review. https://doi.org/10.1007/s11581-020-03569-7/Published.

[34] S. Lee, A. Manthiram, Can cobalt be eliminated from lithium-ion batteries? ACS Energy Lett. 7 (2022) 3058–3063, https://doi.org/10.1021/acsenergylett.2c01553.

[35] N. Muralidharan, E.C. Self, J. Nanda, I. Belharouak, Next-generation cobalt-free cathodes – a prospective solution to the battery industry's cobalt problem, in: Transition Metal Oxides for Electrochemical Energy Storage, Wiley, 2022, pp. 33–53.

[36] T. Liu, L. Yu, J. Liu, J. Lu, X. Bi, A. Dai, M. Li, M. Li, Z. Hu, L. Ma, D. Luo, J. Zheng, T. Wu, Y. Ren, J. Wen, F. Pan, K. Amine, Understanding Co roles towards developing Co-free Ni-rich cathodes for rechargeable batteries, Nat. Energy 6 (2021) 277–286, https://doi.org/10.1038/s41560-021-00776-y.

[37] Y. You, J. Lu, Timely or early? Breaking away from cobalt-reliant lithium-ion batteries, Next Mater. 1 (2023) 100004, https://doi.org/10.1016/j.nxmate.2023.100004.

[38] W. Huang, C. Lin, M. Zhang, S. Li, Z. Chen, W. Zhao, C. Zhu, Q. Zhao, H. Chen, F. Pan, Revealing roles of Co and Ni in mn-rich layered cathodes, Adv. Energy Mater. 11 (2021), https://doi.org/10.1002/aenm.202102646.

[39] C. Tian, F. Lin, M.M. Doeff, Electrochemical characteristics of layered transition metal oxide cathode materials for lithium ion batteries: surface, bulk behavior, and thermal properties, Acc. Chem. Res. 51 (2018) 89–96, https://doi.org/10.1021/acs.accounts.7b00520.

[40] J. Li, A.R. Cameron, H. Li, S. Glazier, D. Xiong, M. Chatzidakis, J. Allen, G. A. Botton, J.R. Dahn, Comparison of single crystal and polycrystalline $LiNi_{0.5} Mn_{0.3} Co_{0.2} O_2$ positive electrode materials for high voltage Li-Ion cells, J. Electrochem. Soc. 164 (2017) A1534–A1544, https://doi.org/10.1149/2.0991707jes.

[41] J. Hu, H. Wang, B. Xiao, P. Liu, T. Huang, Y. Li, X. Ren, Q. Zhang, J. Liu, X. Ouyang, X. Sun, Challenges and approaches of single-crystal Ni-rich layered cathodes in lithium batteries, Natl. Sci. Rev. 10 (2023), https://doi.org/10.1093/nsr/nwad252.

[42] J.C. Stallard, L. Wheatcroft, S.G. Booth, R. Boston, S.A. Corr, M.F.L. De Volder, B. J. Inkson, N.A. Fleck, Mechanical properties of cathode materials for lithium-ion batteries, Joule 6 (2022) 984–1007, https://doi.org/10.1016/j.joule.2022.04.001.

[43] L. Britala, M. Marinaro, G. Kucinskis, A review of the degradation mechanisms of NCM cathodes and corresponding mitigation strategies, J. Energy Storage 73 (2023) 108875, https://doi.org/10.1016/j.est.2023.108875.

[44] J. Langdon, A. Manthiram, A perspective on single-crystal layered oxide cathodes for lithium-ion batteries, Energy Storage Mater. 37 (2021) 143–160, https://doi.org/10.1016/j.ensm.2021.02.003.

[45] E. McCalla, A.M. Abakumov, M. Saubanère, D. Foix, E.J. Berg, G. Rousse, M.-L. Doublet, D. Gonbeau, P. Novák, G. Van Tendeloo, R. Dominko, J.-M. Tarascon, Visualization of O-O peroxo-like dimers in high-capacity layered oxides for Li-ion batteries, Science 350 (2015) 1516–1521, https://doi.org/10.1126/science.aac8260.

[46] M. Sathiya, G. Rousse, K. Ramesha, C.P. Laisa, H. Vezin, M.T. Sougrati, M. L. Doublet, D. Foix, D. Gonbeau, W. Walker, A.S. Prakash, M. Ben Hassine, L. Dupont, J.M. Tarascon, Reversible anionic redox chemistry in high-capacity layered-oxide electrodes, Nat. Mater. 12 (2013) 827–835, https://doi.org/10.1038/nmat3699.

[47] S.M. Bak, E. Hu, Y. Zhou, X. Yu, S.D. Senanayake, S.J. Cho, K.B. Kim, K.Y. Chung, X.Q. Yang, K.W. Nam, Structural changes and thermal stability of charged LiNixMnyCozO2 cathode materials studied by combined in situ time-resolved XRD and mass spectroscopy, ACS Appl. Mater. Interfaces 6 (2014) 22594–22601, https://doi.org/10.1021/am506712c.

[48] G. Sun, X. Yin, W. Yang, A. Song, C. Jia, W. Yang, Q. Du, Z. Ma, G. Shao, The effect of cation mixing controlled by thermal treatment duration on the electrochemical stability of lithium transition-metal oxides, Phys. Chem. Chem. Phys. 19 (2017) 29886–29894, https://doi.org/10.1039/c7cp05530g.

[49] R. Wang, G. Qian, T. Liu, M. Li, J. Liu, B. Zhang, W. Zhu, S. Li, W. Zhao, W. Yang, X. Ma, Z. Fu, Y. Liu, J. Yang, L. Jin, Y. Xiao, F. Pan, Tuning Li-enrichment in high-Ni layered oxide cathodes to optimize electrochemical performance for Li-ion battery, Nano Energy 62 (2019) 709–717, https://doi.org/10.1016/j.nanoen.2019.05.089.

[50] P. Teichert, G.G. Eshetu, H. Jahnke, E. Figgemeier, Degradation and Aging Routes of ni-rich Cathode Based li-ion Batteries, 2020.

[51] H.R. Morin, D.G. Graczyk, Y. Tsai, S. Lopykinski, H. Iddir, J.C. Garcia, N. Dietz Rago, S. Trask, L.R. Flores, S.B. Son, Z. Zhang, N.M. Johnson, I. Bloom, Transition-metal dissolution from NMC-family oxides: a case study, ACS Appl. Energy Mater. 3 (2020) 2565–2575, https://doi.org/10.1021/acsaem.9b02277.

[52] R. Sahore, D.C. O'Hanlon, A. Tornheim, C.-W. Lee, J.C. Garcia, H. Iddir, M. Balasubramanian, I. Bloom, Revisiting the mechanism behind transition-metal dissolution from delithiated LiNi x Mn y Co z O 2 (NMC) cathodes, J. Electrochem. Soc. 167 (2020) 020513, https://doi.org/10.1149/1945-7111/ab6826.

[53] L. Wu, K.W. Nam, X. Wang, Y. Zhou, J.C. Zheng, X.Q. Yang, Y. Zhu, Structural origin of overcharge-induced thermal instability of Ni-containing layered-cathodes for high-energy-density lithium batteries, Chem. Mater. 23 (2011) 3953–3960, https://doi.org/10.1021/cm201452q.

[54] H. Cha, J. Kim, H. Lee, N. Kim, J. Hwang, J. Sung, M. Yoon, K. Kim, J. Cho, Boosting reaction homogeneity in high-energy lithium-ion battery cathode materials, Adv. Mater. 32 (2020), https://doi.org/10.1002/adma.202003040.

[55] Y. Liu, J. Harlow, J. Dahn, Microstructural observations of "Single Crystal" positive electrode materials before and after long term cycling by cross-section scanning electron microscopy, J. Electrochem. Soc. 167 (2020) 020512, https://doi.org/10.1149/1945-7111/ab6288.

[56] T.M.M. Heenan, A. Wade, C. Tan, J.E. Parker, D. Matras, A.S. Leach, J. B. Robinson, A. Llewellyn, A. Dimitrijevic, R. Jervis, P.D. Quinn, D.J.L. Brett, P. R. Shearing, Identifying the origins of microstructural defects such as cracking within Ni-Rich NMC811 cathode particles for lithium-ion batteries, Adv. Energy Mater. 10 (2020), https://doi.org/10.1002/aenm.202002655.

[57] S.W. Doo, S. Lee, H. Kim, J.H. Choi, K.T. Lee, Hydrophobic Ni-Rich layered oxides as cathode materials for lithium-ion batteries, ACS Appl. Energy Mater. 2 (2019) 6246–6253, https://doi.org/10.1021/acsaem.9b00786.

[58] J. Kim, H. Lee, H. Cha, M. Yoon, M. Park, J. Cho, Prospect and Reality of Ni-Rich Cathode for Commercialization, 2018.

[59] W. Li, A. Dolocan, P. Oh, H. Celio, S. Park, J. Cho, A. Manthiram, Dynamic behaviour of interphases and its implication on high-energy-density cathode materials in lithium-ion batteries, Nat. Commun. 8 (2017), https://doi.org/10.1038/ncomms14589.

[60] W. Lu, J. Zhang, J. Xu, X. Wu, L. Chen, In situ visualized cathode electrolyte interphase on LiCoO2 in high voltage cycling, ACS Appl. Mater. Interfaces 9 (2017) 19313–19318, https://doi.org/10.1021/acsami.7b03024.

[61] Y. Jiang, C. Qin, P. Yan, M. Sui, Origins of capacity and voltage fading of LiCoO2 upon high voltage cycling, J Mater Chem A Mater 7 (2019) 20824–20831, https://doi.org/10.1039/c9ta06579b.

[62] J. Choi, S.Y. Lee, S. Yoon, K.H. Kim, M. Kim, S.H. Hong, The role of Zr doping in stabilizing Li[Ni0.6Co0.2Mn0.2]O2 as a cathode material for lithium-ion batteries, ChemSusChem 12 (2019) 2439–2446, https://doi.org/10.1002/cssc.201900500.

[63] M. Zhang, H. Zhao, M. Tan, J. Liu, Y. Hu, S. Liu, X. Shu, H. Li, Q. Ran, J. Cai, X. Liu, Yttrium modified Ni-rich LiNi0.8Co0.1Mn0.1O2 with enhanced electrochemical performance as high energy density cathode material at 4.5 V high voltage, J. Alloys Compd. 774 (2019) 82–92, https://doi.org/10.1016/j.jallcom.2018.09.281.

[64] T. Weigel, F. Schipper, E.M. Erickson, F.A. Susai, B. Markovsky, D. Aurbach, Structural and electrochemical aspects of LiNi 0.8 Co 0.1 Mn 0.1 O 2 cathode materials doped by various cations, ACS Energy Lett. 4 (2019) 508–516, https://doi.org/10.1021/acsenergylett.8b02302.

[65] R. Du, Y. Bi, W. Yang, Z. Peng, M. Liu, Y. Liu, B. Wu, B. Yang, F. Ding, D. Wang, Improved cyclic stability of LiNi0.8Co0.1Mn0.1O2 via Ti substitution with a cut-off potential of 4.5 v, Ceram. Int. 41 (2015) 7133–7139, https://doi.org/10.1016/j.ceramint.2015.02.026.

[66] P. Hou, H. Zhang, Z. Zi, L. Zhang, X. Xu, Core-Shell and concentration-gradient Cathodes Prepared via co-precipitation Reaction for Advanced lithium-ion Batteries, 2017.

[67] N. Phattharasupakun, J. Wutthiprom, S. Duangdangchote, S. Sarawutanukul, C. Tomon, F. Duriyasart, S. Tubtimkuna, C. Aphirakaramwong, M. Sawangphruk, Core-shell Ni-rich NMC-nanocarbon cathode from scalable solvent-free mechanofusion for high-performance 18650 Li-ion batteries, Energy Storage Mater. 36 (2021) 485–495, https://doi.org/10.1016/j.ensm.2021.01.032.

[68] Y.K. Sun, Z. Chen, H.J. Noh, D.J. Lee, H.G. Jung, Y. Ren, S. Wang, C.S. Yoon, S. T. Myung, K. Amine, Nanostructured high-energy cathode materials for advanced lithium batteries, Nat. Mater. 11 (2012) 942–947, https://doi.org/10.1038/nmat3435.

[69] A.L. Lipson, B.J. Ross, J.L. Durham, D. Liu, M. Leresche, T.T. Fister, L. Liu, K. Kim, Stabilizing NMC 811 Li-Ion battery cathode through a rapid coprecipitation process, ACS Appl. Energy Mater. 4 (2021) 1972–1977, https://doi.org/10.1021/acsaem.0c03112.

[70] Z. Shadike, Y. Chen, E. Hu, J. Zhang, X.-Q. Yang, Interphasial engineering for Ni-rich NMC cathode materials, Trends Chem. 5 (2023) 775–787, https://doi.org/10.1016/j.trechm.2023.08.002.

[71] S. Tan, Z. Shadike, J. Li, X. Wang, Y. Yang, R. Lin, A. Cresce, J. Hu, A. Hunt, I. Waluyo, L. Ma, F. Monaco, P. Cloetens, J. Xiao, Y. Liu, X.-Q. Yang, K. Xu, E. Hu, Additive engineering for robust interphases to stabilize high-Ni layered structures at ultra-high voltage of 4.8 V, Nat. Energy 7 (2022) 484–494, https://doi.org/10.1038/s41560-022-01020-x.

[72] W. Jiang, X. Fan, X. Zhu, Z. Wu, Z. Li, R. Huang, S. Zhao, X. Zeng, G. Hu, B. Zhang, S. Zhang, L. Zhu, L. Yan, M. Ling, L. Wang, C. Liang, Well-dispersed single-crystalline nickel-rich cathode for long-life high-voltage all-solid-state batteries, J. Power Sources 508 (2021) 230335, https://doi.org/10.1016/j.jpowsour.2021.230335.

[73] S. Klein, P. Bärmann, O. Fromm, K. Borzutzki, J. Reiter, Q. Fan, M. Winter, T. Placke, J. Kasnatscheew, Prospects and limitations of single-crystal cathode materials to overcome cross-talk phenomena in high-voltage lithium ion cells, J Mater Chem A Mater 9 (2021) 7546–7555, https://doi.org/10.1039/D0TA11775G.

[74] S.-H. Lee, S.-J. Sim, B.-S. Jin, H.-S. Kim, High performance well-developed single crystal LiNi0.91Co0.06Mn0.03O2 cathode via LiCl-NaCl flux method, Mater. Lett. 270 (2020) 127615, https://doi.org/10.1016/j.matlet.2020.127615.

[75] J. Leng, J. Wang, W. Peng, Z. Tang, S. Xu, Y. Liu, J. Wang, Highly-dispersed submicrometer single-crystal nickel-rich layered cathode: spray synthesis and accelerated lithium-ion transport, Small 17 (2021), https://doi.org/10.1002/smll.202006869.

[76] N. Chen, H. Li, Y. Dai, Y. Miao, W. Xiong, L. Wang, M. Tong, J. Yang, B. Huang, W. Li, H. Li, Mechanism and properties of rod-like Li1.2Mn0.54Ni0.13Co0.13O2 cathode material synthesized by β-MnO2 template for advanced Li-ion batteries, J. Alloys Compd. 867 (2021) 158935, https://doi.org/10.1016/j.jallcom.2021.158935.

[77] Z. Tao, G. Liu, S. Li, M. Yao, Y. Zhang, Rational structure of rod-like single crystal LiNi0.9Co0.05Mn0.04Al0.01O2 cathode for superior-stable lithium-ion battery, Electrochim. Acta 444 (2023) 141975, https://doi.org/10.1016/j.electacta.2023.141975.

[78] S. Zhou, T. Mei, X. Wang, Y. Qian, Crystal structural design of exposed planes: express channels, high-rate capability cathodes for lithium-ion batteries, Nanoscale 10 (2018) 17435–17455, https://doi.org/10.1039/C8NR04842H.

[79] J. Zhu, G. Chen, Single-crystal based studies for correlating the properties and high-voltage performance of li[ni $_x$ Mn $_y$ Co $_{1-x-y}$]O $_2$ cathodes, J Mater Chem A Mater 7 (2019) 5463–5474, https://doi.org/10.1039/C8TA10329A.

[80] X. Zhao, X. Cao, C. Sheng, L. Xu, P. Wu, Y. Zhou, P. He, Y. Tang, H. Zhou, Perspective on high-stability single-crystal Li-Rich cathode materials for Li-Ion batteries, ACS Appl. Mater. Interfaces 16 (2024) 24147–24161, https://doi.org/10.1021/acsami.4c05206.

[81] M. Ge, S. Wi, X. Liu, J. Bai, S. Ehrlich, D. Lu, W. Lee, Z. Chen, F. Wang, Kinetic limitations in single-crystal high-nickel cathodes, Angew. Chem. Int. Ed. 60 (2021) 17350–17355, https://doi.org/10.1002/anie.202012773.

[82] Y. Li, X. Li, C. Du, H. Sun, Y. Zhang, Q. Liu, T. Yang, J. Zhao, C. Delmas, S. J. Harris, H. Chen, Q. Huang, Y. Tang, L. Zhang, T. Zhu, J. Huang, Degradation by kinking in layered cathode materials, ACS Energy Lett. 6 (2021) 3960–3969, https://doi.org/10.1021/acsenergylett.1c01976.

[83] A. Saleem, L.L. Shaw, R. Iqbal, A. Hussain, A.R. Akbar, B. Jabar, S. Rauf, M. K. Majeed, Ni-rich cathode evolution: exploring electrochemical dynamics and strategic modifications to combat degradation, Energy Storage Mater. 69 (2024) 103440, https://doi.org/10.1016/j.ensm.2024.103440.

[84] J. Wang, X. Lu, Y. Zhang, J. Zhou, J. Wang, S. Xu, Grain size regulation for balancing cycle performance and rate capability of LiNi0.9Co0.055Mn0.045O2 single crystal nickel-rich cathode materials, J. Energy Chem. 65 (2022) 681–687, https://doi.org/10.1016/j.jechem.2021.06.017.

[85] Y. Bi, J. Tao, Y. Wu, L. Li, Y. Xu, E. Hu, B. Wu, J. Hu, C. Wang, J.-G. Zhang, Y. Qi, J. Xiao, Reversible planar gliding and microcracking in a single-crystalline Ni-rich cathode, Science 370 (2020) 1313–1317, https://doi.org/10.1126/science.abc3167.

[86] J. Xiao, F. Shi, T. Glossmann, C. Burnett, Z. Liu, From laboratory innovations to materials manufacturing for lithium-based batteries, Nat. Energy 8 (2023) 329–339, https://doi.org/10.1038/s41560-023-01221-y.

[87] H. Liu, M. Wolfman, K. Karki, Y.-S. Yu, E.A. Stach, J. Cabana, K.W. Chapman, P. J. Chupas, Intergranular cracking as a major cause of long-term capacity fading of layered cathodes, Nano Lett. 17 (2017) 3452–3457, https://doi.org/10.1021/acs.nanolett.7b00379.

[88] R. Jung, R. Morasch, P. Karayaylali, K. Phillips, F. Maglia, C. Stinner, Y. Shao-Horn, H.A. Gasteiger, Effect of ambient storage on the degradation of Ni-Rich positive electrode materials (NMC811) for Li-Ion batteries, J. Electrochem. Soc. 165 (2018) A132–A141, https://doi.org/10.1149/2.0401802jes.

[89] W. Song, J. Harlow, E. Logan, H. Hebecker, M. Coon, L. Molino, M. Johnson, J. Dahn, M. Metzger, A systematic study of electrolyte additives in single crystal and bimodal LiNi $_{0.8}$ Mn $_{0.1}$ Co $_{0.1}$ O $_2$/Graphite pouch cells, J. Electrochem. Soc. 168 (2021) 090503, https://doi.org/10.1149/1945-7111/ac1e55.

[90] S.S. Shishvan, N.A. Fleck, R.M. McMeeking, V.S. Deshpande, Cracking and associated volumetric expansion of NMC811 secondary particles, J. Power Sources 588 (2023) 233745, https://doi.org/10.1016/j.jpowsour.2023.233745.

[91] G.J. Páez Fajardo, E. Fiamegkou, J.A. Gott, H. Wang, I. Temprano, I.D. Seymour, M.J.W. Ogley, A.S. Menon, I.E.L. Stephens, M. Ans, T.-L. Lee, P.K. Thakur, W. M. Dose, M.F.L. De Volder, C.P. Grey, L.F.J. Piper, Synergistic degradation mechanism in single crystal Ni-Rich NMC//Graphite cells, ACS Energy Lett. 8 (2023) 5025–5031, https://doi.org/10.1021/acsenergylett.3c01596.

[92] B.N. Abraham, O.F. Ngasoh, N.E. Offia-Kalu, V.C. Anye, D. Amune, U.C. Obi, A. Bello, Understanding degradation mechanisms in single crystal NMC cathodes for enhanced lithium-ion battery performance - a review, in: 2023 2nd International Conference on Multidisciplinary Engineering and Applied Science (ICMEAS), IEEE, 2023, pp. 1–6.

[93] H. Zhang, X. He, Z. Chen, Y. Yang, H. Xu, L. Wang, X. He, Single-crystalline ni-rich LiNi $_x$ Mn $_y$ Co $_{1-x-y}$ O $_2$ cathode materials: a perspective, Adv. Energy Mater. 12 (2022), https://doi.org/10.1002/aenm.202202022.

[94] Y. Chen, W. Luan, X. Zhu, H. Chen, Mechanical degradation behavior of single crystal LiNixMnyCozO2 cathode in Li-Ion battery by indentation analysis, J. Pressure Vessel Technol. 144 (2022), https://doi.org/10.1115/1.4053530.

[95] L. Saunders, J. Wang, U. Stimming, Evaluating single-crystal and polycrystalline NMC811 electrodes in lithium-ion cells via non-destructive EIS alone, J. Appl. Electrochem. 52 (2022) 1305–1316, https://doi.org/10.1007/s10800-022-01713-x.

[96] X. Ou, T. Liu, W. Zhong, X. Fan, X. Guo, X. Huang, L. Cao, J. Hu, B. Zhang, Y. S. Chu, G. Hu, Z. Lin, M. Dahbi, J. Alami, K. Amine, C. Yang, J. Lu, Enabling high energy lithium metal batteries via single-crystal Ni-rich cathode material co-doping strategy, Nat. Commun. 13 (2022) 2319, https://doi.org/10.1038/s41467-022-30020-4.

[97] Q. Xie, W. Li, A. Manthiram, A Mg-Doped high-nickel layered oxide cathode enabling safer, high-energy-density Li-Ion batteries, Chem. Mater. 31 (2019) 938–946, https://doi.org/10.1021/acs.chemmater.8b03900.

[98] F. Zhang, S. Lou, S. Li, Z. Yu, Q. Liu, A. Dai, C. Cao, M.F. Toney, M. Ge, X. Xiao, W.-K. Lee, Y. Yao, J. Deng, T. Liu, Y. Tang, G. Yin, J. Lu, D. Su, J. Wang, Surface regulation enables high stability of single-crystal lithium-ion cathodes at high voltage, Nat. Commun. 11 (2020) 3050, https://doi.org/10.1038/s41467-020-16824-2.

[99] X. Fan, Y. Huang, H. Wei, L. Tang, Z. He, C. Yan, J. Mao, K. Dai, J. Zheng, Surface modification engineering enabling 4.6 V single-crystalline ni-rich cathode with superior long-term cyclability, Adv. Funct. Mater. 32 (2022), https://doi.org/10.1002/adfm.202109421.

[100] J. Zhang, P. Wang, P. Bai, H. Wan, S. Liu, S. Hou, X. Pu, J. Xia, W. Zhang, Z. Wang, B. Nan, X. Zhang, J. Xu, C. Wang, Interfacial design for a 4.6 V high-voltage single-crystalline $LiCoO_2$ cathode, Adv. Mater. 34 (2022), https://doi.org/10.1002/adma.202108353.

[101] G. Liu, M. Li, N. Wu, L. Cui, X. Huang, X. Liu, Y. Zhao, H. Chen, W. Yuan, Y. Bai, Single-crystalline particles: an effective way to ameliorate the intragranular cracking, thermal stability, and capacity fading of the $LiNi_{0.6}Co_{0.2}Mn_{0.2}O_2$ electrodes, J. Electrochem. Soc. 165 (2018) A3040–A3047, https://doi.org/10.1149/2.0491813jes.

[102] T. Kimijima, N. Zettsu, K. Teshima, Growth manner of octahedral-shaped $Li(Ni_{1/3}Co_{1/3}Mn_{1/3})O_2$ single crystals in molten Na_2SO_4, Cryst. Growth Des. 16 (2016) 2618–2623, https://doi.org/10.1021/acs.cgd.5b01723.

[103] X. Xu, H. Huo, J. Jian, L. Wang, H. Zhu, S. Xu, X. He, G. Yin, C. Du, X. Sun, Lithium-ion batteries: radially oriented single-crystal primary nanosheets enable ultrahigh rate and cycling properties of $LiNi_{0.8}Co_{0.1}Mn_{0.1}O_2$ cathode material for lithium-ion batteries (adv. Energy mater. 15/2019), Adv. Energy Mater. 9 (2019), https://doi.org/10.1002/aenm.201970051.

[104] K. Park, H. Jung, L. Kuo, P. Kaghazchi, C.S. Yoon, Y. Sun, Improved cycling stability of $Li[Ni_{0.90}Co_{0.05}Mn_{0.05}]O_2$ through microstructure modification by boron doping for Li-Ion batteries, Adv. Energy Mater. 8 (2018), https://doi.org/10.1002/aenm.201801202.

[105] Y. Liu, X. Fan, B. Luo, Z. Zhao, J. Shen, Z. Liu, Z. Xiao, B. Zhang, J. Zhang, L. Ming, X. Ou, Understanding the enhancement effect of boron doping on the electrochemical performance of single-crystalline Ni-rich cathode materials, J. Colloid Interface Sci. 604 (2021) 776–784, https://doi.org/10.1016/j.jcis.2021.07.027.

[106] T. Li, X. Chang, Y. Xin, Y. Liu, H. Tian, Synergistic strategy using doping and polymeric coating enables high-performance high-nickel layered cathodes for lithium-ion batteries, J. Phys. Chem. C 127 (2023) 8448–8461, https://doi.org/10.1021/acs.jpcc.3c00951.

[107] J. Shen, B. Zhang, X. He, B. Xiao, Z. Xiao, X. Li, X. Ou, Synergistic regulation of kinetic reaction pathway and surface structure degradation in single-crystal high-nickel cathodes, J. Colloid Interface Sci. 629 (2023) 388–398, https://doi.org/10.1016/j.jcis.2022.08.184.

[108] G.-W. Yoo, B.-C. Jang, J.-T. Son, Novel design of core shell structure by NCA modification on NCM cathode material to enhance capacity and cycle life for lithium secondary battery, Ceram. Int. 41 (2015) 1913–1916, https://doi.org/10.1016/j.ceramint.2014.09.077.

[109] H. Liu, Y.P. Wu, E. Rahm, R. Holze, H.Q. Wu, Cathode materials for lithium ion batteries prepared by sol-gel methods, J. Solid State Electrochem. 8 (2004) 450–466, https://doi.org/10.1007/s10008-004-0521-1.

[110] S.H. Ju, Y.C. Kang, The characteristics of Ni–Co–Mn–O precursor and Li(Ni1/3Co1/3Mn1/3)O2 cathode powders prepared by spray pyrolysis, Ceram. Int. 35 (2009) 1205–1210, https://doi.org/10.1016/j.ceramint.2008.06.007.

[111] Y. Zou, X. Yang, C. Lv, T. Liu, Y. Xia, L. Shang, G.I.N. Waterhouse, D. Yang, T. Zhang, Multishelled Ni-rich $Li(Ni_xCo_yMn_z)O_2$ hollow fibers with low cation mixing as high-performance cathode materials for li-ion batteries, Adv. Sci. 4 (2017), https://doi.org/10.1002/advs.201600262.

[112] B. N, D. H, Review on synthesis, characterizations, and electrochemical properties of cathode materials for lithium ion batteries, J. Mater. Sci. Eng. 5 (2016), https://doi.org/10.4172/2169-0022.1000258.

[113] Z. Li, K. Zhu, J. Li, X. Wang, Morphological and orientational diversity of $LiFePO_4$ crystallites: remarkable reaction path dependence in hydrothermal/solvothermal syntheses, CrystEngComm 16 (2014) 10112–10122, https://doi.org/10.1039/C4CE01397B.

[114] Y. Xue, Z. Wang, F. Yu, Y. Zhang, G. Yin, Ethanol-assisted hydrothermal synthesis of $LiNi_{0.5}Mn_{1.5}O_4$ with excellent long-term cyclability at high rate for lithium-ion batteries, J. Mater. Chem. A 2 (2014) 4185–4191, https://doi.org/10.1039/C3TA14567K.

[115] N. Zhou, E. Uchaker, H.-Y. Wang, M. Zhang, S.-Q. Liu, Y.-N. Liu, X. Wu, G. Cao, H. Li, Additive-free solvothermal synthesis of hierarchical flower-like LiFePO4/C mesocrystal and its electrochemical performance, RSC Adv. 3 (2013) 19366, https://doi.org/10.1039/c3ra42855a.

[116] J. Song, L. Wang, G. Shao, M. Shi, Z. Ma, G. Wang, W. Song, S. Liu, C. Wang, Controllable synthesis, morphology evolution and electrochemical properties of $LiFePO_4$ cathode materials for Li-ion batteries, Phys. Chem. Chem. Phys. 16 (2014) 7728–7733, https://doi.org/10.1039/C4CP00251B.

[117] G. Qin, S. Xue, Q. Ma, C. Wang, The morphology controlled synthesis of 3D networking $LiFePO_4$ with multiwalled-carbon nanotubes for Li-ion batteries, CrystEngComm 16 (2014) 260–269, https://doi.org/10.1039/C3CE41967C.

[118] Y. Wang, G. Cao, Developments in nanostructured cathode materials for high-performance lithium-ion batteries, Adv. Mater. 20 (2008) 2251–2269, https://doi.org/10.1002/adma.200702242.

[119] Freeze-drying [Drying by sublimation, J. Am. Med. Assoc. 142 (1950) 767, https://doi.org/10.1001/jama.1950.02910280075034.

[120] V. Palomares, A. Goñi, I.G. de Muro, I. de Meatza, M. Bengoechea, O. Miguel, T. Rojo, New freeze-drying method for LiFePO4 synthesis, J. Power Sources 171 (2007) 879–885, https://doi.org/10.1016/j.jpowsour.2007.06.161.

[121] V. Palomares, A. Goni, I.G. de Muro, L. Lezama, I. de Meatza, M. Bengoechea, I. Boyano, T. Rojo, Near heterosite Li0.1FePO4 phase formation as atmospheric aging product of LiFePO4/C composite. Electrochemical, magnetic and EPR study, J. Electrochem. Soc. 158 (2011) A1042, https://doi.org/10.1149/1.3611435.

[122] Y. Han, S. Heng, Y. Wang, Q. Qu, H. Zheng, Anchoring interfacial nickel cations on single-crystal $LiNi_{0.8}Co_{0.1}Mn_{0.1}O_2$ cathode surface via controllable electron transfer, ACS Energy Lett. 5 (2020) 2421–2433, https://doi.org/10.1021/acsenergylett.0c01032.

[123] Q. Chen, A.J. Rondinone, B.C. Chakoumakos, Z. John Zhang, Synthesis of superparamagnetic MgFe2O4 nanoparticles by coprecipitation, J. Magn. Magn Mater. 194 (1999) 1–7, https://doi.org/10.1016/S0304-8853(98)00585-X.

[124] A.I. Petrov, D.V. Volodkin, G.B. Sukhorukov, Protein-calcium carbonate coprecipitation: a tool for protein encapsulation, Biotechnol. Prog. 21 (2008) 918–925, https://doi.org/10.1021/bp0495825.

[125] H. Li, Q. Xu, X.-X. Shi, D.-W. Song, L.-Q. Zhang, Electrochemical performance of LiNi0.5Mn0.5O2 with different synthesis methods, Rare Met. 34 (2015) 580–585, https://doi.org/10.1007/s12598-013-0088-z.

[126] D. Wang, I. Belharouak, G.M. Koenig, G. Zhou, K. Amine, Growth mechanism of Ni0.3Mn0.7CO3 precursor for high capacity Li-ion battery cathodes, J. Mater. Chem. 21 (2011) 9290, https://doi.org/10.1039/c1jm11077b.

[127] Z. Xu, L. Xiao, F. Wang, K. Wu, L. Zhao, M.-R. Li, H.-L. Zhang, Q. Wu, J. Wang, Effects of precursor, synthesis time and synthesis temperature on the physical and electrochemical properties of Li(Ni1−x−yCoxMny)O2 cathode materials, J. Power Sources 248 (2014) 180–189, https://doi.org/10.1016/j.jpowsour.2013.09.064.

[128] J. Li, M. Zhang, D. Zhang, Y. Yan, Z. Li, Z. Nie, Effect of sintering conditions on electrochemical properties of LiNi0.8Co0.1Mn0.1O2 as cathode material, Int. J. Electrochem. Sci. 15 (2020) 1881–1892, https://doi.org/10.20964/2020.03.63.

[129] J.-Z. Kong, F. Zhou, C.-B. Wang, X.-Y. Yang, H.-F. Zhai, H. Li, J.-X. Li, Z. Tang, S.-Q. Zhang, Effects of li source and calcination temperature on the electrochemical properties of LiNi0.5Co0.2Mn0.3O2 lithium-ion cathode materials, J. Alloys Compd. 554 (2013) 221–226, https://doi.org/10.1016/j.jallcom.2012.11.090.

[130] K. Wu, F. Wang, L. Gao, M.-R. Li, L. Xiao, L. Zhao, S. Hu, X. Wang, Z. Xu, Q. Wu, Effect of precursor and synthesis temperature on the structural and electrochemical properties of Li(Ni0.5Co0.2Mn0.3)O2, Electrochim. Acta 75 (2012) 393–398, https://doi.org/10.1016/j.electacta.2012.05.035.

[131] D. Wang, I. Belharouak, L.H. Ortega, X. Zhang, R. Xu, D. Zhou, G. Zhou, K. Amine, Synthesis of high capacity cathodes for lithium-ion batteries by morphology-tailored hydroxide co-precipitation, J. Power Sources 274 (2015) 451–457, https://doi.org/10.1016/j.jpowsour.2014.10.016.

[132] Y. Yang, S. Xu, M. Xie, Y. He, G. Huang, Y. Yang, Growth mechanisms for spherical mixed hydroxide agglomerates prepared by co-precipitation method: a case of Ni1/3Co1/3Mn1/3(OH)2, J. Alloys Compd. 619 (2015) 846–853, https://doi.org/10.1016/j.jallcom.2014.08.152.

[133] X. Sun, J. Kim, W.S. Kim, Spherical agglomeration of nickel-manganese-cobalt hydroxide in turbulent batchelor vortex flow, Chem. Eng. J. 421 (2021), https://doi.org/10.1016/j.cej.2021.129924.

[134] W. Hua, W. Liu, M. Chen, S. Indris, Z. Zheng, X. Guo, M. Bruns, T.-H. Wu, Y. Chen, B. Zhong, S. Chou, Y.-M. Kang, H. Ehrenberg, Unravelling the growth mechanism of hierarchically structured Ni1/3Co1/3Mn1/3(OH)2 and their application as precursors for high-power cathode materials, Electrochim. Acta 232 (2017) 123–131, https://doi.org/10.1016/j.electacta.2017.02.105.

[135] Q. Zhu, H. Xiao, R. Zhang, S. Geng, Q. Huang, Effect of impeller type on preparing spherical and dense Ni1−−Co Mn (OH)2 precursor via continuous co-precipitation in pilot scale: a case of Ni0·6Co0·2Mn0·2(OH)2, Electrochim. Acta 318 (2019) 1–13, https://doi.org/10.1016/j.electacta.2019.06.008.

[136] X. Sun, J. Kim, W.-S. Kim, Spherical agglomeration of nickel-manganese-cobalt hydroxide in turbulent batchelor vortex flow, Chem. Eng. J. 421 (2021) 129924, https://doi.org/10.1016/j.cej.2021.129924.

[137] X. Sun, J. Kim, W.-S. Kim, Spherical agglomeration of nickel-manganese-cobalt hydroxide in turbulent batchelor vortex flow, Chem. Eng. J. 421 (2021) 129924, https://doi.org/10.1016/j.cej.2021.129924.

[138] V. Pimenta, M. Sathiya, D. Batuk, A.M. Abakumov, D. Giaume, S. Cassaignon, D. Larcher, J.-M. Tarascon, Synthesis of Li-Rich NMC: a comprehensive study, Chem. Mater. 29 (2017) 9923–9936, https://doi.org/10.1021/acs.chemmater.7b03230.

[139] W. Hua, Z. Wu, M. Chen, M. Knapp, X. Guo, S. Indris, J.R. Binder, N.N. Bramnik, B. Zhong, H. Guo, S. Chou, Y.-M. Kang, H. Ehrenberg, Shape-controlled synthesis of hierarchically layered lithium transition-metal oxide cathode materials by shear exfoliation in continuous stirred-tank reactors, J Mater Chem A Mater 5 (2017) 25391–25400, https://doi.org/10.1039/C7TA08073E.

[140] Y. Yang, S. Xu, M. Xie, Y. He, G. Huang, Y. Yang, Growth mechanisms for spherical mixed hydroxide agglomerates prepared by co-precipitation method: a

case of Ni1/3Co1/3Mn1/3(OH)2, J. Alloys Compd. 619 (2015) 846–853, https://doi.org/10.1016/j.jallcom.2014.08.152.

[141] A. van Bommel, J.R. Dahn, Analysis of the growth mechanism of coprecipitated spherical and dense nickel, manganese, and cobalt-containing hydroxides in the presence of aqueous ammonia, Chem. Mater. 21 (2009) 1500–1503, https://doi.org/10.1021/cm803144d.

[142] M.-H. Lee, Y.-J. Kang, S.-T. Myung, Y.-K. Sun, Synthetic optimization of Li[Ni1/3Co1/3Mn1/3]O2 via co-precipitation, Electrochim. Acta 50 (2004) 939–948, https://doi.org/10.1016/j.electacta.2004.07.038.

[143] L. Li, M. Xu, Z. Chen, X. Zhou, Q. Zhang, H. Zhu, C. Wu, K. Zhang, High-performance lithium-rich layered oxide materials: effects of chelating agents on microstructure and electrochemical properties, Electrochim. Acta 174 (2015) 446–455, https://doi.org/10.1016/j.electacta.2015.05.171.

[144] J.H. Mugumya, M.L. Rasche, R.F. Rafferty, A. Patel, S. Mallick, M. Mou, J. A. Bobb, R.B. Gupta, M. Jiang, Synthesis and theoretical modeling of suitable Co-precipitation conditions for producing NMC111 cathode material for lithium-ion batteries, Energy & Fuels 36 (2022) 12261–12270, https://doi.org/10.1021/acs.energyfuels.2c01805.

[145] Y. Shen, Y. Wu, H. Xue, S. Wang, D. Yin, L. Wang, Y. Cheng, Insight into the coprecipitation-controlled crystallization reaction for preparing lithium-layered oxide cathodes, ACS Appl. Mater. Interfaces 13 (2021) 717–726, https://doi.org/10.1021/acsami.0c19493.

[146] Y. Shen, H. Xue, S. Wang, D. Zhang, D. Yin, L. Wang, Y. Cheng, Ammonia-low coprecipitation synthesis of lithium layered oxide cathode material for high-performance battery, Chem. Eng. J. 411 (2021) 128487, https://doi.org/10.1016/j.cej.2021.128487.

[147] P. Barai, Z. Feng, H. Kondo, V. Srinivasan, Multiscale computational model for particle size evolution during coprecipitation of Li-Ion battery cathode precursors, J. Phys. Chem. B 123 (2019) 3291–3303, https://doi.org/10.1021/acs.jpcb.8b12004.

[148] J. Cho, $LiNi_{0.74}Co_{0.26-x}Mg_xO_2$ cathode material for a Li-Ion cell, Chem. Mater. 12 (2000) 3089–3094, https://doi.org/10.1021/cm000153l.

[149] H. Qiu, Y. Wang, S. Ye, Rationally-directed synthesis and characterization of nickel-rich cathode material for lithium ion battery, Energy Technol. 6 (2018) 2419–2428, https://doi.org/10.1002/ente.201800415.

[150] C. Xu, S. Guan, L. Li, C. Sun, B. An, X. Geng, Electrochemical properties of LiNi0.6Co0.2Mn0.2O2 cathode materials prepared with different ammonia content, Coatings 11 (2021) 932, https://doi.org/10.3390/coatings11080932.

[151] K.-H. Hu, Y.-Y. He, C.-Q. Zhu, K. Zhou, Q. Chen, Z.-M. Yang, B.-R. Wan, E.-Q. Yang, T.-T. Zhang, Y.-D. Qin, Insight into the evolution of precursor and electrochemical performance of Ni-rich cathode modulated by ammonia during hydroxide precipitation, J. Alloys Compd. 803 (2019) 538–545, https://doi.org/10.1016/j.jallcom.2019.06.309.

[152] L.G. Sillén, A. Martell, J. Bjerrum, G. Schwarzenbach, Stability Constants of metal-ion Complexes, The Chemical Society, London, UK, 1964.

[153] S. Hwa Lee, K. Young Kwon, B. Kil Choi, H. Deog Yoo, A kinetic descriptor to optimize Co-precipitation of nickel-rich cathode precursors for Lithium-ion batteries, J. Electroanal. Chem. 924 (2022) 116828, https://doi.org/10.1016/j.jelechem.2022.116828.

[154] Theodore E. Brown, H.Eugene H. LeMay, Bruce E. Bursten, Catherine Murphy, Patrick Woodward: Chemistry, The Central Science, Prentice Hall, 2008.

[155] Raymond Chang, Kenneth Goldsby, Chemistry, McGraw-Hill Education, 2015.

[156] K.N. Han, E. Narita, F. Lawson, The coprecipitation behavior of Co(II) and Ni(II) with Fe(III), Cr(III) and Al(III) from aqueous ammoniacal solutions, Hydrometallurgy 8 (1982) 365–377, https://doi.org/10.1016/0304-386X(82)90062-7.

[157] D.-L. Vu, J. Lee, Properties of LiNi0.8Co0.1Mn0.1O2 as a high energy cathode material for lithium-ion batteries, Kor. J. Chem. Eng. 33 (2016) 514–526, https://doi.org/10.1007/s11814-015-0154-3.

[158] D. Kashchiev, On the relation between nucleation work, nucleus size, and nucleation rate, J. Chem. Phys. 76 (1982) 5098–5102, https://doi.org/10.1063/1.442808.

[159] D. Ren, Y. Shen, Y. Yang, L. Shen, B.D.A. Levin, Y. Yu, D.A. Muller, H.D. Abruña, Systematic optimization of battery materials: key parameter optimization for the scalable synthesis of uniform, high-energy, and high stability $LiNi_{0.6}Mn_{0.2}Co_{0.2}O_2$ cathode material for lithium-ion batteries, ACS Appl. Mater. Interfaces 9 (2017) 35811–35819, https://doi.org/10.1021/acsami.7b10155.

[160] L. Liang, K. Du, Z. Peng, Y. Cao, J. Duan, J. Jiang, G. Hu, Co–precipitation synthesis of Ni0.6Co0.2Mn0.2(OH)2 precursor and characterization of LiNi0.6Co0.2Mn0.2O2 cathode material for secondary lithium batteries, Electrochim. Acta 130 (2014) 82–89, https://doi.org/10.1016/j.electacta.2014.02.100.

[161] K.K. Cheralathan, N.Y. Kang, H.S. Park, Y.J. Lee, W.C. Choi, Y.S. Ko, Y.-K. Park, Preparation of spherical LiNi0.80Co0.15Mn0.05O2 lithium-ion cathode material by continuous co-precipitation, J. Power Sources 195 (2010) 1486–1494, https://doi.org/10.1016/j.jpowsour.2009.08.101.

[162] A.R. Nichols, J.H. Walton, The autoxidation of manganous hydroxide, J. Am. Chem. Soc. 64 (1942) 1866–1870, https://doi.org/10.1021/ja01260a034.

[163] J. Meyer, R. Nerlich, Zur Kenntnis des dreiwertigen Mangans. II, Z. Anorg. Allg. Chem. 116 (1921) 117–136, https://doi.org/10.1002/zaac.19211160111.

[164] Pier Giorgio Schiavi, Mario Branchi, Eleonora Casalese, Pietro Altimari, Maria Assunta Navarra, Francesca Pagnanelli, Resynthesis of NMC111 cathodic material from real waste lithium ion batteries, Chem Eng Trans 86 (2021) 463–468.

[165] S. Arrhenius, Über die Reaktionsgeschwindigkeit bei der Inversion von Rohrzucker durch Säuren, Zeitschrift für Physikalische Chemie 4U (1889) 226–248, https://doi.org/10.1515/zpch-1889-0416.

[166] E. Nielsen Arne, Kinetics of Precipitation, 1964.

[167] H. Ronduda, M. Zybert, A. Szczęsna-Chrzan, T. Trzeciak, A. Ostrowski, D. Szymański, W. Wieczorek, W. Raróg-Pilecka, M. Marcinek, On the sensitivity of the ni-rich layered cathode materials for li-ion batteries to the different calcination conditions, Nanomaterials 10 (2020) 1–21, https://doi.org/10.3390/nano10102018.

[168] M. Wolfman, X. Wang, J.C. Garcia, P. Barai, J.E. Stubbs, P.J. Eng, O. Kahvecioglu, T.L. Kinnibrugh, K.E. Madsen, H. Iddir, V. Srinivasan, T.T. Fister, The importance of surface oxygen for lithiation and morphology evolution during calcination of high-nickel NMC cathodes, Adv. Energy Mater. 12 (2022), https://doi.org/10.1002/aenm.202102951.

[169] J. Zheng, P. Yan, L. Estevez, C. Wang, J.G. Zhang, Effect of calcination temperature on the electrochemical properties of nickel-rich LiNi0.76Mn0.14Co0.10O2 cathodes for lithium-ion batteries, Nano Energy 49 (2018) 538–548, https://doi.org/10.1016/j.nanoen.2018.04.077.

[170] S. Rahayu, A.U. Saudi, R. Tasomara, M.D. Gumelar, W.T. Utami, A.U. Hapsari, J. Raharjo, A. Rifai, D.S. Khaerudini, S. Husin, D.A. Saputra, H. Yuliani, Y. A. Andrameda, G. Taqwatomo, O.P. Arjasa, D. Damisih, A. Hardiansyah, R. D. Pravitasari, A. Agustanhakri, A.H. Budiman, The calcination temperature effect on crystal structure of LiNi1/3Mn1/3Co1/3O2 cathode material for lithium-ion batteries, Journal of Batteries for Renewable Energy and Electric Vehicles 1 (2023) 68–75, https://doi.org/10.59046/jbrev.v1i02.22.

[171] T. Entwistle, E. Sanchez-Perez, G.J. Murray, N. Anthonisamy, S.A. Cussen, Co-precipitation synthesis of nickel-rich cathodes for Li-ion batteries, Energy Rep. 8 (2022) 67–73, https://doi.org/10.1016/j.egyr.2022.06.110.

[172] M. Zybert, H. Ronduda, A. Szczęsna, T. Trzeciak, A. Ostrowski, E. Żero, W. Wieczorek, W. Raróg-Pilecka, M. Marcinek, Different strategies of introduction of lithium ions into nickel-manganese-cobalt carbonate resulting in LiNi0.6Mn0.2Co0.2O2 (NMC622) cathode material for Li-ion batteries, Solid State Ionics 348 (2020) 115273, https://doi.org/10.1016/j.ssi.2020.115273.

[173] S. Jo, J. Han, S. Seo, O. Kwon, S. Choi, J. Zhang, H. Hyun, J. Oh, J. Kim, J. Chung, H. Kim, J. Wang, J. Bae, J. Moon, Y. Park, M. Hong, M. Kim, Y. Liu, I. Sohn, K. Jung, J. Lim, Solid-state reaction heterogeneity during calcination of lithium-ion battery cathode, Adv. Mater. 35 (2023), https://doi.org/10.1002/adma.202207076.

[174] M. Ihalainen, M. Kortelainen, A. Mesceriakovas, T. Karhunen, S.-M. Mesceriakove, D. Lindberg, J.T.T. Leskinen, T. Kankaanpää, J. Jokiniemi, A. Lähde, Synthesis of solid NMC622 particles by spray drying, post-annealing and lithiation, Adv. Powder Technol. 34 (2023) 104187, https://doi.org/10.1016/j.apt.2023.104187.

[175] Octave Levenspiel, Chemical Reaction Engineering, Wiley, 1999.

[176] G.F. Froment, K.B. Bischoff, J. Wiley, Chemical Reactor Analysis and Design, 1979.

[177] X. Liu, J. Shi, B. Zheng, Z. Chen, Y. Su, M. Zhang, C. Xie, M. Su, Y. Yang, Constructing a high-energy and durable single-crystal NCM811 cathode for all-solid-state batteries by a surface engineering strategy, ACS Appl. Mater. Interfaces 13 (2021) 41669–41679, https://doi.org/10.1021/acsami.1c11419.

[178] J. Liu, H. Chen, J. Xie, Z. Sun, N. Wu, B. Wu, Morphology and particle growth of a two-phase Ni/Mn precursor for high-capacity Li-rich cathode materials, J. Appl. Electrochem. 44 (2014) 225–232, https://doi.org/10.1007/s10800-013-0633-3.

[179] L. Huang, L. Liu, H. Wu, Y. Wang, H. Liu, Y. Zhang, Optimization of synthesis parameters for uniform sphere-like Li1.2Mn0.54Ni0.13Co0.13O2 as high performance cathode material for lithium ion batteries, J. Alloys Compd. 775 (2019) 921–930, https://doi.org/10.1016/j.jallcom.2018.10.173.

[180] B. Cao, H.-T. Fang, D. Li, Y. Chen, Controlled synthesis of single–crystalline Ni–Rich cathodes for high-performance lithium–ion batteries, ACS Appl. Mater. Interfaces 14 (2022) 53667–53676, https://doi.org/10.1021/acsami.2c13832.

[181] R. Zhang, Z. Meng, X. Ma, M. Chen, B. Chen, Y. Zheng, Z. Yao, P. Vanaphuti, Bong, Z. Yang, Y. Wang, Understanding fundamental effects of Cu impurity in different forms for recovered LiNi0.6Co0.2Mn0.2O2 cathode materials, Nano Energy 78 (2020) 105214, https://doi.org/10.1016/j.nanoen.2020.105214.

[182] M. Wang, M. Luo, Y. Chen, L. Chen, S. Yan, Y. Ren, M. Chu, A new approach to improve the electrochemical performance of Li-rich cathode material by precursor pretreatment, J. Alloys Compd. 696 (2017) 891–899, https://doi.org/10.1016/j.jallcom.2016.12.054.

[183] Y. Song, M. Wang, J. Li, H. Cui, H. Su, Y. Liu, Controllable synthesis of LiNi1/3Co1/3Mn1/3O2 electrode material via a high shear mixer-assisted precipitation process, Chem. Eng. J. 419 (2021) 129281, https://doi.org/10.1016/j.cej.2021.129281.

[184] H. Qin, C. Zhang, Q. Xu, X. Dang, W. Li, K. Lei, L. Zhou, J. Zhang, Geometrical improvement of inline high shear mixers to intensify micromixing performance, Chem. Eng. J. 319 (2017) 307–320, https://doi.org/10.1016/j.cej.2017.02.150.

[185] W. Hua, Z. Wu, M. Chen, M. Knapp, X. Guo, S. Indris, J.R. Binder, N.N. Bramnik, B. Zhong, H. Guo, S. Chou, Y.-M. Kang, H. Ehrenberg, Shape-controlled synthesis of hierarchically layered lithium transition-metal oxide cathode materials by shear exfoliation in continuous stirred-tank reactors, J Mater Chem A Mater 5 (2017) 25391–25400, https://doi.org/10.1039/C7TA08073E.

[186] M.L. Para, M. Alidoost, M. Shiea, G. Boccardo, A. Buffo, A.A. Barresi, D. Marchisio, A modelling and experimental study on the co-precipitation of Ni0.8Mn0.1Co0.1(OH)2 as precursor for battery cathodes, Chem. Eng. Sci. 254 (2022) 117634, https://doi.org/10.1016/j.ces.2022.117634.

[187] M.L. Para, A. Querio, J. Amici, D. Versaci, A.A. Barresi, S. Bodoardo, D. Marchisio, Electrochemical performance optimization of NMC811 through the structure design of its precursor, J. Electroanal. Chem. 943 (2023) 117630, https://doi.org/10.1016/j.jelechem.2023.117630.

[188] Y. Wu, Q. Zhao, R. Wang, W. Xu, M. Zhang, Y. Li, B. Zhong, Y. Song, X. Guo, Rapid preparation of cobalt-free lithium rich cathode materials with layered structure and excellent performance via capillary microreactors, Chem. Eng. Sci. 284 (2024) 119459, https://doi.org/10.1016/j.ces.2023.119459.

[189] J.M. Kim, S.M. Chang, J.H. Chang, W.S. Kim, Agglomeration of nickel/cobalt/manganese hydroxide crystals in couette-taylor crystallizer, Colloids Surf. A Physicochem. Eng. Asp. 384 (2011) 31–39, https://doi.org/10.1016/j.colsurfa.2011.03.016.

[190] Y.B. Hendri, L.-Y. Kuo, M. Seenivasan, Y.-S. Wu, S.-H. Wu, J.-K. Chang, R. Jose, M. Ihrig, P. Kaghazchi, C.-C. Yang, Two birds with one stone: one-pot concurrent Ta-doping and -coating on Ni-rich LiNi0.92Co0.04Mn0.04O2 cathode materials with fiber-type microstructure and Li+-conducting layer formation, J. Colloid Interface Sci. 661 (2024) 289–306, https://doi.org/10.1016/j.jcis.2024.01.094.

[191] J. Jeyakumar, M. Seenivasan, Y.-S. Wu, S.-H. Wu, J.-K. Chang, R. Jose, C.-C. Yang, Preparation of long-term cycling stable ni-rich concentration–gradient NCMA cathode materials for li-ion batteries, J. Colloid Interface Sci. 639 (2023) 145–159, https://doi.org/10.1016/j.jcis.2023.02.064.

[192] S. Aryal, J.L. Durham, A.L. Lipson, K.Z. Pupek, O. Kahvecioglu, Roles of Mn and Co in Ni-rich layered oxide cathodes synthesized utilizing a Taylor vortex reactor, Electrochim. Acta 391 (2021) 138929, https://doi.org/10.1016/j.electacta.2021.138929.

[193] M. Piton, F. Huchet, B. Cazacliu, O. Le Corre, Heat transport in rotating annular duct: a short review, Energies 15 (2022) 8633, https://doi.org/10.3390/en15228633.

[194] M. Schrimpf, J. Esteban, H. Warmeling, T. Färber, A. Behr, A.J. Vorholt, <scp>Taylor-Couette</scp> reactor: principles, design, and applications, AIChE J. 67 (2021), https://doi.org/10.1002/aic.17228.

[195] N.M. Jobst, M. Mancini, M. Hölzle, M. Wohlfahrt-Mehrens, P. Axmann, Understanding the low-voltage behavior of stoichiometric over lithiated spinel $Li_{1+x}\,Ni_{0.5}\,Mn_{1.5}\,O_4$: an electrochemical investigation, J. Electrochem. Soc. 170 (2023) 020513, https://doi.org/10.1149/1945-7111/acb8a6.

[196] J.-M. Kim, S.-M. Chang, J.H. Chang, W.-S. Kim, Agglomeration of nickel/cobalt/manganese hydroxide crystals in couette–taylor crystallizer, Colloids Surf. A Physicochem. Eng. Asp. 384 (2011) 31–39, https://doi.org/10.1016/j.colsurfa.2011.03.016.

[197] J.J. De Yoreo, Principles of crystal nucleation and growth, Rev. Mineral. Geochem. 54 (2003) 57–93, https://doi.org/10.2113/0540057.

[198] K.-J. Wu, E.C.M. Tse, C. Shang, Z. Guo, Nucleation and growth in solution synthesis of nanostructures – from fundamentals to advanced applications, Prog. Mater. Sci. 123 (2022) 100821, https://doi.org/10.1016/j.pmatsci.2021.100821.

[199] D. Gebauer, J.D. Gale, H. Cölfen, Crystal nucleation and growth of inorganic ionic materials from aqueous solution: selected recent developments, and implications, Small 18 (2022), https://doi.org/10.1002/smll.202107735.

[200] H.N. Pollen, J.R. Tolchard, A.M. Svensson, N.P. Wagner, A single-pot co-precipitation synthesis route for Ni-rich layered oxide materials with high cycling stability, Chemelectrochem 9 (2022), https://doi.org/10.1002/celc.202200859.

[201] T. Le Thi, T. Phan Van, B. Nguyen Van, N. To Van, T. Nguyen Van, T.P. Doan, T. L. Ngo, N.H. Vu, T.-T. Nguyen, H.N. Nguyen, N.V. Anh Duy, M.T. Dang, Modified coprecipitation synthesis of nickel-rich NMC ($Li_{1.0}\,Ni_{0.6}\,Mn_{0.2}\,Co_{0.2}\,O_2$) for Lithium-ion batteries: a simple, cost-effective, environmentally friendly method, ACS Omega 8 (2023) 45414–45427, https://doi.org/10.1021/acsomega.3c04717.

[202] Y.-U. Park, J. Kim, H. Gwon, D.-H. Seo, S.-W. Kim, K. Kang, Synthesis of multicomponent olivine by a novel mixed transition metal oxalate coprecipitation method and electrochemical characterization, Chem. Mater. 22 (2010) 2573–2581, https://doi.org/10.1021/cm903616d.

[203] D. Wang, I. Belharouak, G. Zhou, K. Amine, Synthesis of lithium and manganese-rich cathode materials via an oxalate Co-Precipitation method, J. Electrochem. Soc. 160 (2013) A3108–A3112, https://doi.org/10.1149/2.016305jes.

[204] X. Yao, Z. Xu, Z. Yao, W. Cheng, H. Gao, Q. Zhao, J. Li, A. Zhou, Oxalate co-precipitation synthesis of LiNi0.6Co0.2Mn0.2O2 for low-cost and high-energy lithium-ion batteries, Mater. Today Commun. 19 (2019) 262–270, https://doi.org/10.1016/j.mtcomm.2019.02.001.

[205] Z. Zhu, D. Zhang, H. Yan, W. Li, Qilu: precise preparation of high performance spherical hierarchical LiNi0.5Mn1.5O4 for 5 V lithium ion secondary batteries, J Mater Chem A Mater 1 (2013) 5492, https://doi.org/10.1039/c3ta10980a.

[206] A.S. Wijareni, H. Widiyandari, A. Purwanto, A.F. Arif, M.Z. Mubarok, Morphology and particle size of a synthesized NMC 811 cathode precursor with mixed hydroxide precipitate and nickel sulfate as nickel sources and comparison of their electrochemical performances in an NMC 811 lithium-ion battery, Energies 15 (2022) 5794, https://doi.org/10.3390/en15165794.

[207] H. Dong, A. Wang, G. Smart, D. Johnson, G.M. Koenig, In-situ analysis of nucleation and growth of transition metal oxalate battery precursor particles via time evolution of solution composition and particle size distribution, Colloids Surf. A Physicochem. Eng. Asp. 558 (2018) 8–15, https://doi.org/10.1016/j.colsurfa.2018.08.047.

[208] H. Ghadimi Mahanipour, S.M. Masoudpanah, M. Adeli, S.M.H. Hoseini, Regeneration of LiNi0.6Co0.2Mn0.2O2 material from spent lithium-ion batteries by solution combustion synthesis method, J. Energy Storage 79 (2024) 110192, https://doi.org/10.1016/j.est.2023.110192.

[209] N. Ngoepe, A. Gutierrez, P. Barai, J. Chen, P.E. Ngoepe, J.R. Croy, The effects of process parameters on the properties of manganese-rich carbonate precursors: a study of co-precipitation synthesis using semi-batch reactors, Chem. Eng. Sci. 241 (2021) 116694, https://doi.org/10.1016/j.ces.2021.116694.

[210] T.H. Cho, S.M. Park, M. Yoshio, T. Hirai, Y. Hideshima, Effect of synthesis condition on the structural and electrochemical properties of Li[Ni1/3Mn1/3Co1/3]O2 prepared by carbonate co-precipitation method, J. Power Sources 142 (2005) 306–312, https://doi.org/10.1016/j.jpowsour.2004.10.016.

[211] Y.J. Gu, Y. Hu, H.Q. Liu, H.H. Zhou, Z. Guo, Z.W. Hu, Synthesis the precursor of $LiNi_{0.5}Mn_{0.5}O_2$ via an improved carbonate Co-Precipitation, Adv. Mater. Res. 233–235 (2011) 32–35. https://doi.org/10.4028/www.scientific.net/AMR.233-235.32.